Probing the Volcanic–Plutonic Connection and the Genesis of Crystal-rich Rhyolite in a Deeply Dissected Supervolcano in the Nevada Great Basin: Source of the Late Eocene Caetano Tuff

Kathryn E. Watts[1]*, David A. John[1], Joseph P. Colgan[2], Christopher D. Henry[3], Ilya N. Bindeman[4] and Axel K. Schmitt[5]

[1]US Geological Survey, 345 Middlefield Road, Menlo Park, CA 94025, USA; [2]US Geological Survey, Denver Federal Center, Lakewood, CO 80225, USA; [3]Nevada Bureau of Mines and Geology, University of Nevada, Reno, NV 89557, USA; [4]Department of Geological Sciences, University of Oregon, Eugene, OR 97403, USA and [5]Institut für Geowissenschaften, Universität Heidelberg, 69120 Heidelberg, Germany

*Corresponding author. Telephone: (650) 329-5308. E-mail: kwatts@usgs.gov

ABSTRACT

Late Cenozoic faulting and large-magnitude extension in the Great Basin of the western USA has created locally deep windows into the upper crust, permitting direct study of volcanic and plutonic rocks within individual calderas. The Caetano caldera in north–central Nevada, formed during the mid-Tertiary ignimbrite flare-up, offers one of the best exposed and most complete records of caldera magmatism. Integrating whole-rock geochemistry, mineral chemistry, isotope geochemistry and geochronology with field studies and geologic mapping, we define the petrologic evolution of the magmatic system that sourced the $>1100 \, km^3$ Caetano Tuff. The intra-caldera Caetano Tuff is up to ~5 km thick, composed of crystal-rich (30–45 vol. %), high-silica rhyolite, overlain by a smaller volume of comparably crystal-rich, low-silica rhyolite. It defies classification as either a monotonous intermediate or crystal-poor zoned rhyolite, as commonly ascribed to ignimbrite eruptions. Crystallization modeling based on the observed mineralogy and major and trace element geochemistry demonstrates that the compositional zonation can be explained by liquid–cumulate evolution in the Caetano Tuff magma chamber, with the more evolved lower Caetano Tuff consisting of extracted liquids that continued to crystallize and mix in the upper part of the chamber following segregation from a cumulate-rich, and more heterogeneous, source mush. The latter is represented in the caldera stratigraphy by the less evolved upper Caetano Tuff. Whole-rock major, trace and rare earth element geochemistry, modal mineralogy and mineral chemistry, O, Sr, Nd and Pb isotope geochemistry, sanidine Ar–Ar geochronology, and zircon U–Pb geochronology and trace element geochemistry provide robust evidence that the voluminous caldera intrusions (Carico Lake pluton and Redrock Canyon porphyry) are genetically equivalent to the least evolved Caetano Tuff and formed from magma that remained in the lower chamber after ignimbrite eruption and caldera collapse. Thus, the Caetano Tuff contradicts models for the mutually exclusive origins of voluminous volcanic and plutonic magmas in the upper crust. Crystal-scale O isotope data indicate that the Caetano Tuff is one of the most ^{18}O-enriched rhyolites in the Great Basin ($\delta^{18}O_{magma} = 10 \cdot 2 \pm 0 \cdot 2\text{‰}$), supporting anatexis of local metasedimentary basement crust. Metapelite xenoliths in the Carico Lake pluton and ubiquitous xenocrystic zircons in the Caetano Tuff provide constraints for the anatexis process; these data point to shallow ($<15 \, km$) dehydration melting of a protolith similar to the Proterozoic McCoy Creek Group siliciclastic sediments in eastern Nevada, projected beneath Caetano in fault-stacked shelf sediments that were thickened during Mesozoic crustal shortening. Mean zircon U–Pb ages for different stratigraphic levels of the

intra-caldera Caetano Tuff are 34·2–34·5 Ma, 0·2–0·5 Myr older than the caldera sanidine $^{40}Ar/^{39}Ar$ age of 34·00 ± 0·03 Ma, documenting protracted duration of assembly and homogenization of isotopically diverse upper crustal melts, followed by crystallization and zonation to generate the Caetano Tuff magma chamber. Sanidine rims in the least evolved Caetano Tuff and in the Carico Lake pluton and Redrock Canyon porphyry have sharply zoned Ba domains that point to crystal growth during magmatic recharge events. The recharge magma is inferred to have been compositionally similar to the Caetano Tuff magma, with increased Ba resulting from remelting of Ba-rich sanidine cumulates. Mush reactivation to generate the Caetano Tuff eruption was sufficiently rapid to preserve compositional gradients in the intracaldera ignimbrite, calling into question models that predict homogeneity as a prerequisite for remobilizing crystal-rich ignimbrite magmas.

INTRODUCTION

The Earth's largest caldera volcanoes (supervolcanoes) can expel hundreds to thousands of km^3 of silicic magma in a single eruptive event. These eruptions pose extreme geologic hazards and shape the evolution of the Earth's continental crust over geologic time. Ignimbrites are the main erupted products from supervolcanoes, and provide inverted profiles of magma chamber architecture at the time of eruption (Lipman *et al.*, 1966; Hildreth, 1979, 1981; Smith, 1979). Thus, zoning patterns within them are key to identifying the physical, chemical and temporal conditions that culminate in the Earth's most destructive caldera-forming eruptions. Ignimbrite zoning patterns in varied geological settings define a continuum (Hildreth, 1981), but many can be grouped into two categories: (1) crystal-rich, homogeneous ignimbrites of dacitic composition ['monotonous intermediates' of Hildreth (1981)]; (2) crystal-poor ignimbrites of rhyolitic composition that may or may not be chemically zoned with a crystal-rich complement (Bachmann & Bergantz, 2008*a*). Whereas the former are equated to erupted batholiths, unlocked from a rigid state by rejuvenation of the system by more mafic intrusions (Bachmann *et al.*, 2002), the latter are conceived to be the expelled interstitial liquids of a rigid crystal 'sponge' concentrated above a source mush reservoir (Hildreth, 1981; Bachmann & Bergantz, 2004; Hildreth & Wilson, 2007). There are, however, notable exceptions that do not conform to these generalized models, for example: crystal-poor ignimbrites that require more mafic parental source magmas (Streck & Grunder, 2007; Christiansen & McCurry, 2008) combined with varying degrees of assimilation and crystal fractionation (Bryan *et al.*, 2010); crystal-poor ignimbrites derived from partial to wholesale remelting of hydrothermally altered crust (Bindeman & Valley, 2003; Watts *et al.*, 2011; Drew *et al.*, 2013); and crystal-rich 'monotonous' rhyolitic ignimbrites such as those erupted in the Nevada Great Basin (Best *et al.*, 2013*b*, 2013*c*; Henry & John, 2013), the Taupo Volcanic Zone, New Zealand (Matthews *et al.*, 2012; Cooper & Wilson, 2014), and the Southern Rocky Mountain volcanic field (Fridrich *et al.*, 1991; Lipman & Bachmann, 2015).

The link between ignimbrites and plutons is fundamental to understanding the interconnectivity of volcanic and plutonic processes in the upper crust (Bachmann *et al.*, 2007) or lack thereof (Glazner *et al.*, 2004). A model in which remnant crystal-rich mush zones solidify into plutons following eruption of liquid-rich magmas is an attractive framework in which to integrate the two realms (Bachmann & Bergantz, 2004, 2008*b*; de Silva & Gosnold, 2007). However, the counter view is that ignimbrite eruptions record ephemeral conditions of high magma flux into the crust, with rapid development of large magma 'tanks' that are evacuated quickly and completely, leaving little plutonic residue behind (Glazner *et al.*, 2004). The close association between calderas and plutons in areas with extensive exposures of the upper crust (e.g. Southern Rocky Mountain volcanic field, Lipman, 2007) lends support to the volcanic–plutonic connection. On the other hand, geophysical evidence for low-velocity zones beneath large active caldera centers (e.g. Altiplano–Puna Volcanic Complex, Ward *et al.*, 2014; Yellowstone caldera, Farrell *et al.*, 2014; Toba caldera, Stankiewicz *et al.*, 2010) indicates predominantly crystalline and thermally moribund magma reservoirs. The degree to which they are related to the melt-rich chambers that yielded climactic caldera-forming eruptions is debated (Glazner *et al.*, 2004); incremental assembly of near-solid material at lower magmatic flux rates is an alternative possibility (e.g. Frazer *et al.*, 2014). The complexities in answering these questions are compounded by the fact that silicic magma chambers may exist in a sub-solidus or slightly above-solidus (mush) state for much of their lifespans, with only brief 'defrosting' events that lead to melt-rich eruptible conditions (Mahood, 1990; Bachmann & Bergantz, 2004; Hildreth, 2004; Cooper & Kent, 2014). Recharge magmas that pulse the system with heat and partially melt crystalline material (e.g. Wark *et al.*, 2007) are one means by which plutonic or mush bodies are brought to an eruptible state, and modeling has shown that the rejuvenation process can happen rapidly (10–10^4 years) (e.g. Druitt *et al.*, 2012; Huber *et al.*, 2012; Chamberlain *et al.*, 2014). Remobilization may be further aided by buoyancy rheologically 'unzipping' the magma chamber

(Burgisser & Bergantz, 2011; Caricchi *et al.*, 2013; Malfait *et al.*, 2014), external triggering by regional extension (Allan *et al.*, 2012) or local uplift and overpressure of the chamber roof (Gregg *et al.*, 2012, 2015).

The volcanic–plutonic connection has been debated for over half a century (e.g. Buddington, 1959; Lipman, 1984; Petford *et al.*, 2000; Coleman *et al.*, 2004; Glazner *et al.*, 2004; Bachmann *et al.*, 2007). Whereas some recent studies have pointed to a strong genetic connection between ignimbrites and associated plutons in large caldera centers (e.g. Zimmerer & McIntosh, 2013; Bacon *et al.*, 2014; Cole *et al.*, 2014; Lipman & Bachmann, 2015), others have come to the opposite conclusion (e.g. Tappa *et al.*, 2011; Zimmerer & McIntosh, 2012; Mills & Coleman, 2013). The late Eocene Caetano caldera in north–central Nevada offers an exceptional opportunity to track the evolution of a magmatic system that climaxed with a >1100 km³ ignimbrite eruption and continued with a voluminous intrusive phase. Geologic mapping, sanidine $^{40}Ar/^{39}Ar$ geochronology, and whole-rock geochemistry define the caldera stratigraphy, which includes the caldera floor, pre- and post-caldera lavas, a tuff dike, two units of intra-caldera tuff, caldera intrusions, and extra-caldera dikes and domes (John *et al.*, 2008; Colgan *et al.*, 2011; Henry & John, 2013). Integrating whole-rock geochemistry with mineral chemistry, crystal-scale O isotope geochemistry, whole-rock Sr, Nd and Pb isotope geochemistry, and zircon U–Pb geochronology and trace element geochemistry, this study documents the petrologic evolution of the Caetano caldera system. Key questions focus on the genesis of the magma chamber that sourced the Caetano Tuff, the conditions and timescales of magma storage in the crust, the processes that led to its eruption, and the genetic affinity between the caldera-forming tuff and large caldera intrusions. As a crystal-rich, compositionally zoned, rhyolitic ignimbrite, the Caetano Tuff deviates from end-member mush model paradigms (Hildreth, 1981; Bachmann & Bergantz, 2008a; Huber *et al.*, 2012), and may provide an important lens through which to view the volcanic and plutonic underpinnings of calderas worldwide.

GEOLOGICAL BACKGROUND

During the mid-Tertiary the Great Basin was the site of a large ignimbrite 'flare-up', with dozens of caldera centers that developed across SW North America (McKee, 1971; Lipman *et al.*, 1972; Coney, 1978; Best *et al.*, 1989, 2013b; Fig. 1). Magmatism progressed southwestward, consistent with removal, or 'roll-back', of the Farallon slab following flat-slab subduction, causing upwelling of asthenospheric mantle and large-scale crustal melting (Coney & Reynolds, 1977; Humphreys, 1995; Humphreys *et al.*, 2003). Dewatering of the flat-slab may have metasomatized the overriding lithospheric mantle, potentially aiding in partial melting and

concentrating gold and other trace metals that were important for later mineralization in upper crustal rocks, particularly Carlin-type gold deposits in Nevada that cumulatively form the second largest concentration of gold on Earth (Muntean *et al.*, 2011; Fig. 1). Although silicic magmatism continued for about 20 Myr (∼37–19 Ma), the location, distribution, eruptive style, and composition of the eruptive products vary, and have been used to subdivide the broader volcanic province into separate volcanic fields. In Nevada, these include the western Nevada, central Nevada, and Indian Peak–Caliente fields (Best *et al.*, 2013a, 2013b, 2013c; Henry & John, 2013; Fig. 1). Each of these volcanic fields produced exceptionally voluminous ignimbrites (individually hundreds to thousands of km³ and cumulatively tens of thousands of km³; Best *et al.*, 2013b). Some ignimbrites traveled >250 km from their source calderas, channelized along paleovalleys that drained the western margin of the Nevadaplano highland during the mid-Tertiary (Best *et al.*, 2009; Henry *et al.*, 2012; Cassel *et al.*, 2014; Fig. 1). This topographic boundary roughly coincides with a crustal transition from Precambrian basement in eastern Nevada to rifted allochthonous and oceanic terranes across central and western Nevada. Thus Nevada's volcanic fields developed across a highly diverse crustal profile (Best *et al.*, 2013a, 2013c; Henry & John, 2013; Fig. 1).

The Caetano caldera is one of the oldest calderas in the western Nevada volcanic field, formed during eruption of the 34·0 Ma Caetano Tuff in north–central Nevada (John *et al.*, 2008; Henry & John, 2013; Fig. 2). Large-magnitude (∼110%) east–west extension during the middle Miocene cut and tilted the caldera into a series of east-dipping fault blocks that expose the caldera interior in three dimensions over a 5 km paleodepth range (Colgan *et al.*, 2008, 2011). Removing post-collapse extension yields original caldera dimensions of 20 km east–west by 12–18 km north–south (John *et al.*, 2008). A compound cooling unit of densely welded intra-caldera ignimbrite up to ∼3·6 km thick was the first erupted and volumetrically dominant part of the Caetano Tuff eruption and is defined as the lower unit (John *et al.*, 2008; Fig. 2). Thin ash beds suggest minor discontinuities in an otherwise continuous eruption, and megabreccia and mesobreccia lenses occur mostly within 1–2 km of the caldera margin, composed of Paleozoic and lesser Tertiary wall-rocks shed from the caldera margin (John *et al.*, 2008; Fig. 2). Thin welded ignimbrite deposits (∼9) and interbedded sediments define an upper intra-caldera tuff unit 0·5–2 km thick (Fig. 2) that records a transition to sporadic, low-magnitude eruptions during the waning stages of caldera magmatism (John *et al.*, 2008). A complete depositional and cooling break separates the lower and upper tuff units (Fig. 2). The caldera floor is exposed in a small region of the northwestern part of the caldera (<0·5 km) and more extensively in the northeastern (∼2 km) and southeastern (∼4 km) parts of the caldera, where basal tuff vitrophyres overlie Eocene pre-caldera andesite
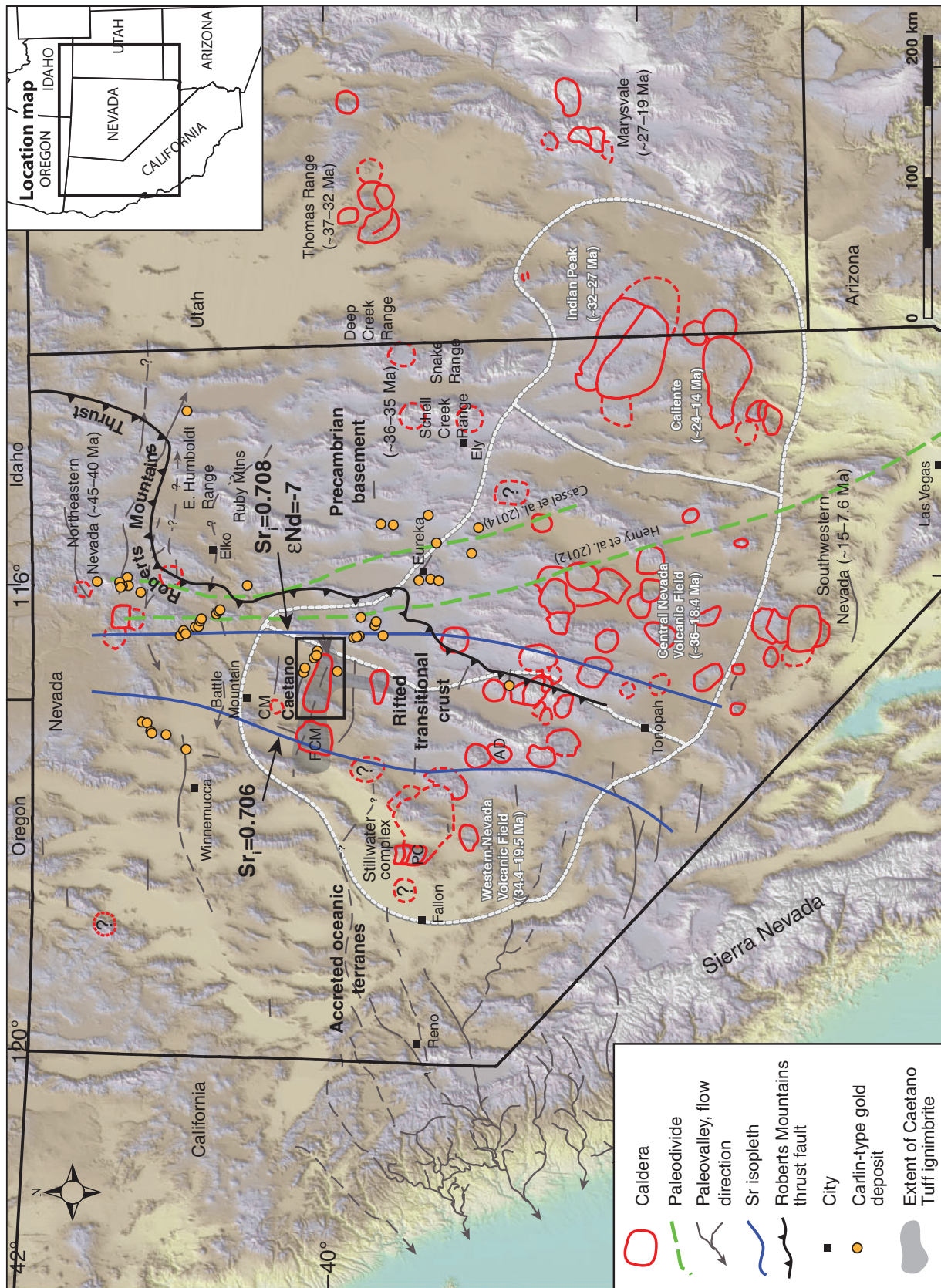
Fig. 1. Regional map showing locations of calderas and major crustal features in the Nevada Great Basin. White dashed lines show the approximate boundaries between defined volcanic fields. The Caetano caldera area is outlined by the bold black box (area of Fig. 2), and the inferred extent of the Caetano Tuff ignimbrite is shown by gray shading. The distribution of Carlin-type gold deposits is from Muntean *et al.* (2011). The Sr$_i$ 0.706, Sr$_i$ 0.708 and ɛNd −7 boundaries are from Farmer & DePaolo (1983). Abbreviations for calderas mentioned in the text: FCM, Fish Creek Mountains; CM, Cove Mine; PC, Poco Canyon; AD, Arc Dome. Map modified after Henry & John (2013).
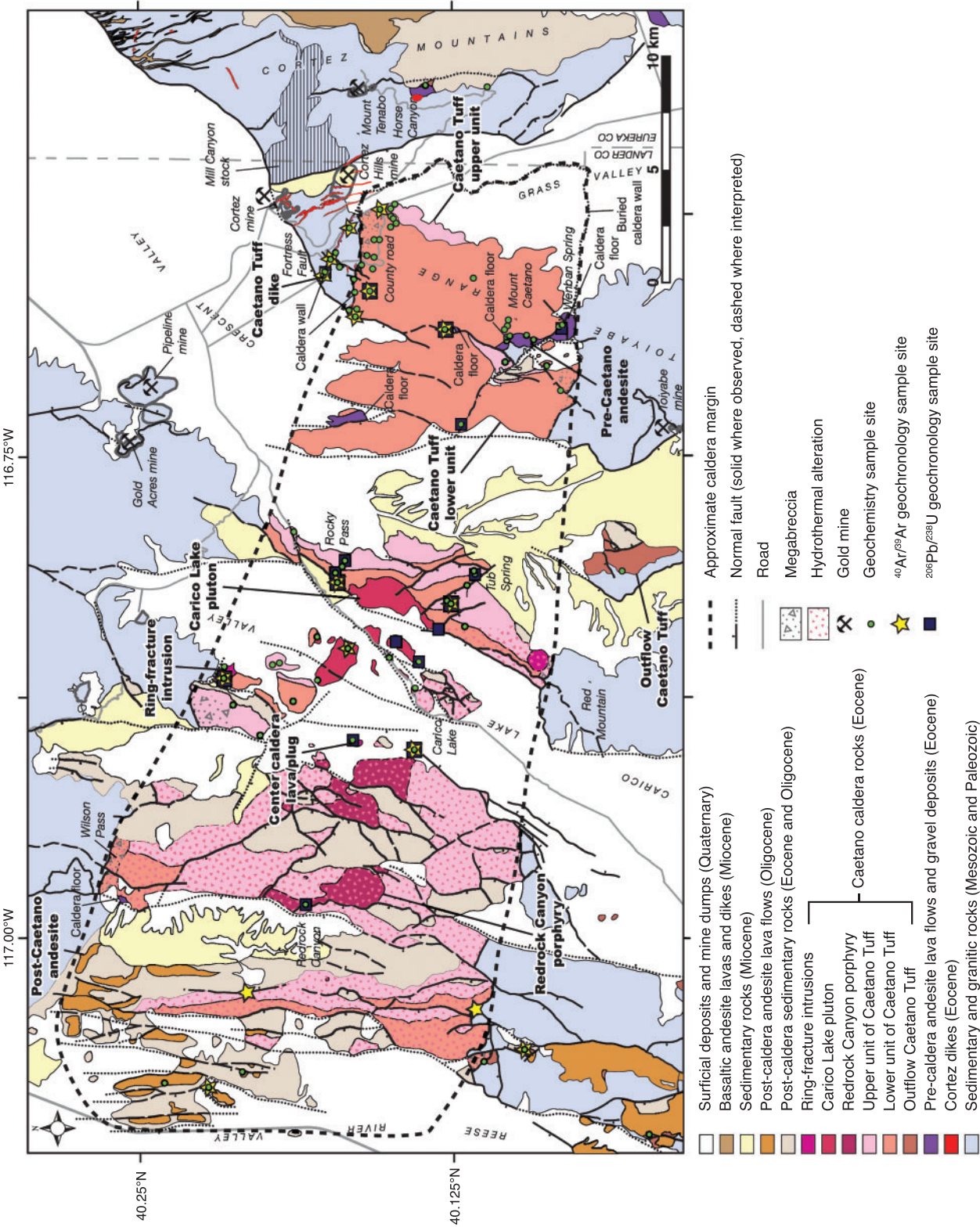
Fig. 2. Geologic map of the Caetano caldera, showing geologic units, caldera features, and sampling localities. The elongate shape of the caldera margin is due to ~110% east-west extension in the middle Miocene that dissected the caldera basin into a series of east-dipping fault blocks (Colgan *et al.,* 2008). Map modified after Colgan *et al.* (2011) and Henry & John (2013).

lavas, breccias, and pre-volcanic conglomerate deposited on Paleozoic basement (Fig. 2). A restored (pre-extension) caldera area of 280 km^2 and an average 3 km tuff thickness yields a volume of 840 km^3 for the intra-caldera Caetano Tuff. Outflow Caetano Tuff is preserved 50 km to the west and south, but only 5 km east of the caldera (Figs 1 and 2). Caldera collapse generated a basin that was further filled with >1 km of sediments and unrelated tuffs. The distribution of outflow tuff and excess depth of the caldera basin (∼1 km) are consistent with an additional volume of 280 km^3. Combined, this yields a conservative volume estimate of >1100 km^3 for the Caetano Tuff (John *et al.*, 2008), making it one of the most voluminous ignimbrite eruptions in the Nevada Great Basin (Best *et al.*, 2013*b*; Henry & John, 2013).

Precursory magmatism to the Caetano Tuff eruption included pre-caldera andesite lavas and block and ash flows that locally form the caldera floor, and extra-caldera silicic dikes and domes that were intruded near the northeastern caldera margin (Fig. 2). The latter include variably hydrothermally altered, 35·7–36·3 Ma rhyolite dikes in the Cortez and Cortez Hills regions that are associated with several large Carlin-type gold deposits (Fig. 2). Although the dikes and gold mineralization predated the Caetano Tuff eruption by 1·5–2 Myr, an early manifestation of caldera magmatism may have provided an important source of heat, fluids and potentially metals in these economically valuable deposits (Muntean *et al.*, 2011). A 10–40 m thick composite tuff dike, composed of crystal-rich (25–35 vol. %) and aphyric to nearly aphyric (<5 vol. %) high-silica rhyolite is exposed along a ring-fracture on the northeastern caldera margin (Fig. 2; Henry & John, 2013). It is interpreted to be an early vent source of the Caetano Tuff eruption, which climaxed with eruption of >1100 km^3 of crystal-rich (30–45 vol. %) rhyolite tuff, normally zoned from high- to low-silica compositions. Crystal-rich (25–45 vol. %) pumices occur in both lower and upper tuff units and are particularly abundant in basal Caetano Tuff vitrophyres at Wenban Spring near the southeastern caldera margin and in a county road cut along the northeastern caldera wall (Fig. 2). Sparse aphyric to nearly aphyric (<5 vol. %) pumices are present locally in the basal Caetano Tuff. Pumice concentrations decrease upwards in the lower Caetano Tuff unit and fiamme are rare in the upper sections. Fresh pumices are present in vitrophyres of the upper Caetano Tuff unit, notably at Tub Spring east of Carico Lake Valley (Fig. 2), and mildly altered (orange) crystal-rich pumices are present in many devitrified exposures.

Several intrusions of low-silica rhyolite were emplaced shortly after the Caetano Tuff eruption. The largest of these are the Carico Lake pluton and Redrock Canyon porphyry, exposed over a pre-extension area of ∼ 15 km^2 in the center of the caldera (Fig. 2). Basal zones of the pluton and porphyry are not exposed, but reconstructions of caldera fault blocks indicate that they extend to >3·5 km depth relative to the top of the intra-caldera tuff sequence (Colgan *et al.*, 2011), yielding a

minimum combined volume of >50 km^3. Aeromagnetic data for the Caetano caldera (Fig. 3) indicate that the total pluton volume at depth is probably much greater. Magnetic highs distinctly outline the Carico Lake pluton, and overlie the altered Redrock Canyon porphyry and altered and unaltered intra-caldera Caetano Tuff. Given that altered rocks have no magnetic susceptibility, and that the Caetano Tuff is reversely magnetized (MacDonald *et al.*, 2012), the magnetic highs in the caldera cannot arise from either the altered rocks, unaltered tuff at depth, or reversely magnetized tuff at the surface. Thus, the aeromagnetic data support the presence of caldera-wide intrusions with magnetization induced by the Earth's present-day normal polarity magnetic field, as commonly observed in coarse-grained igneous intrusions (e.g. Bacon *et al.*, 2014). If not related to caldera intrusions, the magnetic high beneath Mount Caetano in the southeastern caldera (Fig. 3) may be related to plutonic remnants from the pre-Caetano andesite eruption (Fig. 2), and/or Mesozoic plutons. The magnetic high extending from Mount Tenabo along the eastern caldera boundary coincides with mapped exposures of the Jurassic Mill Canyon stock (Figs 2 and 3), which would be consistent with the latter interpretation. In addition to the voluminous caldera intrusions, a small ring-fracture intrusion of low-silica rhyolite is present along the northern caldera margin (Fig. 2), a pervasively altered ring-fracture intrusion is present along the southern caldera margin (Fig. 2), and a small, locally brecciated, lava or plug of high-silica rhyolite is exposed <1 km east of the Redrock Canyon porphyry (Fig. 2).

Heat from intrusion of the Redrock Canyon porphyry and/or deeper residual Caetano magma drove a large hydrothermal system that altered the western half of the caldera over an area of more than 110 km^2 (Fig. 2). This hydrothermal system had ceased by the time of intrusion of the unaltered Carico Lake pluton (John *et al.*, 2011), which may have cut off its heat source. The presence of metapelite xenoliths in the Carico Lake pluton and their absence in the Redrock Canyon porphyry are consistent with a deeper magmatic source for the pluton. Both intrusions ultimately rose to within <1 km of the paleosurface, cross-cutting the intra-caldera fill sequence; the Carico Lake pluton locally domed and steeply tilted intra-caldera Caetano Tuff in the center of the caldera (John *et al.*, 2008; Colgan *et al.*, 2011). In addition to unusually steep dips (70–90°) and anomalous westerly strikes of Caetano Tuff rocks surrounding the Carico Lake pluton, its shallow emplacement is supported by concentric magnetic highs that form a distinct 'bulls-eye' pattern around mapped Carico Lake pluton exposures (Fig. 3). High-precision single crystal sanidine ^{40}Ar/^{39}Ar dating of the intra-caldera tuff and intrusions indicates that eruption, caldera formation, resurgence, hydrothermal alteration, and final pluton consolidation occurred within a span of <100 kyr (John *et al.*, 2008; Henry & John, 2013). Post-caldera andesites in the northwestern part of the caldera (Fig. 2) are the
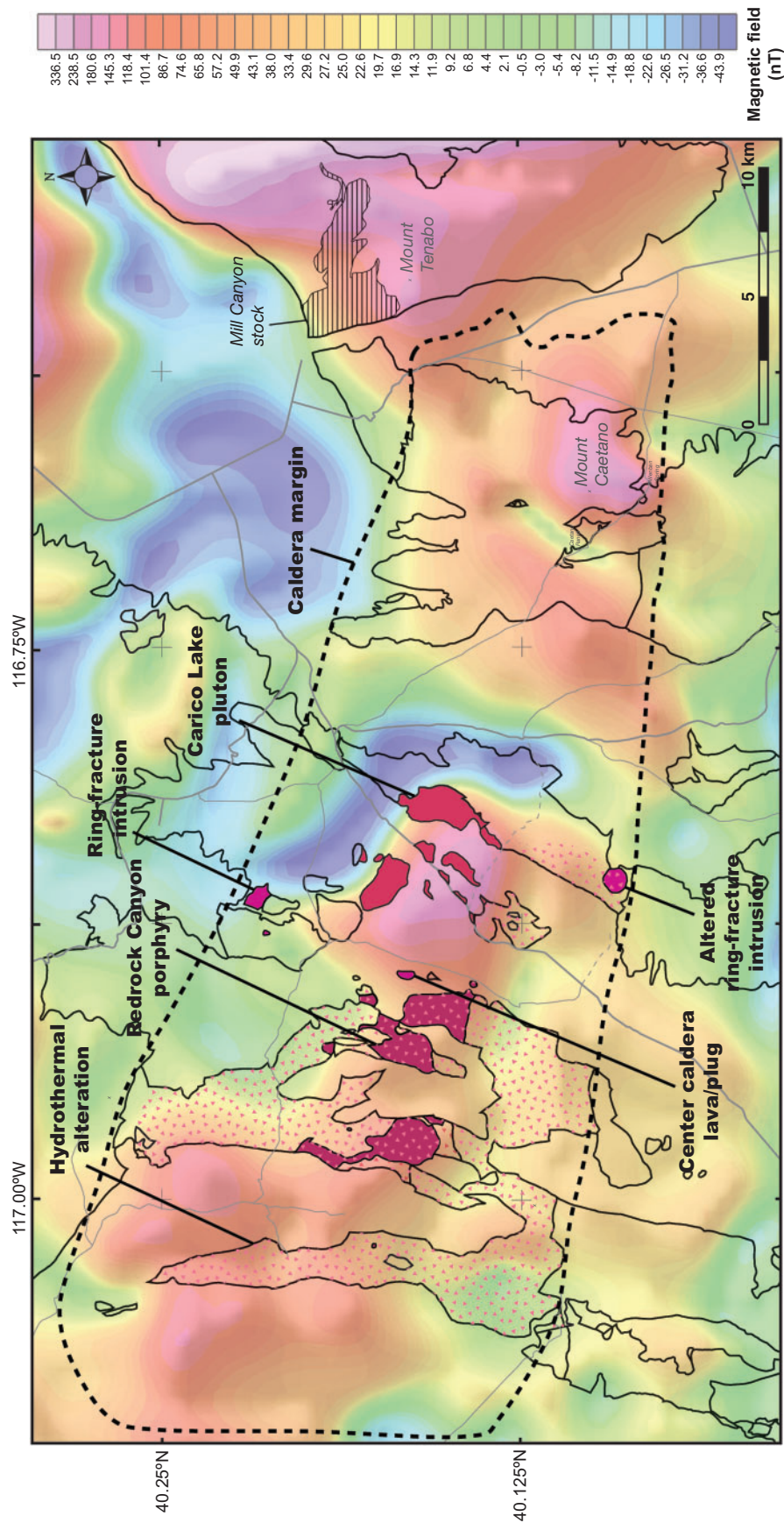
Fig. 3. Aeromagnetic map of the Caetano caldera, overlain by geologic map boundaries (Fig. 2), with intrusive caldera units shown by filled pink areas and hydrothermal alteration shown by the stippled pattern. Aeromagnetic data from Kucks *et al.* (2006).

last known phase of magmatic activity and postdate the caldera-forming eruption by about 500 kyr.

METHODS

Whole-rock major and trace element compositions were determined using X-ray fluorescence (XRF) and inductively coupled plasma-mass spectrometry (ICP-MS) for a comprehensive suite of extrusive and intrusive Caetano units. Samples were crushed and hand-picked to obtain lithic-free chips for analysis. New XRF data are combined with previously published data (John *et al.*, 2008; Henry & John, 2013), totaling 115 analyses. An additional 23 analyses were discarded on the basis of alteration, apparent by their high SiO_2, high K_2O and/or low Na_2O contents. All XRF and ICP-MS data were collected at the Washington State University GeoAnalytical Laboratory or US Geological Survey (USGS) contracted SGS Minerals laboratory in Toronto.

Mineral chemistry was determined for a representative subset of Caetano samples. Major element compositions of plagioclase, sanidine, orthopyroxene, clinopyroxene, biotite and hornblende, and Ba zoning profiles in sanidine, were measured with a JEOL 8900 electron microprobe at the USGS Menlo Park microanalytical facility. For single-spot mineral analyses, the electron microprobe was operated at a 15 kV accelerating voltage and beam conditions were tuned as follows: a 5 nA focused (<1 μm diameter) beam for plagioclase and sanidine, a 15 nA focused beam for pyroxene, and a 5 nA defocused (5 μm diameter) beam for biotite and hornblende. For sanidine Ba zoning profiles, the electron microprobe was operated at a 15 kV accelerating voltage, with a 20 nA focused beam, and linear traverses were measured in 4 μm step increments. Cathodoluminescence (CL) imaging using a JEOL 5600 LV scanning electron microscope (SEM) allowed targeting of discrete compositional boundaries within single sanidine crystals. A variety of USGS mineral, glass and major oxide standards were analyzed throughout each analytical session to monitor instrument drift and correct compositional offsets.

Oxygen isotope analyses were performed at the University of Oregon stable isotope laboratory using CO_2-laser fluorination (Bindeman, 2008). Single- or multi-crystal mineral separates and whole-rock powders were reacted under vacuum with a CO_2 laser and BrF_5 reagent to liberate oxygen gas from 1·5–2·5 mg aliquots. For reactive sanidine and whole-rock powder analyses, an airlock chamber was used to isolate single samples for analysis. The O_2 gas generated in the laser chamber was purified through a series of cryogenic traps and a mercury diffusion pump was used to remove traces of fluorine gas. Oxygen was converted to CO_2 gas in a small platinum–graphite converter, the yield was measured, and then CO_2 gas was analyzed on a ThermoFinnigan MAT 253 mass spectrometer. All $\delta^{18}O$ values were calculated relative to Vienna Standard Mean Ocean Water (VSMOW). A University of Oregon

garnet standard ($\delta^{18}O = 6\cdot52‰$, VSMOW) was analyzed with the unknowns during each analytical session. Variability of the measured $\delta^{18}O$ values of the garnet standard ranged from –0·1 to +0·2‰ from its empirical value, which was used to correct $\delta^{18}O$ offsets in unknowns. The average reproducibility of the garnet standard was 0·1–0·2‰ in conventional and airlock measurements. Single crystal core and rim zircon analyses were obtained with a CAMECA ims 1270 ion microprobe at UCLA, targeting the same zircon spots (after repolishing) as previously dated by U–Pb for 10 Caetano samples. Instrumental calibrations were made using the R33 zircon standard ($\delta^{18}O = 5\cdot55‰$, VSMOW), which had an average reproducibility of 0·2–0·3‰. A few higher in $\delta^{18}O$ (elevated by ∼1‰, possibly xenocrystic) R33 grains were omitted. TEMORA 2 zircon ($\delta^{18}O = 8\cdot20‰$, VSMOW) was used as a secondary standard during ion microprobe O isotope sessions, and had an average reproducibility of 0·2‰.

Strontium, neodymium and lead isotope analyses of whole-rock powders were combined with oxygen isotope data for a subset of Caetano samples. These measurements were made on a ThermoFinnigan TRITON thermal ionization multicollector mass spectrometer at Carleton University in Ottawa, Canada. Isotopic ratios were corrected for radiogenic ingrowth using a caldera $^{40}Ar/^{39}Ar$ age of 34·0 Ma.

Zircon U–Pb age and trace element analyses were obtained on the sensitive high-resolution ion microprobe-reverse geometry (SHRIMP-RG) co-operated by the USGS and Stanford University. This effort was made over 5 years, with a database totaling over 300 analyzed zircon spots for Caetano caldera units. Zircons were separated from whole-rock powders using standard heavy liquid and magnetic separation techniques, hand-picked under a binocular microscope, mounted in epoxy, and ground down to expose grain interiors. Zircons were imaged with CL on a JEOL 5600 SEM to identify internal structures and zonation and target analytical spots. Secondary ions were generated from the target spot with an O_2^- primary ion beam varying in intensity from 4·0 to 5·5 nA, with a typical ion beam spot diameter of 20–25 μm. Secondary ion intensities were measured in 4–5 cycles in mass order (peak-hopping from mass 89 to 270), and included Y, Hf, and nine rare earth elements (REE). For six samples, Ti concentrations were also measured in a separate analytical session. U–Pb ages were calculated relative to the R33 zircon standard (419·3 Ma; Black *et al.*, 2004). Data reduction for geochronology follows the methods described by Williams (1997) and Ireland & Williams (2003), and uses the Excel add-in programs Isoplot 3.76 and Squid 2.51 of Ludwig (2009, 2012). U, Th, and trace element concentrations (Y, Hf, Ti, REE) were standardized against MAD-green zircon (Barth & Wooden, 2010). Ti concentrations and the Ti-in-zircon thermometer of Ferry & Watson (2007) were used to estimate crystallization temperatures for Caetano zircons, using an average Ti activity ($aTiO_2$) of 0·4 for Caetano

rhyolites, which was constrained from the compositions of equilibrium Fe–Ti oxide pairs in the Caetano Tuff (Ghiorso & Evans, 2008). Zircon saturation temperatures and whole-rock liquidus temperatures for the same Caetano samples or units were calculated using the calibration of Boehnke *et al.* (2013) and the Rhyolite-MELTS thermodynamic modeling software of Gualda *et al.* (2012).

WHOLE-ROCK GEOCHEMISTRY

Major elements
The Caetano Tuff and all intrusive Caetano units are calc-alkaline rhyolites (SiO_2 = 71–78 wt %) and distinctly peraluminous [alumina saturation index (ASI) = 1·0–1·2] (Fig. 4; Table 1; Supplementary Data Table 1; supplementary data are available for downloading at http://www.petrology.oxfordjournals.org). The most evolved compositions are found in the Caetano Tuff dike and the lower unit of the Caetano Tuff, whereas the least evolved compositions occur in the upper unit of the Caetano Tuff, the Carico Lake and Redrock Canyon intrusions, and the small ring-fracture intrusion (Fig. 4a; Table 1). Outflow tuff spans the geochemical range of intracaldera Caetano Tuff units (Fig. 4a). Pumices from the lower unit of the Caetano Tuff have overlapping to slightly less evolved compositions, with the exception of one pumice clast with a dacitic composition (Fig. 4a). Pre- and post-caldera andesite flows are the most primitive eruptive products (Fig. 4a). Metapelite xenoliths in the Carico Lake pluton are mafic (SiO_2 = 45–55 wt %) and extremely peraluminous (ASI up to 2·9) (Fig. 4). Their composition is consistent with that of a refractory restite from partial melting of pelitic crust (e.g. Patiño Douce, 1999); the least evolved Caetano rhyolites have compositions that fall within the partial melt fields for mafic metapelite and metagraywacke sources (Fig. 5; Patiño Douce & Johnston, 1991; Lee *et al.*, 2003).

The intra-caldera Caetano Tuff is compositionally zoned and can be subdivided into two compositional groups: a high-SiO_2 (75–78 wt %) and low-TiO_2 (0·05–0·15 wt %) group that forms the bulk of the lower Caetano Tuff and a more variable low-SiO_2 (71–75 wt %) and high-TiO_2 (0·15–0·30 wt %) group that forms the upper part of the lower Caetano Tuff and the entire upper Caetano Tuff (Fig. 6a and b). To document vertical zonation, samples were projected to their stratigraphic positions relative to the caldera floor (0 m) or the cooling break between the upper and lower tuff units (~3600 m in the most complete sections in the eastern caldera). Most geochemical analyses are from the less altered eastern part of the caldera (Fig. 2), and average uncertainties in projected depths are ± 50–100 m. Geochemical data for the Carico Lake pluton and Redrock Canyon porphyry demonstrate a compositional affinity to the least evolved (upper) parts of the intra-caldera Caetano Tuff sequence (Fig. 6a and b). Liquidus temperatures calculated using Rhyolite-
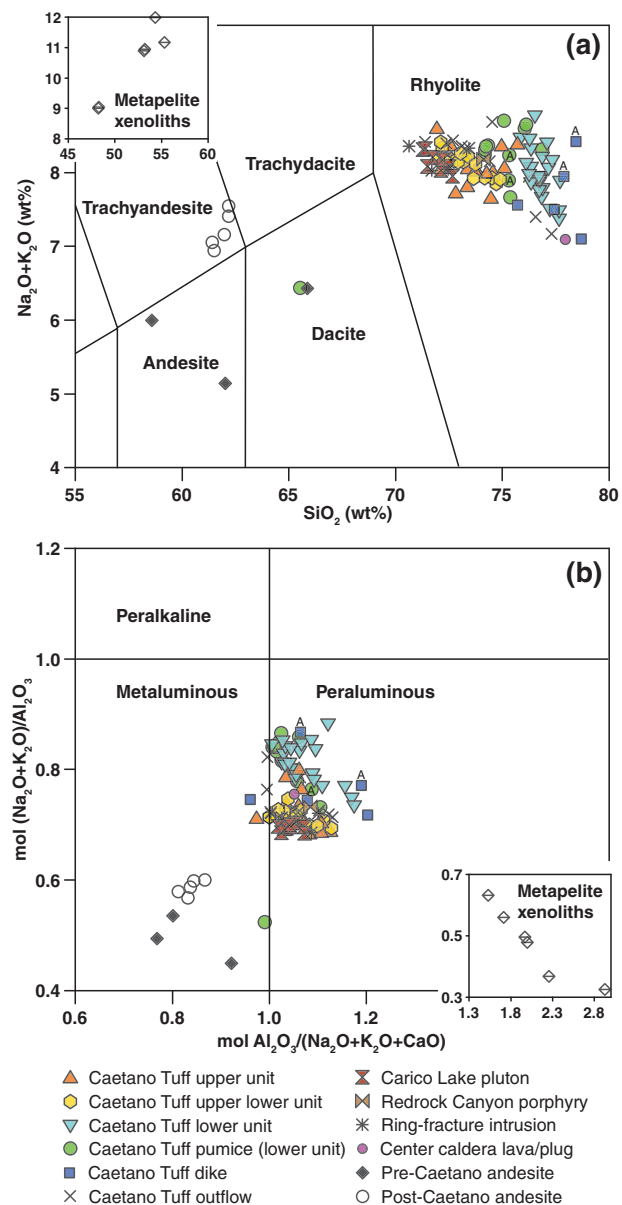

Fig. 4. Whole-rock geochemical classification diagrams. (a) Total alkali–silica diagram. (b) Alumina saturation indices. 'A' denotes aphyric samples.

MELTS for Caetano whole-rock compositions (1·5 kbar, 4 wt % H_2O, ΔQFM = 0, where QFM is quartz–fayalite–magnetite buffer) correspond to a temperature range of ~800–860°C, and exhibit a zoning pattern consistent with higher temperatures and increasingly less evolved compositions up-sequence (Fig. 6c; Table 1; Supplementary Data Table 1).

Despite the pronounced compositional and thermal variation in the intra-caldera Caetano Tuff (Fig. 6a–c), it is highly crystal-rich (30–45 vol. %) throughout (Fig. 6d; Table 2; Supplementary Data Table 2). Crystal-poor components of the eruption were restricted to volumetrically minor (<10 m thick) aphyric parts of the tuff dike and sparse aphyric pumices within the lower Caetano

Table 1: Whole-rock major and trace element compositions of representative Caetano caldera samples

Sample:	08-DJ-85	08-DJ-87	06-DJ-6	05-DJ-21	08-DJ-72	06-DJ-64	08-DJ-43
Unit:	Caetano Tuff upper unit	Caetano Tuff upper unit	Caetano Tuff upper unit	Caetano Tuff upper lower unit	Caetano Tuff upper lower unit	Caetano Tuff upper lower unit	Caetano Tuff lower unit
Latitude (°N):	40·1279	40·1264	40·1994	40·1713	40·1503	40·1890	40·1577
Longitude (°W):	−116·8248	−116·8269	−116·7866	−116·8102	−116·6305	−116·8771	−116·6529
Strat. pos. (m):	3840	3686	3460	3380	3210	2750	1760
Major element analyses by XRF (wt %), normalized to 100% anhydrous							
SiO_2	72·10	72·78	72·58	72·15	73·37	72·28	75·81
TiO_2	0·27	0·23	0·25	0·30	0·23	0·25	0·12
Al_2O_3	15·10	14·74	14·79	15·41	15·14	14·76	13·07
FeO*	1·79	1·92	1·53	1·33	0·88	1·95	1·19
MnO	0·03	0·04	0·02	0·02	0·01	0·04	0·05
MgO	0·27	0·55	0·48	0·25	0·21	0·42	0·17
CaO	2·31	1·94	2·07	2·11	1·87	2·06	1·07
Na_2O	3·04	3·06	3·02	3·34	3·03	3·40	3·35
K_2O	5·01	4·66	5·17	4·99	5·19	4·76	5·11
P_2O_5	0·08	0·06	0·08	0·10	0·07	0·08	0·04
LOI	2·43	2·73	—	—	0·97	—	2·53
Un-normalized sums	99·80	98·57	97·61	97·33	100·15	95·30	101·33
Liquidus *T* (°C)	856	893	866	864	845	871	802
Trace element analyses by XRF (ppm)							
V	13	15	10	19	10	18	8
Cr	—	—	2	4	—	3	—
Co	2·4	2	1·4	1·7	1·5	2·3	1
Ni	9	6	3	6	19	2	10
Cu	—	—	3	4	—	5	—
Zn	48	48	40	47	32	53	44
Ga	24	22	19	20	22	18	17
Rb	146	184	158	132	128	151	216
Sr	422	388	282	404	354	378	111
Ba	1530	1380	1053	1636	1630	1430	305
Y	19	16	17	17	14	18	23
Zr	173	180	158	221	176	198	97
Nb	13	12	12	12	11	12	18
Pb	25	24	24	21	23	20	29
Th	24	24	21	19	23	20	23
U	6·2	5·9	—	—	4·8	2	9
Trace element analyses by ICP-MS (ppm)							
La	58	55	133	85	66	75	22
Ce	102	99	214	136	111	126	46
Pr	11	11	23	15	12	14	6
Nd	38	36	70	48	42	45	21
Sm	6·7	5·6	8·7	6·6	6·3	6·6	4·9
Eu	1·05	0·95	1·29	1·45	1·15	1·21	0·46
Gd	5·1	4·6	5·2	4·6	5·0	4·5	4·6
Tb	0·68	0·64	0·64	0·55	0·63	0·63	0·80
Dy	3·3	3·0	3·0	3·08	2·7	3·3	4·4
Ho	0·63	0·55	0·56	0·56	0·50	0·62	0·90
Er	1·92	1·68	1·43	1·59	1·40	1·82	2·55
Tm	0·30	0·24	0·22	0·25	0·20	0·29	0·38
Yb	1·90	1·80	1·40	1·50	1·60	1·80	2·50
Lu	0·29	0·25	0·22	0·24	0·24	0·28	0·40

(Continued)

Tuff unit. Winnowing of ash from crystals during explosive eruption appears not to have significantly increased the phenocryst content of the Caetano Tuff, based on uniformly high crystallinities in all erupted parts of the ignimbrite and the presence of comparably crystal-rich pumices (25–45 vol. %) in lower and upper tuff units. Thus, the Caetano Tuff differs from crystal-rich, dacitic ignimbrites (i.e. 'monotonous intermediates', Hildreth, 1981), and ignimbrites that are zoned in composition and crystallinity, typically with a large crystal-poor component (see Bachmann & Bergantz, 2008a; Huber et al., 2012). Many similar crystal-rich rhyolites exist in the western Nevada volcanic field, both in close proximity to the Caetano caldera (tuff of Cove Mine and Fish Creek Mountains Tuff <5–10 km to the NW and west) and at greater distance (tuff of Poco Canyon in the Stillwater caldera complex and tuff of Arc Dome > 100 km to the SW) (Figs 1 and 7). Crystal-rich (>30 vol. %) to moderately crystal-rich (20–30 vol. %)

rhyolites that do not conform to a two-state ignimbrite classification scheme also occur in the central Nevada volcanic field (Best et al., 2013c), the Southern Rocky Mountain volcanic field (Fridrich et al., 1991; Mills & Coleman, 2013; Lipman & Bachmann, 2015), and the Taupo Volcanic Zone (Matthews et al., 2012; Cooper & Wilson, 2014) (Fig. 7).

Rhyolite-MELTS crystallization modeling for Caetano whole-rock compositions demonstrates that the compositional range of the Caetano Tuff can be produced by progressive crystallization of the least evolved rhyolite (Carico Lake pluton; 72 wt % SiO_2) (Fig. 8a), or alternatively, a more evolved rhyolite that falls between the two compositional groups (hypothetical 'gap' rhyolite; 74·5 wt % SiO_2) (Fig. 8b). Coeval evolution of the liquid and principal solid phases (plagioclase, sanidine, quartz) results in a compositional gap of ∼3 wt % SiO_2, yielding a high-silica (∼75–77 wt % SiO_2) rhyolite liquid and a low-silica (∼72–73 wt % SiO_2) solid cumulate

Table 1: Continued

Sample:	06-DJ-23	05-DJ-5	H08-113B	06-DJ-1	09-DJ-7	06-DJ-34†	11-DJ-17	10-DJ-32	11-DJ-3	H05-52	09-DJ-77
Unit:	Caetano Tuff lower unit	Caetano Tuff lower unit	Caetano Tuff lower unit dike	Caetano Tuff outflow	Caetano Tuff outflow	Carico Lake pluton	Redrock Canyon porphyry	Ring-fracture intrusion	Center caldera lava/plug	Pre-Caetano andesite	Post-Caetano andesite
Latitude (°N):	40·1171	40·0954	40·1768	39·8759	40·1137	40·1507	40·1838	40·2161	40·1649	40·1267	40·2229
Longitude (°W):	−116·6572	−116·6868	−116·6567	−116·8112	−117·0639	−116·854	−116·9822	−116·8591	−116·8979	−116·6845	−117·078
Strat. pos. (m):	1450	5	—	—	—	—	—	—	—	—	—
Major element analyses by XRF (wt %), normalized to 100% anhydrous											
SiO_2	76·69	76·30	78·66	74·51	76·52	71·38	74·08	70·61	77·92	62·01	61·41
TiO_2	0·11	0·09	0·12	0·15	0·10	0·34	0·20	0·30	0·16	0·92	0·82
Al_2O_3	12·82	13·06	12·14	13·43	12·94	15·80	14·25	15·43	12·11	16·88	16·05
FeO*	1·09	1·12	0·42	1·58	1·30	1·42	1·45	2·29	1·10	5·67	5·31
MnO	0·06	0·06	0·03	0·02	0·05	0·01	0·01	0·05	—	0·14	0·10
MgO	0·37	0·24	0·26	0·25	0·37	0·23	0·28	0·54	0·27	3·07	3·17
CaO	1·07	1·02	1·22	1·33	1·28	2·36	1·49	2·32	1·30	5·88	5·73
Na_2O	3·33	3·70	2·41	2·92	2·49	3·47	2·81	3·74	2·62	3·61	2·99
K_2O	4·42	4·37	4·69	5·76	4·91	4·85	5·37	4·62	4·48	1·53	4·06
P_2O_5	0·05	0·04	0·05	0·04	0·03	0·13	0·06	0·10	0·04	0·28	0·35
LOI	—	—	2·50	—	2·49	2·44	2·20	2·53	2·07	2·33	2·00
Un-normalized sum	96·93	97·08	96·81	98·53	99·65	96·58	101·30	99·36	97·41	100·68	96·56
Liquidus *T* (°C)	841	813	—	857	—	875	830	893	—	—	—
Trace element analyses by XRF (ppm)											
V	14	10	19	7	7	18	—	15	8	145	140
Cr	—	3	7·5	4	—	3	<10	—	<10	80	60
Co	1·9	0·9	—	1·3	1	—	1·2	2·9	1	13	12
Ni	10	6	3·9	5	7	6	<5	—	7	47	31
Cu	—	3	1	1	—	3	<5	5	6	9	11
Zn	63	49	99	34	42	47	32	46	8	82	91
Ga	18	19	17	16	17	18	18	19	16	20	17
Rb	315	225	302	152	211	123	157	129	135	129	125
Sr	96	84	86	219	124	447	246	379	210	677	707
Ba	346	177	588	846	553	1645	1130	1260	1520	1030	2030
Y	37	25	32	13	19	13	15	15	17	20	18
Zr	101	85	93	138	101	269	180	199	133	183	197
Nb	26	19	28	10	14	11	12	11	6	12	12
Pb	36	31	23	23	27	20	18	22	22	14	17
Th	25	22	22	19	22	19	18	19	17	11	16
U	10·6	—	8·7	1	7·2	4	3·4	4·8	4·8	2·5	4·4
Trace element analyses by ICP-MS (ppm)											
La	27	19	26	43	29	66	52	55	41	39	38
Ce	55	41	50	75	57	115	89	97	78	70	70
Pr	7	5	6	9	7	12	10	10	8	9	8
Nd	25	19	22	29	24	42	35	35	28	34	34
Sm	6	4·6	5·8	4·7	4·8	6·3	5·3	5·4	4·5	5·9	5·7
Eu	0·42	0·28	0·43	0·84	0·44	1·49	0·94	1·07	0·86	1·39	1·39
Gd	6·6	4·6	5·7	3·6	3·8	4·5	3·7	3·8	3·6	4·7	5·2
Tb	1·25	0·71	0·96	0·48	0·59	0·60	0·51	0·52	0·55	0·66	0·60
Dy	6·6	4·3	5·7	2·5	3·3	2·5	2·7	2·8	2·8	3·8	3·5
Ho	1·36	0·86	1·10	0·45	0·69	0·47	0·49	0·57	0·57	0·72	0·67
Er	4·38	2·56	2·95	1·39	1·93	1·50	1·49	1·66	1·58	2·06	2·07
Tm	0·59	0·39	0·45	0·23	0·30	0·18	0·20	0·25	0·23	0·29	0·29
Yb	4·00	2·50	2·96	1·40	2·00	1·40	1·50	1·60	1·60	2·00	1·90
Lu	0·62	0·40	0·46	0·22	0·32	0·28	0·23	0·31	0·28	0·36	0·32

Strat. pos., stratigraphic position calculated relative to the exposed caldera floor (0 m) in the eastern part of the caldera and extrapolated from the cooling break (3600 m) for samples west of the Toiyabe Range. Liquidus temperatures were calculated using major element compositions and the Rhyolite-MELTS thermodynamic modeling software of Gualda *et al.* (2012) at 1·5 kbar and 4 wt % H_2O. —, no data. LOI, loss on ignition. See Supplementary Data Table 1 for compilation of major and trace element data for all Caetano caldera samples.
*All Fe as FeO.
†Trace element ICP-MS data are from a duplicate of the same sample.

residue (Fig. 8). This compositional gap approximates what is observed in the intra-caldera tuff sequence (Fig. 6a); however, the crystallinity at which the gap occurs varies between the two starting compositions: ∼50–60% for the Carico Lake pluton (Fig. 8a), and ∼30% for the 'gap' rhyolite (Fig. 8b). The Carico Lake pluton starting composition produces the liquid–cumulate gap within the 'extraction window' of Dufek & Bachmann (2010), at which removal of interstitial melt is most mechanically efficient (50–70% crystallinity), whereas the 'gap' rhyolite starting composition produces a narrower range of appropriate compositions and at a lower crystallinity (Fig. 8).

Trace elements

Decreases in trace elements that are compatible in major and accessory phases in the Caetano Tuff (Sr—plagioclase, sanidine; Ba—sanidine, biotite; Zr—zircon; La—allanite), correspond to increases in relatively incompatible trace elements (Rb, U), yielding compositional arrays that are consistent with fractional crystallization (Fig. 9). Crystallization paths were modeled using the energy-constrained recharge, assimilation and fractional crystallization (EC-RAxFC) model of Bohrson & Spera (2007), with intermediate values for published trace element partition coefficients for Sr, Ba, and Rb (Nash & Crecraft, 1985), a representative modal mineralogy for Caetano
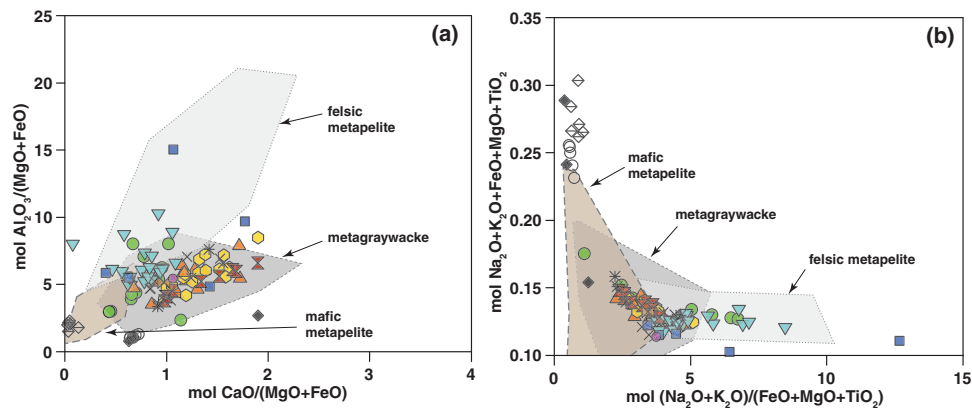
Fig. 5. Whole-rock geochemical data for Caetano samples compared with experimentally determined partial melt fields for metapelite and metagraywacke crustal sources [mica dehydration melting experiments of Patiño Douce & Johnston (1991); figure modified after Lee *et al.* (2003)]. Symbols are the same as those used in Fig. 4.
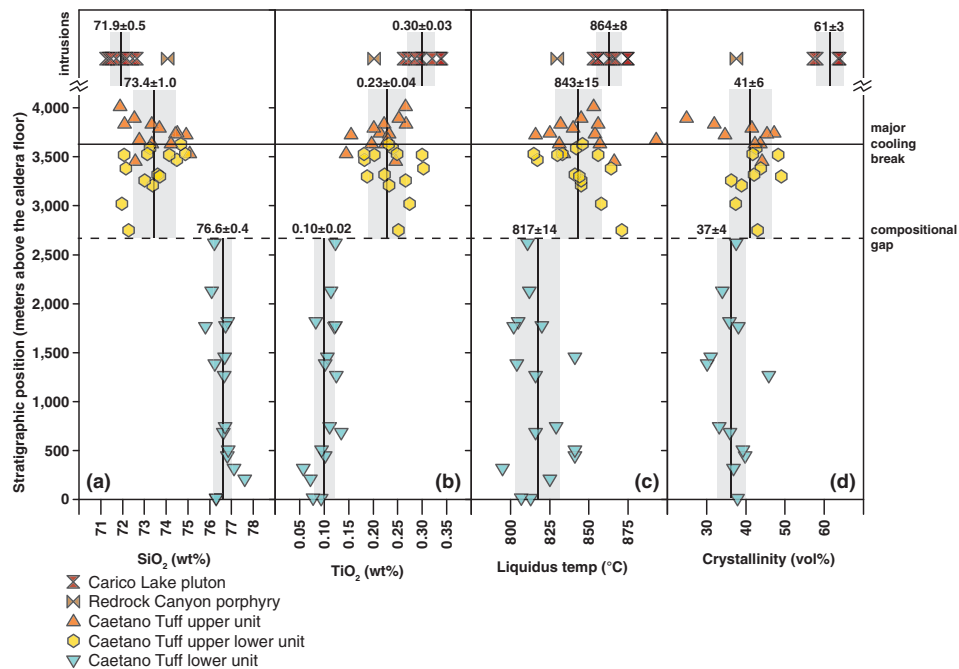
Fig. 6. Whole-rock zoning in the intra-caldera Caetano Tuff from 0 to 4000 m above the caldera floor. Large caldera intrusions (Carico Lake pluton, Redrock Canyon porphyry) are plotted above for reference. Vertical bars and gray shaded fields show the means and standard deviations for two compositional groups of Caetano Tuff and the Carico Lake pluton. (a) SiO_2 contents. (b) TiO_2 contents. (c) Liquidus temperatures. (d) Crystallinity. In all samples, crystallinity refers to the volume per cent of phenocrysts; in the pluton, the holocrystalline groundmass is not included.

Table 2: Summary of phenocryst contents and mineral modes of Caetano caldera units

Unit	Samples	Total phenocrysts		Average proportion of total phenocrysts (%)				
	(*n*)	volume (%)		Plagioclase	Sanidine	Quartz	Biotite	Other*
		Range	Average					
Caetano Tuff, upper unit	12	25–47	40	42	27	24	6	1
Caetano Tuff, upper lower unit	17	29–49	42	43	27	24	5	1
Caetano Tuff, lower unit	21	27–48	38	29	34	32	4	1
Caetano Tuff, outflow	16	32–43	38	35	31	27	6	1
Carico Lake pluton	4	57–64	61	40	35	20	2	3
Redrock Canyon porphyry	2	38–42	40	46	30	19	4	1
Ring-fracture intrusion	1		45	36	36	20	6	2

Total phenocryst contents and mineral modes were determined by point-counting single thin sections (∼700–800 points per thin section). See Supplementary Data Table 2 for compilation of all point-counting data for Caetano thin sections.
*Hornblende, orthopyroxene, Fe–Ti oxides, accessory phases.
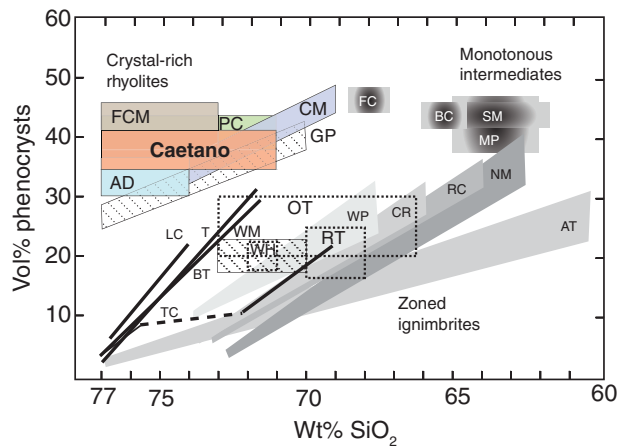
Fig. 7. Phenocryst and SiO₂ contents of ignimbrite deposits. Modified after Huber *et al.* (2012) to include examples of crystal-rich rhyolites and other tuffs that do not plot within the fields defined by monotonous intermediates or zoned ignimbrites. The Caetano Tuff and colored boxes are ignimbrites from the western Nevada volcanic field: FCM, Fish Creek Mountains Tuff; CM, tuff of Cove Mine; PC, tuff of Poco Canyon; AD, tuff of Arc Dome (Henry & John, 2013). The boxes with bold, short-dashed outlines are ignimbrites from the Taupo Volcanic Zone: OT, Ongatiti; RT, Rangitaiki; WH, Whakamaru (Matthews *et al.*, 2012; Cooper & Wilson, 2014). The boxes with thin, diagonal stripes are ignimbrites from the Southern Rocky Mountain volcanic field: GP, Grizzly Peak; WM, Wall Mountain (Fridrich *et al.*, 1991; Mills & Coleman, 2013; Lipman & Bachmann, 2015). Additional examples of crystal-rich rhyolitic ignimbrites in the central Nevada volcanic field are numerous (>17; see table 1 of Best *et al.*, 2013*c*; not included in this figure). Abbreviations from the original Huber *et al.* (2012) figure for ignimbrites of the western USA are as follows: LC, Lava Creek Tuff; T, Tshigere Member of the Bandelier Tuff; BT, Bishop Tuff; TC, Tiva Canyon Tuff; WP, Wason Park Tuff; CR, Carpenter Ridge Tuff; RC, Rat Creek Tuff; NM, Nelson Mountain Tuff; AT, Ammonia Tanks Tuff; FC, Fish Canyon Tuff; BC, Blue Creek; SM, Snowshoe Mountain Tuff; MP, Masonic Park Tuff.

rhyolites (40% plagioclase, 30% sanidine, 25% quartz, 5% biotite), and two starting compositions, the least evolved Carico Lake pluton sample and a hypothetical 'gap' melt that approximates the compositional gap observed in the Caetano Tuff (Fig. 10; Supplementary Data Appendix A). The trace element contents estimated for this gap melt (Rb = 175 ppm, Sr = 200 ppm, Ba = 875 ppm) are very similar to those of the outflow tuff sample used in the Rhyolite-MELTS major element modeling to approximate the gap melt composition (Rb = 152 ppm, Sr = 219 ppm, Ba = 845 ppm). The models were run with 0–25% contribution from assimilation and recharge; the crustal assimilant was approximated by metapelitic rocks exhumed from mid-crustal depths in the Ruby Mountains ~100 km east of the Caetano caldera (Lee *et al.*, 2003), and the composition of the recharge magma was constrained by sanidine Ba chemistry in the Caetano Tuff (see next section on Petrography and Mineral Chemistry). Evolution of the liquids and cumulates is essentially unaffected by ≤25% assimilation and recharge because of similar compositional and thermodynamic parameters for the three subsystems, and energy conservation that minimizes the
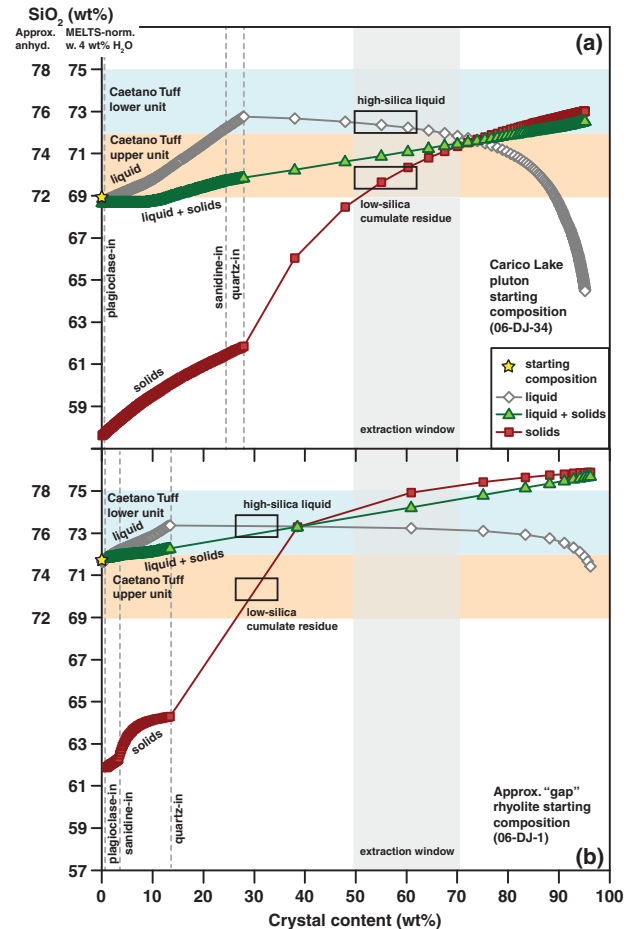

Fig. 8. Rhyolite-MELTS isobaric crystallization modeling. The runs were started at the liquidus temperatures with conditions at 1·5 kbar, 4 wt % H₂O, and ΔQFM = 0. Two starting compositions were modeled: (a) the least evolved Carico Lake pluton (sample 06-DJ-34) and (b) 'gap' rhyolite that is intermediate between the two compositional groups of tuff (approximated as outflow tuff sample 06-DJ-1). SiO₂ evolution with increasing degrees of crystallization is shown by the modeled curves for the liquid, liquid + solids, and solids (solids were approximated as plagioclase, sanidine and quartz, which constitute >90% of the equilibrium assemblage). The gray shaded field shows the extraction window (50–70% crystallinity) of Dufek & Bachmann (2010). The SiO₂ axes are labeled for both the MELTS-normalized SiO₂ content with 4 wt % H₂O and the approximate anhydrous SiO₂ content.

mass of anatectic melt mixed into the magma body (Bohrson & Spera, 2007). The EC-RAxFC curves are also virtually identical to those calculated using simple Rayleigh fractionation equations (without assimilation or recharge) to model liquids ($C_l/C_o = F^{D-1}$) and cumulate residues [$C_r/C_o = (1 - F^D)/1 - F$] (Supplementary Data Appendix A).
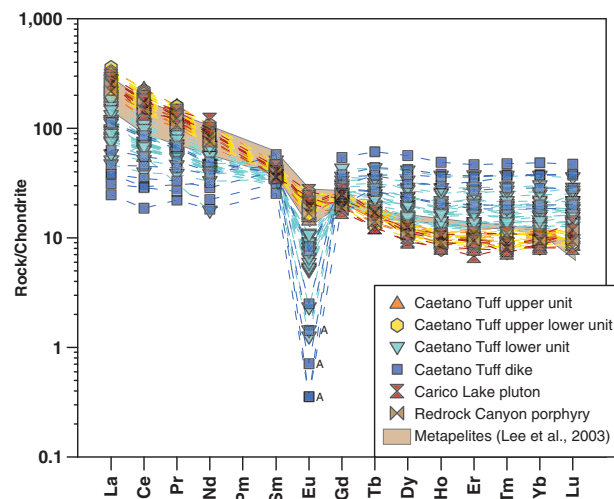
Rare earth elements
REE patterns exhibit a strong negative Eu anomaly that indicates significant feldspar fractionation in the Caetano Tuff (Fig. 11). Aphyric parts of the tuff dike exhibit the most extreme degree of fractionation, whereas the least evolved tuff is compositionally equivalent to the Carico
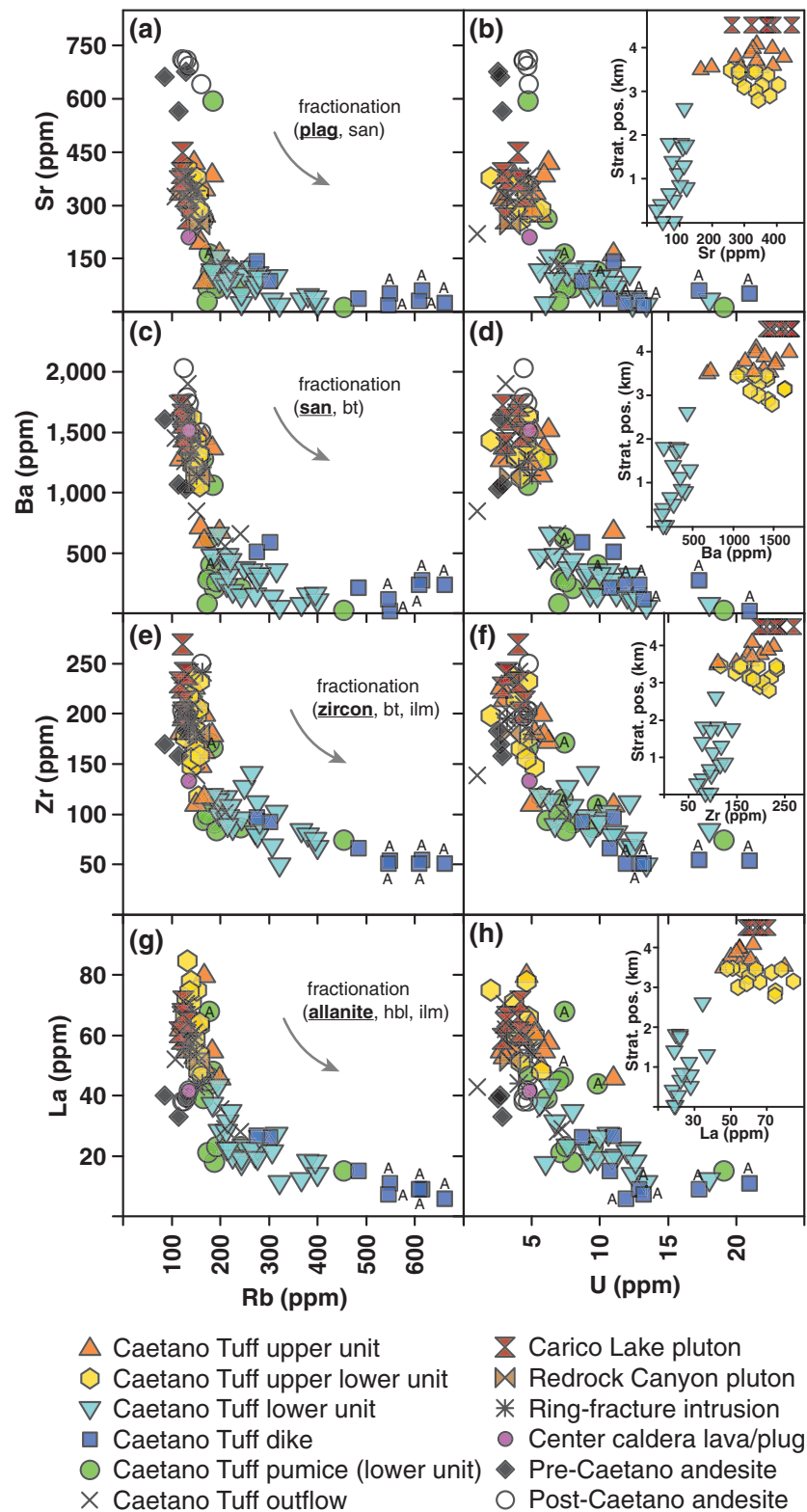
Fig. 9. Whole-rock trace element variation diagrams. Negative trends are indicative of fractional crystallization. Text in left panels indicates specific mineral phases with the largest influence on fractionation signatures: plagioclase (a, b), sanidine (c, d), zircon (e, f), and allanite (g, h). 'A' denotes aphyric samples. Insets in right panels illustrate compatible trace element variation with stratigraphic position in kilometers above the caldera floor.
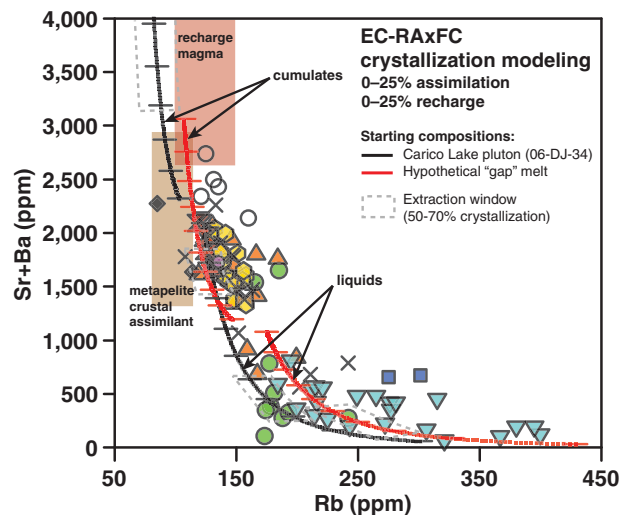
Fig. 10. Trace element fractional crystallization modeling for Rb, Sr and Ba. Curves were constructed using the EC-RAxFC model of Bohrson & Spera (2007). Two starting compositions were used to model the evolution of liquids and cumulates: the Carico Lake pluton (black curves) and a hypothetical 'gap' melt (red curves). Tick marks show 10% crystallization increments. The dashed boxes show the extraction window of Dufek & Bachmann (2010) at 50–70% crystallinity. The crustal assimilant field was approximated from metapelite basement rocks exposed in the Lamoille Canyon and East Humboldt Range ~100 km NE of Caetano (Rb 87–109 ppm, Sr 452–832 ppm, Ba 939–2046 ppm; Lee *et al.*, 2003) and the recharge magma field was approximated from Ba zoning in Caetano Tuff sanidines that indicate rim crystallization from a high-Ba rhyolite (Ba ~2000–4000 ppm; corresponds to Sr ~700–1500 ppm). Symbols are the same as those shown in Fig. 9.

Fig. 11. Chondrite-normalized whole-rock rare earth element diagram (chondrite concentrations after McDonough & Sun, 1995). 'A' denotes aphyric samples. The shaded field shows analyzed metapelites from Lamoille Canyon (Lee *et al.*, 2003).

Lake pluton and Redrock Canyon porphyry, requiring little to no fractionation (Fig. 11). As observed for Sr, Ba, and Rb (Fig. 10), the least evolved Caetano compositions are also very similar in their REE abundances to regional metapelites (Lee *et al.*, 2003). Depletions in light REE (LREE) and enrichments in heavy REE (HREE) in evolved

tuff compositions (Fig. 11) further support the role of accessory mineral crystallization, particularly LREE-rich allanite (e.g. Miller & Mittlefehldt, 1982), which is present in all Caetano rhyolites.

PETROGRAPHY AND MINERAL CHEMISTRY

The crystal-rich nature of the Caetano Tuff—with a mineral assemblage of plagioclase + sanidine + quartz + biotite ± orthopyroxene ± hornblende + Fe–Ti oxides + accessory zircon, apatite, allanite and pyrrhotite—make it particularly amenable to crystal-scale study. Modal abundances of quartz and sanidine decrease, whereas plagioclase increases upward within the intra-caldera tuff, and proportions of plagioclase, sanidine and quartz in the least evolved upper Caetano Tuff are very similar to those in the Carico Lake and Redrock Canyon intrusions (Fig. 12a–l; Table 2; Supplementary Data Table 2). Proportions of mafic minerals (biotite, orthopyroxene, hornblende, Fe–Ti oxides) increase in upper tuff exposures but are less abundant (pervasively resorbed) in the Carico Lake and Redrock Canyon intrusions (Fig. 12a–l; Table 2).

Plagioclase

Plagioclase occurs as oscillatory zoned, euhedral laths ~1–4 mm in length (e.g. Fig. 13a), anhedral fragments with complex internal zonation and resorption (Supplementary Data Appendix B), and in composite clusters with orthopyroxene in the upper tuff unit and ring-fracture intrusion (e.g. Fig. 13b; Appendix B). Plagioclase An histograms (Fig. 12m–r) indicate that the most evolved compositions (An ~10) are found in the lower tuff (Fig. 12q and r), with a shift to less evolved compositions (An ~30) in the upper tuff (Fig. 12o and p) and Carico Lake and Redrock Canyon intrusions (Fig. 12m and n). Excluding rare xenocrysts (e.g. Fig. 12p and q), overall An contents span a broad compositional range from oligoclase to andesine (An 10–55) (Fig. 12m–r; Table 3; Supplementary Data Table 3). No consistent core–rim zoning patterns are apparent in the Caetano Tuff; however, in the upper tuff unit the least evolved (An 40–55) plagioclase grains tend to be intergrown with orthopyroxene (Fig. 12o). In the Carico Lake and Redrock Canyon intrusions, plagioclase rims have consistently lower An contents than cores (Fig. 12m and n).

Sanidine

Sanidine phenocrysts are large (~1–5 mm) and commonly poikilitic with anhedral–subhedral plagioclase inclusions (e.g. Fig. 13c; Supplementary Data Appendix B). They are generally present as crystal fragments, with CL-dark cores mantled by CL-bright overgrowth rims. Using CL as a guide to target compositional boundaries, sanidine Ba zoning profiles were determined for the intra-caldera tuff and the Carico Lake and Redrock Canyon intrusions (representative zoning profiles for these units are shown in Fig. 12s–x; Table 4;
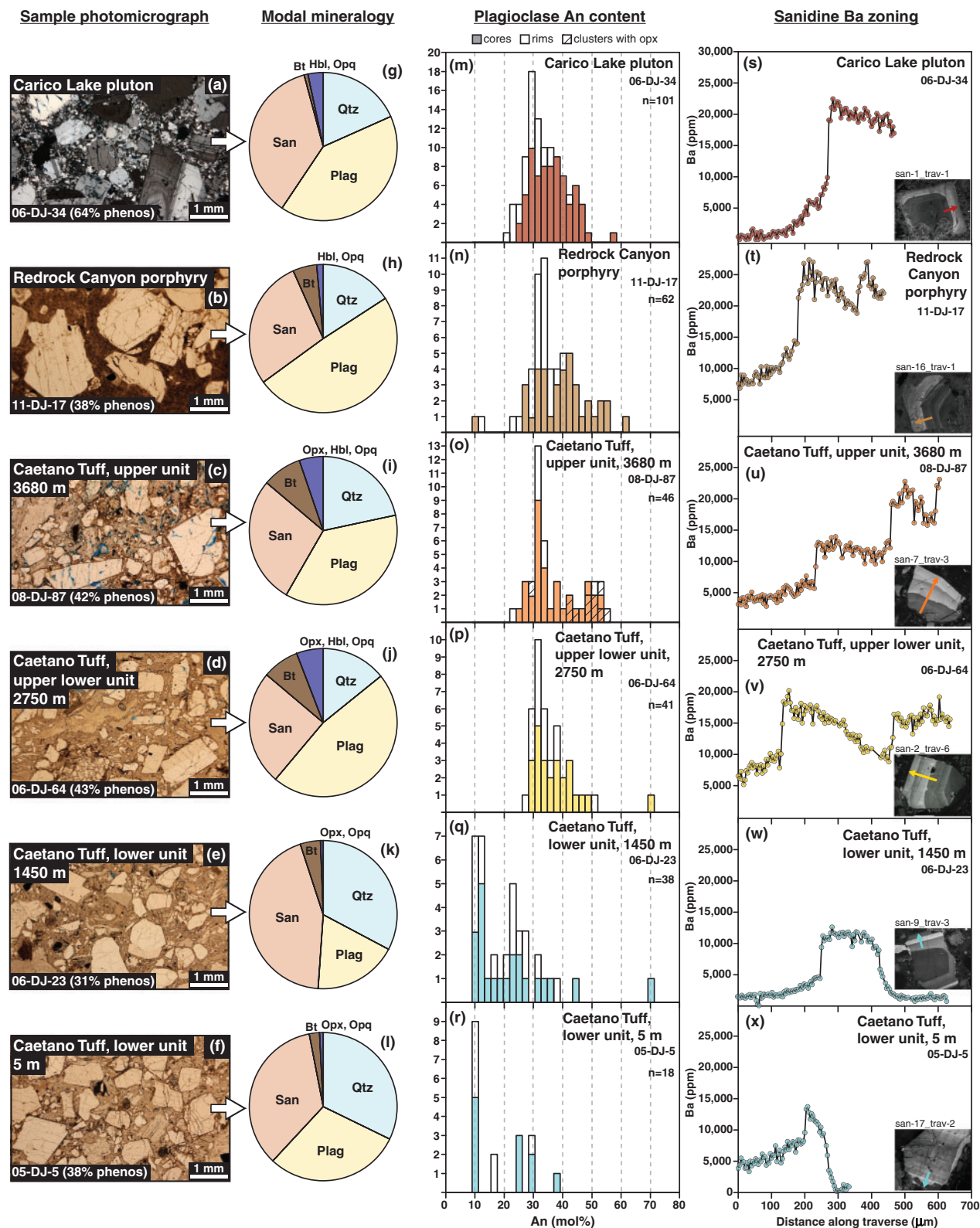
Fig. 12. Compilation of mineral data for different stratigraphic levels of the intra-caldera tuff and large caldera intrusions. Sample photomicrographs in cross-polarized light (a) and plane-polarized light (b–f) with total phenocryst volume per cent in parentheses; modal mineralogies (g–l) shown as the proportion of total phenocrysts: Plag, plagioclase; San, sanidine; Qtz, quartz; Bt, biotite; Hbl, hornblende; Opx, orthopyroxene; Opq, opaque minerals; plagioclase An content histograms (m)–(r); representative sanidine Ba zoning profiles (s–x), insets show cathodoluminescence images and colored arrows show the locations of profile traverses within sanidine phenocrysts.
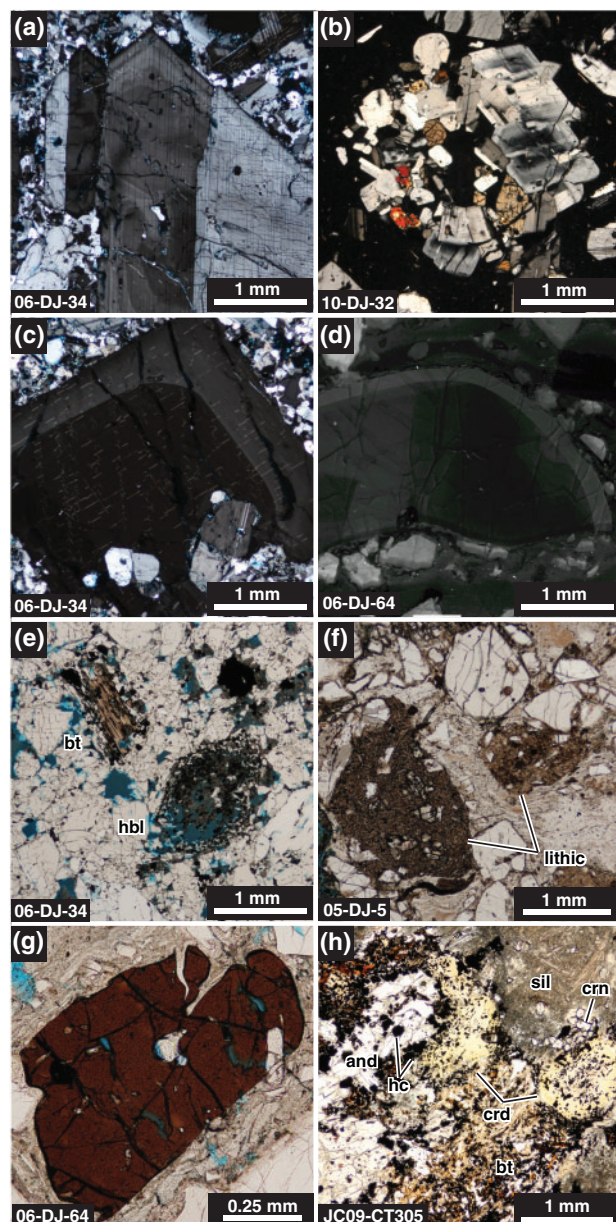
Fig. 13. Photomicrographs of selected features, imaged in cross-polarized light (xpl), plane-polarized light (ppl), and cathodoluminescence (CL). (a) Euhedral, oscillatory zoned plagioclase crystal (xpl); Carico Lake pluton. (b) Plagioclase and orthopyroxene crystal cluster (xpl); ring-fracture intrusion. (c) Zoned, poikilitic and slightly perthitic sanidine crystal (xpl); Carico Lake pluton. (d) Zoned, bright-rimmed quartz crystal (CL); upper lower tuff unit. (e) Resorbed biotite (bt) and hornblende (hbl) crystals with Fe–Ti oxide replacement textures (ppl); Carico Lake pluton. (f) Andesite lithic fragments containing orthopyroxene and clinopyroxene crystals (ppl); lower tuff unit. (g) Large pleochroic allanite crystal (ppl); upper lower tuff unit. (h) Metapelite xenolith with andalusite (and) that encloses and is surrounded by dark hercynite (hc) crystals, cordierite (crd) with pinite alteration, fibrolitic sillimanite (sil) with small crystals of corundum (crn), and biotite (bt) (ppl); xenolith in Carico Lake pluton.

Supplementary Data Table 4). Ba concentrations (up to $\sim$20 000–25 000 ppm) correlate with CL intensity (Fig. 12s–x and insets) and are typically independent of (or subtly correlated with) Na and K contents (Or $\sim$60–75;

Supplementary Data Table 4). The highest Ba zones in sanidine correspond to Ba concentrations of $\sim$2000–4000 ppm in equilibrium rhyolite melt, using intermediate sanidine–melt partition coefficients of $\sim$5–10 (Nash & Crecraft, 1985). One-dimensional infinite planar source diffusion modeling yields timescales of hundreds to thousands of years to generate the observed Ba zoning profiles at temperatures of 800–850°C (Supplementary Data Appendix C).

Quartz

Quartz is euhedral–subhedral ($\sim$1–3 mm), commonly with rounded and embayed margins. Like sanidine, quartz occurs as large crystal fragments with CL-bright overgrowth rims (e.g. Fig. 13d). Some quartz crystals are overprinted by a late resorption event, with prominent embayments and sieve textures that cross-cut CL-bright rims. Ti concentrations in quartz ($<$120 ppm) were too low to permit clear resolution of Ti zoning profiles by electron microprobe, but Ti contents are observed to increase in sharp steps rimward, analogous to Ba zoning profiles in Caetano sanidines (Fig. 12s–x).

Biotite

Subhedral–euhedral books of biotite ($\sim$0·3 to $>$1 mm wide) commonly exhibit deformation from welding in the Caetano Tuff, with foliation parallel to that of deformed glass shards. In the Redrock Canyon porphyry, biotite is mostly oxidized, and in the Carico Lake pluton pervasively sieved, with only relict biotite textures and Fe–Ti oxides remaining (e.g. Fig. 13e). In contrast, biotites in the ring-fracture intrusion are fresh, abundant, and commonly intergrown with plagioclase and pyroxene. Biotite mineral chemistry (Fig. 14a and b; Table 5; Supplementary Data Table 5) reveals a compositional array in the range of Mg# $\sim$15–70, TiO$_2$ $\sim$2–7 wt %, and Al$_2$O$_3$ $\sim$13–16 wt %. Although most biotites fall along a normal differentiation trend of increasing Mg# with increasing TiO$_2$, the Carico Lake pluton biotites define a reverse trend (Fig. 14a), possibly owing to removal of Ti from relict biotite grains during Fe–Ti oxide alteration (e.g. Fig. 13e).

Pyroxene

Orthopyroxene occurs as isolated phenocrysts ($\sim$0·3–1 mm), in composite clusters with plagioclase (e.g. Fig. 13b), and in andesite lithic fragments (e.g. Fig. 13f). Although absent in the Carico Lake and Redrock Canyon intrusions and sparse in the lower tuff unit, orthopyroxene is commonly observed in the upper unit and ring-fracture intrusion. In contrast to biotite, orthopyroxene is less evolved in the lower Caetano Tuff (Mg# $\sim$55–70) than in the upper Caetano Tuff or ring-fracture intrusion (Mg# $\sim$30–55) (Fig. 14c; Table 6; Supplementary Data Table 6). Analyses from isolated orthopyroxene crystals in the lower Caetano Tuff define ranges that are identical to or overlap those within andesite lithic fragments in the lower Caetano Tuff, with

Table 3: Summary of plagioclase electron microprobe data for Caetano caldera units

Unit	Sample	Cores/rims	Spots (n)	An (mol %)			Representative spot analysis	
				Range	Average	Median	Spot	SiO_2
Caetano Tuff, upper unit	08-DJ-87	cores	35	26–52	37	33	plag-1_s35	58·18
Caetano Tuff, upper unit	08-DJ-87	rims	11	22–55	37	32	plag-1_s36	60·27
Caetano Tuff, upper lower unit	06-DJ-64	cores	25	29–71	38	36	plag-2_s248	60·54
Caetano Tuff, upper lower unit	06-DJ-64	rims	16	28–50	33	32	plag-2_s249	60·40
Caetano Tuff, lower unit	06-DJ-23	cores	22	10–71	23	20	plag-10_s190	65·65
Caetano Tuff, lower unit	06-DJ-23	rims	16	10–37	20	22	plag-10_s191	65·41
Caetano Tuff, lower unit	05-DJ-5	cores	11	9–37	21	26	plag-1_s337	66·26
Caetano Tuff, lower unit	05-DJ-5	rims	7	9–29	14	10	plag-1_s338	66·30
Carico Lake pluton	06-DJ-34	cores	72	25–58	36	35	plag_2_s215	60·41
Carico Lake pluton	06-DJ-34	rims	30	21–43	30	30	plag_2_s214	60·82
Redrock Canyon porphyry	11-DJ-17	cores	65	11–62	41	42	plag-5_s48	58·86
Redrock Canyon porphyry	11-DJ-17	rims	24	12–41	31	33	plag-5_s49	60·50

|	Representative spot analysis						
	Al_2O_3	Na_2O	CaO	K_2O	MgO	FeO	Total
Caetano Tuff, upper unit	26·74	6·24	7·86	0·63	0·00	—	99·65
Caetano Tuff, upper unit	25·44	7·17	6·44	0·78	0·01	—	100·12
Caetano Tuff, upper lower unit	25·68	7·16	6·34	0·66	0·00	—	100·38
Caetano Tuff, upper lower unit	25·26	7·17	6·21	0·86	0·01	—	99·92
Caetano Tuff, lower unit	20·84	9·88	2·27	1·06	0·00	0·14	99·84
Caetano Tuff, lower unit	21·56	9·87	2·62	1·14	0·00	0·12	100·71
Caetano Tuff, lower unit	21·83	9·43	2·14	0·90	0·00	—	100·56
Caetano Tuff, lower unit	21·28	9·17	2·02	1·62	0·00	—	100·39
Carico Lake pluton	25·56	7·34	6·63	0·76	0·00	—	100·71
Carico Lake pluton	25·16	7·43	6·14	0·64	0·00	—	100·20
Redrock Canyon porphyry	25·74	7·00	7·86	0·83	0·01	0·15	100·45
Redrock Canyon porphyry	25·20	7·88	6·79	0·50	0·00	0·19	101·06

—, no data. See Supplementary Data Table 3 for compilation of all plagioclase electron microprobe data.

Table 4: Summary of representative sanidine electron microprobe traverses for Caetano caldera units

Unit	Sample	Traverse domain		Representative spot analysis in traverse			
		Low-Ba/ high-Ba	Traverse	Distance (μm)	SiO_2	Al_2O_3	K_2O
Caetano Tuff, upper unit	08-DJ-87	Low-Ba	san-7_trav-3	8	64·95	18·47	11·99
Caetano Tuff, upper unit	08-DJ-87	High-Ba	san-7_trav-3	604	64·86	19·31	10·88
Caetano Tuff, upper lower unit	06-DJ-64	Low-Ba	san-2_trav-6	20	64·71	18·71	12·17
Caetano Tuff, upper lower unit	06-DJ-64	High-Ba	san-2_trav-6	156	63·01	19·41	11·07
Caetano Tuff, lower unit	06-DJ-23	Low-Ba	san-9_trav-3	28	65·81	18·76	11·89
Caetano Tuff, lower unit	06-DJ-23	High-Ba	san-9_trav-3	336	63·84	18·97	11·46
Caetano Tuff, lower unit	05-DJ-5	Low-Ba	san-17_trav-2	20	64·66	18·44	11·29
Caetano Tuff, lower unit	05-DJ-5	High-Ba	san-17_trav-2	208	64·58	19·25	10·78
Carico Lake pluton	06-DJ-34	Low-Ba	san-1_trav-1	12	64·82	18·47	11·50
Carico Lake pluton	06-DJ-34	High-Ba	san-1_trav-1	284	62·83	19·48	10·95
Redrock Canyon porphyry	11-DJ-17	Low-Ba	san-16_trav-1	12	65·22	18·86	11·23
Redrock Canyon porphyry	11-DJ-17	High-Ba	san-16_trav-1	212	63·61	20·18	9·95

	Representative spot analysis in traverse							
	Na_2O	CaO	FeO	MgO	TiO_2	BaO	Total	Ba (ppm)
Caetano Tuff, upper unit	3·07	0·27	0·00	0·00	0·00	0·34	99·09	3075
Caetano Tuff, upper unit	2·91	0·24	0·13	0·00	0·05	2·58	100·96	23101
Caetano Tuff, upper lower unit	3·03	0·19	0·02	0·00	0·14	0·58	99·55	5182
Caetano Tuff, upper lower unit	2·91	0·40	0·12	0·00	0·10	2·25	99·27	20187
Caetano Tuff, lower unit	3·10	0·19	0·05	—	—	0·14	99·95	1288
Caetano Tuff, lower unit	3·05	0·19	0·10	—	—	1·32	98·93	11834
Caetano Tuff, lower unit	3·01	0·20	0·14	0·03	0·01	0·44	98·20	3909
Caetano Tuff, lower unit	3·26	0·26	0·10	0·02	0·00	1·53	99·78	13696
Carico Lake pluton	3·43	0·15	0·11	0·00	0·14	0·06	98·68	534
Carico Lake pluton	3·02	0·29	0·19	0·00	0·00	2·51	99·27	22465
Redrock Canyon porphyry	3·51	0·24	0·21	0·00	0·09	0·84	100·21	7513
Redrock Canyon porphyry	3·64	0·38	0·04	0·04	0·00	3·05	100·89	27334

— no data. See Supplementary Data Table 4 for compilation of all sanidine electron microprobe data.
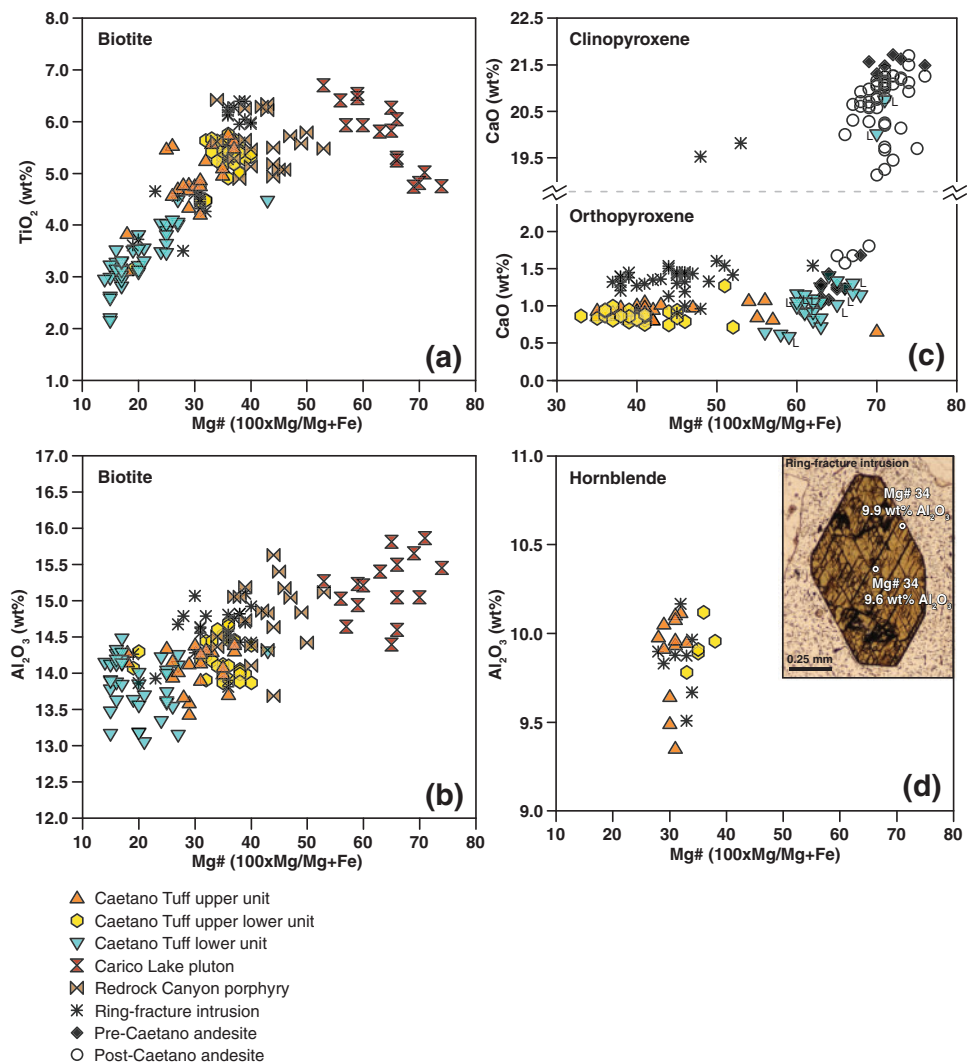
Fig. 14. Geochemical data for mafic mineral phases biotite (a, b); pyroxene (c), 'L' denotes analyses in lithic fragments; hornblende (d). Inset in (d) is a plane-polarized light photomicrograph of a typical hornblende crystal, showing its homogeneous (core and rim) composition in Mg# and wt % Al_2O_3.

similar pyroxene chemistry to the pre-Caetano andesite (Fig. 14c; Table 6). This evidence suggests that they are xenocrysts. Clinopyroxene (augite) is abundant in both the pre- and post-Caetano andesites and occurs as rare xenocrysts in the ring-fracture intrusion and lower Caetano Tuff unit (Fig. 14c).

Hornblende

Hornblende (up to 1–3 mm in length) occurs in the upper tuff unit, upper part of the lower tuff unit, and in the ring-fracture intrusion. In the Carico Lake and Redrock Canyon intrusions, primary hornblende is absent, but relict pseudomorphic textures are observed in the Carico Lake pluton (e.g. Fig. 13e). Hornblende compositions define a fairly precise mode at ~9·5–10 wt % Al_2O_3 and Mg# of ~30–35 (Fig. 14d; Table 7; Supplementary Data Table 7). Single hornblende phenocrysts are unzoned and lack resorption or dehydration rims that would indicate crystallization at multi-

depth levels in the crust or disequilibrium with their host magmas (e.g. inset photomicrograph in Fig. 14d). Thus, there appears to be less compositional variability in hornblende compared with other mafic mineral phases at Caetano (Fig. 14a–c). Using the amphibole barometer of Ridolfi *et al.* (2010) and average Al_2O_3 contents (9·5–10·0 wt %) for Caetano hornblendes yields crystallization pressures of ~2·2–2·5 kbar, or ~8–9 km depth (Supplementary Data Appendix D).

Fe–Ti oxides

Fe–Ti oxides (~10–500 μm) are ubiquitous. Whereas many ilmenite grains in the Caetano Tuff are fresh, most magnetite grains are oxy-exsolved with pervasive ilmenite exsolution in lamellar and patchy replacement textures. Lower exposures of the Caetano Tuff have fewer oxides (excluding those in lithic fragments) and lower ilmenite/magnetite ratios compared with upper tuff exposures. Most ilmenite and magnetite pairs in the

Table 5: Summary of biotite electron microprobe data for Caetano caldera units

Unit	Sample	Cores/rims	Spots (n)	Mg# [100Mg/(Mg + Fe)]			Representative spot analysis	
				Range	Average	Median	Spot	SiO₂
Caetano Tuff, upper unit	08-DJ-87	cores	12	18–37	31	31	biot-10_s22	34·71
Caetano Tuff, upper unit	08-DJ-87	rims	10	18–37	29	30	biot-10_s23	34·77
Caetano Tuff, upper lower unit	06-DJ-64	cores	16	20–40	35	36	biot-5_s36	34·89
Caetano Tuff, upper lower unit	06-DJ-64	rims	15	19–39	34	35	biot-5_s37	35·51
Caetano Tuff, lower unit	06-DJ-23	cores	13	15–27	21	21	biot-8_s48	34·54
Caetano Tuff, lower unit	06-DJ-23	rims	10	15–27	22	23	biot-8_s49	34·36
Caetano Tuff, lower unit	05-DJ-5	cores	12	15–43	20	17	biot-6_s45	34·80
Caetano Tuff, lower unit	05-DJ-5	rims	5	15–17	17	17	biot-6_s46	34·40
Carico Lake pluton	06-DJ-34	cores	14	53–71	63	65	biot-1_s63	38·33
Carico Lake pluton	06-DJ-34	rims	2	60–74	67	67	biot-1_s64	37·76
Redrock Canyon porphyry	11-DJ-17	cores	10	34–49	41	43	biot-5_s75	35·09
Redrock Canyon porphyry	11-DJ-17	rims	10	39–53	44	43	biot-5_s76	34·47
Ring-fracture intrusion	10-DJ-32	cores	13	20–39	33	36	biot-8_s81	34·35
Ring-fracture intrusion	10-DJ-32	rims	13	19–40	33	36	biot-8_s82	34·63

	Representative spot analysis							
	FeO	Al₂O₃	K₂O	MgO	TiO₂	Na₂O	MnO	CaO	Total
Caetano Tuff, upper unit	27·61	14·30	8·74	7·56	5·57	0·32	0·14	0·00	98·93
Caetano Tuff, upper unit	27·57	14·32	8·76	7·36	5·24	0·31	0·26	0·02	98·63
Caetano Tuff, upper lower unit	25·29	14·46	9·09	8·22	5·18	0·22	0·29	0·00	97·65
Caetano Tuff, upper lower unit	23·96	14·45	8·91	7·99	5·34	0·34	0·21	0·01	96·71
Caetano Tuff, lower unit	31·33	14·00	8·71	4·34	3·20	0·40	0·43	0·03	97·00
Caetano Tuff, lower unit	30·49	13·84	8·65	4·28	3·08	0·45	0·48	0·03	95·67
Caetano Tuff, lower unit	33·64	14·17	8·71	3·88	2·92	0·39	0·44	0·10	99·04
Caetano Tuff, lower unit	33·95	14·18	8·84	3·89	3·02	0·38	0·51	0·02	99·19
Carico Lake pluton	11·92	15·86	9·46	16·45	5·02	0·53	0·11	0·04	97·71
Carico Lake pluton	11·17	15·45	9·46	17·94	4·75	0·45	0·08	0·02	97·09
Redrock Canyon porphyry	23·68	14·32	8·53	10·19	6·34	0·38	0·17	0·09	98·79
Redrock Canyon porphyry	25·84	14·37	7·51	9·85	5·13	0·25	0·24	0·08	97·75
Ring-fracture intrusion	23·93	14·75	8·62	8·04	6·27	0·39	0·15	0·02	96·52
Ring-fracture intrusion	22·74	14·91	9·00	8·36	5·95	0·38	0·20	0·00	96·17

See Supplementary Data Table 5 for compilation of all biotite electron microprobe data.

Caetano Tuff fail the Mg/Mn partitioning test for equilibrium (Bacon & Hirschmann, 1988), except for one sample from the upper part of the lower tuff unit. For this sample, average ilmenite and magnetite compositions of relatively fresh (non-exsolved) grains correspond to an equilibrium temperature of 745°C, oxygen fugacity of –1·07 (log fO_2 ΔNNO), and TiO₂ activity of 0·4, using the Fe–Ti oxide geothermometer of Ghiorso & Evans (2008).

Accessory minerals
Zircon, apatite, allanite and pyrrhotite are the main accessory phases in the Caetano Tuff. Zircon occurs as euhedral crystals (∼100–300 μm long) that are commonly attached to orthopyroxene and Fe–Ti oxide clusters or included in biotite and plagioclase grains. Apatite forms small (<10–50 μm) inclusions in biotite, and more rarely hornblende and allanite grains. Allanite occurs as subhedral–euhedral crystals (∼100 to >500 μm long) that are strongly pleochroic from reddish-brown to light tan (e.g. Fig. 13g). Pyrrhotite occurs as rounded to elongate inclusions (∼5–30 μm in diameter) in ilmenite, orthopyroxene, and plagioclase phenocrysts, and as small (tens of micrometers) crystals in groundmass glasses. Topaz was found in the heavy mineral separate

of a basal Caetano Tuff vitrophyre but was not observed in thin sections or hand samples. Broken topaz sprays suggest vapor-phase precipitation of topaz in tuff vesicles (e.g. Christiansen *et al.*, 1986).

Metapelite xenoliths
Metapelite xenoliths in the Carico Lake pluton have diverse mineral modes and textures, with varying proportions of K-feldspar, biotite, andalusite, silliminate, corundum, cordierite, hercynite (Fe-spinel), Fe–Ti oxides ± quartz and plagioclase (e.g. Fig. 13h). Biotite and sillimanite display varying degrees of schistosity, and most biotite is pervasively altered to Fe–Ti oxides. Intergrown K-feldspar and sparse quartz and plagioclase occur in lenses (several millimeters wide) that are elongated parallel to biotite and sillimanite foliation in some xenoliths. Large (∼1–4 mm) porphyroblasts of corundum (colorless to pleochroic blue) and poikioblastic andalusite are common. Many andalusite porphyroblasts contain hercynite inclusions and/or are surrounded by hercynite rims (e.g. Fig. 13h). Sillimanite is ubiquitous and typically fibrolitic (occasionally in coarser needles), and some fibrolite mats contain small crystals of corundum (e.g. Fig. 13h). Most cordierite is altered to pale yellow–orange pinnite (e.g. Fig. 13h),

Table 6: Summary of pyroxene electron microprobe data for Caetano caldera units

Unit	Sample	Cores/rims	Spots (*n*)	Mg# [100Mg/(Mg + Fe)]			Representative spot analysis
				Range	Average	Median	Spot
Caetano Tuff, upper unit	08-DJ-87	cores	23	35–70	43	40	pyx-clus-4_s12
Caetano Tuff, upper unit	08-DJ-87	rims	12	36–43	41	41	pyx-clus-4_s13
Caetano Tuff, upper lower unit	06-DJ-64	cores	13	36–52	41	40	pyx_clus-1_s275
Caetano Tuff, upper lower unit	06-DJ-64	rims	13	33–45	39	38	pyx_clus-1_s274
Caetano Tuff, lower unit	06-DJ-23	cores	5	61–63	62	62	pyx-2_s208
Caetano Tuff, lower unit	06-DJ-23	rims	4	60–65	62	61	pyx-2_s209
Caetano Tuff, lower unit	06-DJ-23	lithic cores	11	59–71	64	62	pyx_lith_w_pyx-2_s187
Caetano Tuff, lower unit	05-DJ-5	cores	3	58–68	63	62	pyx-4_s332
Caetano Tuff, lower unit	05-DJ-5	rims	3	56–66	62	63	pyx-4_s333
Caetano Tuff, lower unit	05-DJ-5	lithic cores	2	63–64	64	64	pyx_lith_wpyx-1_s312
Ring-fracture intrusion	10-DJ-32	cores	24	37–62	45	45	pyx-1_s45
Ring-fracture intrusion	10-DJ-32	rims	11	38–53	45	45	pyx-1_s46
Pre-Caetano andesite	H05-52	cores	11	61–71	65	64	pyx-2_s129
Pre-Caetano andesite	H05-52	rims	9	65–76	68	66	pyx-2_s130
Post-Caetano andesite	11-DJ-28	cores	32	65–75	70	70	pyx-4_s55
Post-Caetano andesite	11-DJ-28	rims	19	67–76	72	71	pyx-4_s56

|	Representative spot analysis							
	SiO_2	FeO	MgO	CaO	Al_2O_3	TiO_2	MnO	Total
Caetano Tuff, upper unit	49·89	34·20	13·28	1·05	0·74	—	—	99·16
Caetano Tuff, upper unit	50·40	33·64	13·55	0·95	0·59	—	—	99·13
Caetano Tuff, upper lower unit	49·79	35·88	13·43	0·82	0·91	—	—	100·83
Caetano Tuff, upper lower unit	49·90	35·97	13·04	0·79	1·19	—	—	100·88
Caetano Tuff, lower unit	52·36	22·89	21·35	1·08	0·82	0·09	0·86	99·46
Caetano Tuff, lower unit	52·19	23·59	20·25	1·15	0·95	0·13	0·95	99·21
Caetano Tuff, lower unit	52·44	23·18	20·91	1·02	0·59	0·13	1·00	99·27
Caetano Tuff, lower unit	54·09	23·76	21·89	0·80	0·73	—	—	101·27
Caetano Tuff, lower unit	54·54	23·26	22·13	0·71	0·51	—	—	101·15
Caetano Tuff, lower unit	54·25	22·70	21·39	1·25	0·67	—	—	100·25
Ring-fracture intrusion	50·45	32·13	14·56	1·44	0·76	0·16	1·01	100·52
Ring-fracture intrusion	50·33	31·62	14·75	1·45	0·82	0·14	0·95	100·06
Pre-Caetano andesite	52·84	22·51	21·83	1·30	0·74	0·21	0·91	100·33
Pre-Caetano andesite	53·82	20·89	22·85	1·23	0·78	0·22	0·76	100·55
Pre-Caetano andesite	52·16	9·74	14·80	20·14	1·71	0·60	0·36	99·51
Pre-Caetano andesite	52·08	10·60	14·53	20·21	1·66	0·63	0·33	100·03

—, no data. See Supplementary Data Table 6 for compilation of all pyroxene electron microprobe data.

Table 7: Summary of hornblende electron microprobe data for Caetano caldera units

Unit	Sample	Cores/rims	Spots (*n*)	Mg# [100Mg/(Mg + Fe)]		Al_2O_3 (wt %)	
				Range	Average	Range	Average
Caetano Tuff, upper unit	08-DJ-87	cores	6	29–33	31	9·5–10·1	9·9
Caetano Tuff, upper unit	08-DJ-87	rims	6	29–31	30	9·4–10·1	9·8
Caetano Tuff, upper lower unit	06-DJ-64	cores	3	35–38	36	9·9–10·0	9·9
Caetano Tuff, upper lower unit	06-DJ-64	rims	2	33–36	35	9·8–10·1	10·0
Ring-fracture intrusion	10-DJ-32	cores	4	28–34	32	9·5–10·2	9·8
Ring-fracture intrusion	10-DJ-32	rims	4	29–34	32	9·8–10·0	9·9

	Representative spot analysis									
	Spot	SiO_2	FeO	CaO	Al_2O_3	MgO	TiO_2	Na_2O	K_2O	MnO	Total
Caetano Tuff, upper unit	hbe-2_s1	42·25	26·34	10·19	9·93	6·64	2·08	1·63	1·18	0·48	100·72
Caetano Tuff, upper unit	hbe-2_s2	41·73	27·13	10·18	9·91	6·23	1·70	1·91	1·28	0·55	100·63
Caetano Tuff, upper lower unit	hbe-2_s11	42·04	23·53	10·72	9·89	7·14	1·91	1·79	1·29	0·56	98·86
Caetano Tuff, upper lower unit	hbe-2_s12	41·60	23·70	10·58	9·78	6·66	2·18	1·75	1·32	0·50	98·06
Ring-fracture intrusion	hbe-3_s71	41·61	26·23	10·72	9·90	5·82	1·72	1·74	1·08	0·68	99·50
Ring-fracture intrusion	hbe-3_s72	41·46	25·88	10·67	9·83	5·81	1·71	1·58	1·25	0·73	98·93

See Supplementary Data Table 7 for compilation of all hornblende electron microprobe data and Appendix D for barometry calculations.
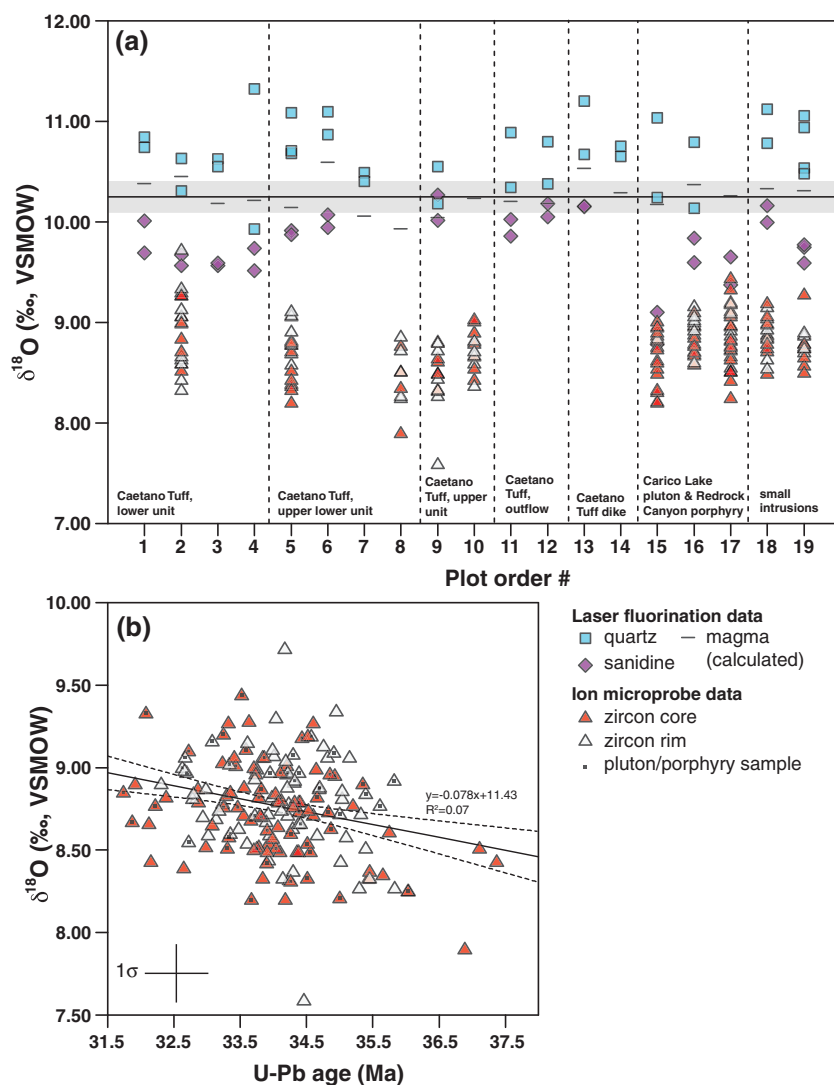
Fig. 15. Oxygen isotope data. (a) Laser fluorination data (quartz and sanidine analyses) and ion microprobe data (zircon core and rim analyses), plotted for single samples (plot order number corresponds to Table 8). Magma $\delta^{18}O$ values were calculated from phenocryst analyses for each sample, and the average and standard deviation of all Caetano samples is shown by the horizontal black line and gray shaded field ($\delta^{18}O_{magma} = 10\cdot2 \pm 0\cdot2‰$). (b) $\delta^{18}O$ vs U–Pb age for single-spot ion microprobe analyses of zircon cores and rims. Linear regression (continuous black line) and 95% confidence band (dashed black lines) reveals no statistically significant trend ($R^2 = 0\cdot07$).

although fresh cordierite is also present in some xenoliths, often concentrated in zones surrounded by K-feldspar.

OXYGEN ISOTOPES

Phenocrysts from all stratigraphic levels of the intracaldera Caetano Tuff have uniformly high $\delta^{18}O$ compositions, with average $\delta^{18}O_{quartz} = 10\cdot4–10\cdot9‰$, $\delta^{18}O_{sanidine} = 9\cdot5–10\cdot1‰$, and $\delta^{18}O_{zircon} = 8\cdot4–8\cdot9‰$ (Fig. 15a; Table 8; Supplementary Data Table 8). Calculated magma (melt) $\delta^{18}O$ values in equilibrium with quartz and zircon phenocrysts at temperatures of 800–870°C ($\Delta^{18}O_{melt-zircon} = 1\cdot4–1\cdot6‰$ and $\Delta^{18}O_{quartz-melt} = 0\cdot3–0\cdot5‰$; Trail *et al.*, 2009), indicate that the Caetano Tuff magma chamber had a very high supracrustal $\delta^{18}O$ value of

$10\cdot2 \pm 0\cdot2‰$ (Fig. 15a; see next section on isotopic modeling). Phenocryst analyses for the Carico Lake pluton, Redrock Canyon porphyry, and small caldera intrusions (Fig. 15a; Table 8) yielded calculated magma $\delta^{18}O$ values that are identical to those of the Caetano Tuff. Analyses of metapelite xenoliths in the Carico Lake pluton returned diverse and high-$\delta^{18}O$ values, in the range of $\delta^{18}O_{whole-rock} = 7\cdot2–10\cdot4‰$ (Table 8).

Core–rim $\delta^{18}O$ data from single zircons were combined with U–Pb ages for the same spots for a subset of extrusive and intrusive Caetano units (Fig. 15b; Supplementary Data Table 9). Most zircons (cores and rims) have a narrow $\delta^{18}O$ range (8·3–9·3‰), despite U–Pb age spans of several million years (Fig. 15b; see section below on zircon U–Pb geochronology). Likewise, $\delta^{18}O$ zoning between core and rim analyses in single

Table 8: Summary of O isotope data for Caetano caldera samples

Unit	Description	Sample	Plot order no.	$\delta^{18}O$ (‰, VSMOW) average Quartz	Sanidine	Zircon	Plagioclase	Whole-rock	Magma $\delta^{18}O$ (‰, calc.)
Caetano Tuff, lower unit	North Toiyabe, 200 m	H03-84	1	10.79	9.85	—	—	—	10.38
Caetano Tuff, lower unit	North Toiyabe, 1260 m	H03-82	2	10.47	9.62	8.92	—	—	10.45
Caetano Tuff, lower unit	Moss Creek	05-DJ-14	3	10.59	9.57	—	—	—	10.18
Caetano Tuff, lower unit	Cedars Quad, Shoshone	H03-88B	4	10.62	9.62	—	—	—	10.21
Caetano Tuff, upper lower unit	Rocky Pass, 3020 m	05-DJ-27	5	10.69	9.89	8.69	—	—	10.14
Caetano Tuff, upper lower unit	North Toiyabe, 3540 m	00-DJ-34	6	10.98	10.00	—	—	—	10.59
Caetano Tuff, upper lower unit	Moss Creek	H03-94	7	10.44	—	—	—	—	10.05
Caetano Tuff, upper lower unit	Rocky Pass, 3590 m	05-DJ-23	8	—	—	8.46	—	—	9.93
Caetano Tuff, upper unit	Tub Spring, 3686 m	08-DJ-88*	9	10.36	10.14	8.59	—	—	10.04
Caetano Tuff, upper unit	Rocky Pass, 3750 m	05-DJ-26	10	—	—	8.72	—	—	10.23
Caetano Tuff, outflow	Cedars Quad	H03-89	11	10.61	9.94	—	—	—	10.20
Caetano Tuff, outflow	Golconda Canyon	Tru5-4	12	10.59	10.11	—	—	—	10.18
Caetano Tuff dike	Fortress, crystal-poor	H07-52	13	10.94	10.15	—	—	—	10.53
Caetano Tuff dike	Fortress, crystal-rich	H07-55B	14	10.70	—	—	—	—	10.29
Redrock Canyon porphyry	Carico Lake Valley	07-DJ-12	15	10.64	8.94	8.66	—	—	10.17
Redrock Canyon porphyry	Redrock Canyon	11-DJ-17	16	10.46	9.71	8.86	—	—	10.37
Carico Lake pluton	Carico Lake valley	H03-96†	17	—	9.51	8.86	—	—	10.26
Ring-fracture intrusion	Tci-1, northern caldera wall	06-DJ-82	18	10.95	10.07	8.86	—	—	10.33
Center caldera lava/plug	Tci-2, Carico Lake valley	11-DJ-3	19	10.75	9.70	8.78	—	—	10.31
Xenolith in Carico Lake pluton	Metapelite xenolith	JC09-CT305	—	—	—	—	—	7.21	7.21
Xenolith in Carico Lake pluton	Metapelite xenolith	JC09-CT304	—	—	—	—	—	10.38	10.38
Xenolith in Carico Lake pluton	Metapelite xenolith	11-DJ-6	—	—	—	—	—	8.78	8.78
Pre-Caetano andesite	Toiyabe, caldera floor	H05-52	—	—	—	—	9.48	—	9.48
Post-Caetano andesite	west of Redrock Canyon	09-DJ-77	—	—	—	—	9.09	—	9.09
Hydrothermally altered caldera rocks									
Caetano Tuff, upper unit	Advanced argillic	09-DJ-48	—	—	—	—	—	1.74	—
Caetano Tuff, upper unit	Advanced argillic	09-DJ-44	—	—	—	—	—	4.13	—
Caetano Tuff, upper unit	Advanced argillic	08-DJ-53	—	—	—	—	—	4.66	—
Caetano Tuff, upper unit	Advanced argillic	09-DJ-25	—	—	—	—	—	3.99	—
Caetano Tuff, upper unit	Advanced argillic	09-DJ-47	—	—	—	—	—	3.73	—
Ring-fracture intrusion	Advanced argillic	09-DJ-52	—	—	—	—	—	3.68	—
Redrock Canyon porphyry	Hydrothermal breccia	09-DJ-21	—	—	—	—	—	3.02	—
Redrock Canyon porphyry	Advanced argillic	08-DJ-38	—	—	—	—	—	4.39	—
Redrock Canyon porphyry	Advanced argillic	08-DJ-114	—	—	—	—	—	2.29	—
Redrock Canyon porphyry	Hydrothermal breccia	07-DJ-30	—	—	—	—	—	2.56	—
Redrock Canyon porphyry	Advanced argillic	08-DJ-50	—	—	—	—	—	3.39	—

Plot order number corresponds to Fig. 15a. Magma $\delta^{18}O$ values were calculated from phenocryst analyses, with fractionation factors from Trail et al. (2009) for zircon ($\Delta^{18}O$melt–zircon = 1.4–1.6‰) and quartz ($\Delta^{18}O$quartz–melt = 0.3–0.5‰) for liquidus temperatures of 800–870°C. For samples without zircon or quartz analyses (xenoliths, andesites), magmatic values were approximated from whole-rock and plagioclase values. Depths in descriptions of tuff units refer to their stratigraphic position in meters above the caldera floor. For hydrothermally altered caldera rocks, advanced argillic alteration assemblages are characterized by quartz–kaolinite–oxidized pyrite. —, no data. See Supplementary Data Table 8 for compilation of all Caetano $\delta^{18}O$ data.
*Zircon data from 08-DJ-87.
†Zircon data from 11-DJ-27 and JC06-CT109.

Table 9: Summary of Sr, Nd, and Pb isotope data for Caetano caldera samples

Unit	Description	Sample	$^{87}Sr/^{86}Sr_i$	$^{143}Nd/^{144}Nd$	εNd^*	$^{206}Pb/^{204}Pb$	$^{207}Pb/^{204}Pb$	$^{208}Pb/^{204}Pb$
Caetano Tuff, lower unit	North Toiyabe, 1260 m	H03-82	0·70682	0·51234	−4·93	19·282	15·691	39·017
Caetano Tuff, upper unit	Tub Spring, 3686 m	08-DJ-87	0·70722	0·51234	−4·94	19·282	15·681	38·984
Carico Lake pluton	Carico Lake valley	JC06-CT109	0·70673	0·51235	−4·77	19·272	15·686	39·002
Redrock Canyon porphyry	Redrock Canyon	11-DJ-17	0·70697	0·51234	−4·91	19·280	15·680	38·987
Xenolith in Carico Lake pluton	Metapelite xenolith	JC09-CT305	0·71623	0·51171	−17·30	19·484	15·693	39·184
Xenolith in Carico Lake pluton	Metapelite xenolith	JC09-CT304	0·76165	0·51185	−14·44	19·807	15·767	39·476
Pre-Caetano andesite	Toiyabe, caldera floor	H05-52	0·70761	0·51221	−7·47	19·357	15·698	39·116
Post-Caetano andesite	West of Redrock Canyon	09-DJ-77	0·70701	0·51233	−5·27	19·279	15·683	39·004

All isotopic ratios are initial ratios, corrected for radiogenic ingrowth of daughter products ^{87}Sr, ^{143}Nd, ^{206}Pb, ^{207}Pb, and ^{208}Pb using an age of 34·0 Ma for the tuff, pluton and porphyry units, 35·2 Ma for the pre-Caetano andesite, and 33·5 Ma for the post-Caetano andesite. Decay constants: $\lambda^{87}Rb = 1·42 \times 10^{-11}$ a^{-1}, $\lambda^{147}Sm = 6·54 \times 10^{-12}$ a^{-1}, $\lambda^{238}U = 1·55125 \times 10^{-10}$ a^{-1}, $\lambda^{235}U = 9·8485 \times 10^{-10}$ a^{-1}, and $\lambda^{232}Th = 4·9475 \times 10^{-11}$ a^{-1}. Depths in descriptions of tuff units refer to their stratigraphic positions in meters above the caldera floor.
*εNd is calculated from the initial sample/chondrite $^{43}Nd/^{144}Nd$ ratios, using present-day chondrite CHUR values of $^{147}Sm/^{144}Nd = 0·1967$ and $^{143}Nd/^{144}Nd = 0·512638$ to calculate inital CHUR values.

zircons is usually small (<0·3‰) (Supplementary Data Table 9). Zircon populations of the Caetano Tuff and large caldera intrusions are indistinguishable in $\delta^{18}O$ or U–Pb age (Fig. 15b; Supplementary Data Table 9), and no temporal trends in $\delta^{18}O$ are evident, in terms of either the relative stratigraphic position of erupted and intruded units (Fig. 15a) or absolute U–Pb ages (Fig. 15b).

## STRONTIUM AND NEODYMIUM ISOTOPES AND ISOTOPIC MODELING

All Caetano units have $^{87}Sr/^{86}Sr_i > 0·706$, and thus are more radiogenic than the accreted arc terranes and arc-related rocks west of the 0·706 line in the Nevada Great Basin (Farmer & DePaolo, 1983; Kistler, 1990; Fig. 1; Table 9). However, the Caetano units have less radiogenic isotope ratios (with the exception of the xenoliths) than the Precambrian cratonic basement in eastern Nevada and western Utah, defined by $^{87}Sr/^{86}Sr_i > 0·708$ and $\varepsilon Nd < −7$ (Farmer & DePaolo, 1983; Bennett & DePaolo, 1987; Fig. 1). The intermediate isotopic ratios of the Caetano magmas ($^{87}Sr/^{86}Sr_i = 0·7067–0·7072$, $\varepsilon Nd = −4·7$ to $−4·9$) correspond to a transition zone along an $\sim$100 km wide crustal section in central Nevada, bounded by the 0·706 isopleth to the west and the cratonic Precambrian basement to the east, which roughly coincides with the trace of the Roberts Mountain thrust in central and eastern Nevada (Farmer & DePaolo, 1983; Bennett & DePaolo, 1987; Fig. 1). This transition is tracked by zircons in Proterozoic, Mesozoic and Tertiary granitic intrusions that ascended through Precambrian cratonic basement in eastern Nevada ($\delta^{18}O_{zircon} \approx 6–7‰$), transitional continental margin sedimentary and metasedimentary rocks in central Nevada ($\delta^{18}O_{zircon} \approx 7–10‰$), and volcanic arc and accreted arc terranes in western Nevada ($\delta^{18}O_{zircon} \approx 5–6‰$) (King et al., 2004; Fig. 1). The highest $\delta^{18}O$ values coincide with the location of the Caetano caldera ($\delta^{18}O_{zircon} \approx 8·3–9·3‰$; Fig. 15b).

The presence of high-$\delta^{18}O$ zircons, and corresponding magmatic $\delta^{18}O$ values of $10·2 \pm 0·2‰$ for the Caetano Tuff (Fig. 15a), place it among the most ^{18}O-enriched ignimbrites documented in the Nevada Great Basin (see Larson & Taylor, 1986; Hart, 1997). This unique isotopic signature provides unequivocal evidence for its derivation from a high-$\delta^{18}O$ supracrustal source. A schematic representation of the crustal architecture beneath Caetano at $\sim$34 Ma, with approximate depths and isotopic characteristics of the different crustal and mantle reservoirs, is depicted in Fig. 16. Late Proterozoic–Paleozoic sediments were deposited on the rifted North American cratonic margin and subsequently buried and metamorphosed during Late Paleozoic and Mesozoic compression and thrust faulting [see geotectonic review by Dickinson (2006)]. Thrust thickened metasedimentary basement ($\sim$40–50 km beneath Caetano; Coney & Harms, 1984) was then variably intruded, melted and replaced by large Mesozoic and Tertiary granitic bodies, which constrain its isotopic composition (Farmer & de Paolo, 1983; Wright & Wooden, 1991; King et al., 2004). The U–Pb age spectra of inherited Precambrian zircons in Caetano units are strikingly similar to spectra from Proterozoic siliciclastic rocks exposed in eastern Nevada, supporting derivation of Caetano magmas from anatexis of equivalent metasedimentary rocks at depth (Fig. 16 inset).

Isotopic mixing models were constructed using this schematic crustal architecture and regional Sr–Nd–O isotope datasets for granites (King et al., 2004) and basalts (Cousens et al., 2012) to constrain crustal and mantle end-member compositions (Fig. 17; Supplementary
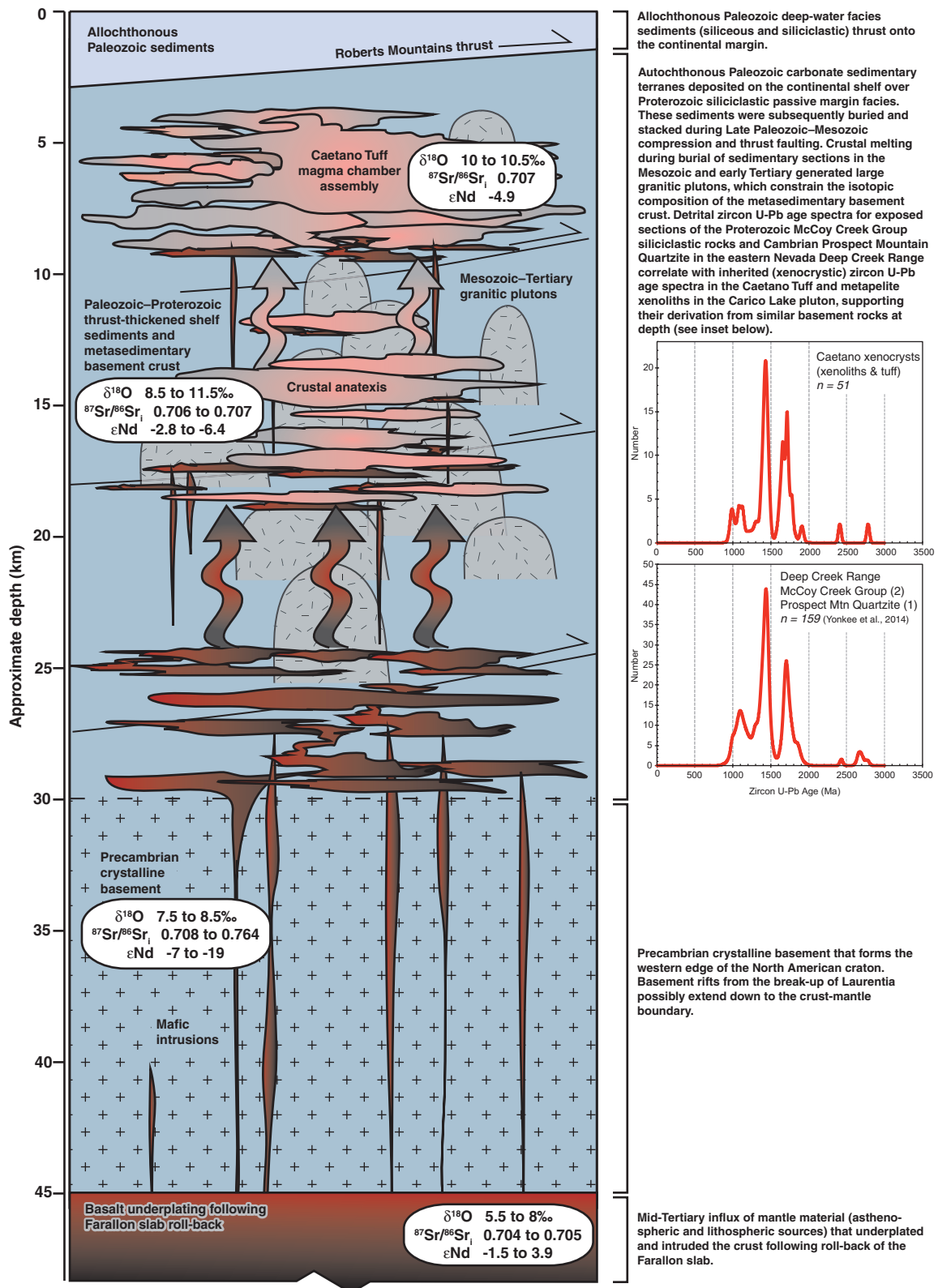
Fig. 16. Schematic crustal architecture showing the approximate depths and isotopic characteristics of reservoirs selected for Sr–Nd–O isotope modeling. Descriptions included in panels to the right. Isotope data from Farmer & DePaolo (1983), Wright & Wooden (1991), Wooden *et al.* (1999), King *et al.* (2004), and Cousens *et al.* (2012).
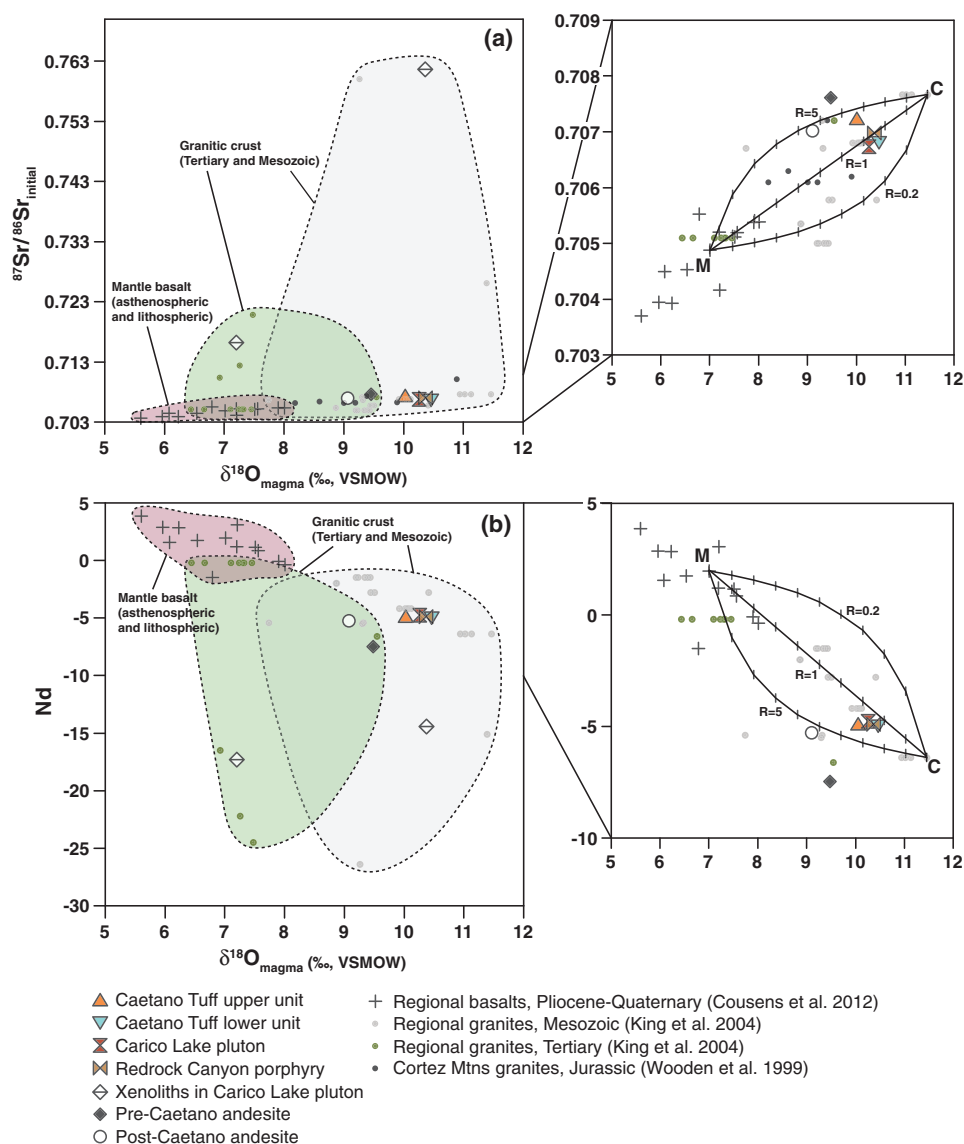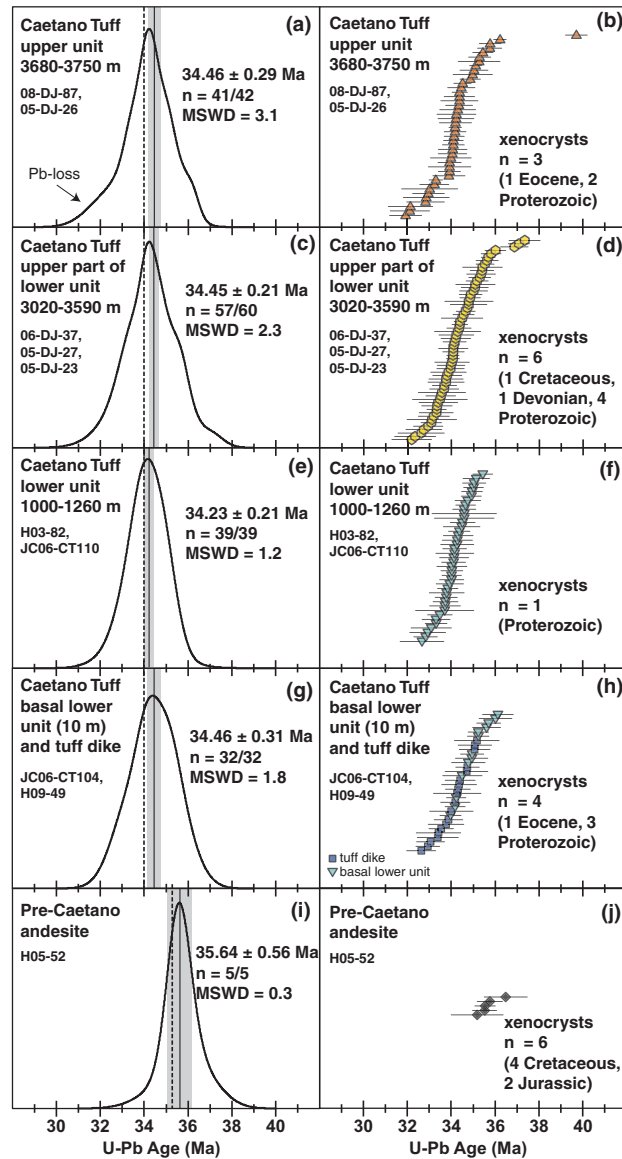
Fig. 17. Caetano isotope data combined with regional datasets for Sr–O (a) and Nd–O (b). Insets show the results of isotopic mixing models to constrain crust ('C') and mantle ('M') contributions to the Caetano magmas. Mixing hyperbolae were calculated using R_{crust}/R_{mantle} concentrations of 0·2, 1 and 5.

Data Appendix E). Excluding a few highly radiogenic outliers (Caetano xenoliths, a few analyses from Mesozoic and Tertiary granites), the magmatic rocks generally fall along a linear trend between mantle-derived basalt and granitic crustal compositions, spanning a range of $^{87}Sr/^{86}Sr_i = 0.704–0.708$, $\varepsilon Nd = -6.4$ to 3·8, and $\delta^{18}O_{magma} = 5.6–11.5‰$ (Fig. 17). The metapelite xenoliths are not suitable crustal end-members for isotopic modeling owing to their extremely radiogenic and generally lower $\delta^{18}O$ compositions relative to Caetano rhyolites (Fig. 17). A Mesozoic granite intruded along a similar longitude to the Caetano caldera was selected for the crustal end-member (Supplementary Data Appendix E). Because the isotopic composition of the mid-Tertiary mantle beneath Caetano is not known (there were no basalt eruptions at this time), the mantle

end-member was based on a suite of younger Pliocene–Quaternary basalts in the Nevada Great Basin that have isotopic compositions intermediate between lithospheric and asthenospheric mantle sources (Supplementary Data Appendix E).

Based on these constraints, mixing models indicate ~70–80% crust and ~20–30% mantle in the Caetano rhyolites (Fig. 17 insets; Supplementary Data Appendix E). Crustal proportions could be as high as 100% if using granitic compositions with $\delta^{18}O_{magma} = 10.0$– 10·5‰, for which there are ample examples in the Nevada Great Basin (Fig. 17 and insets). The ~20–30% mantle contribution estimate is close to the maximum allowed by the isotopic ranges of the Caetano magmas. Shifting the mantle end-member to the most primitive (asthenospheric) basalt composition would result in a

Extrusive Caetano units   **Intrusive Caetano units**
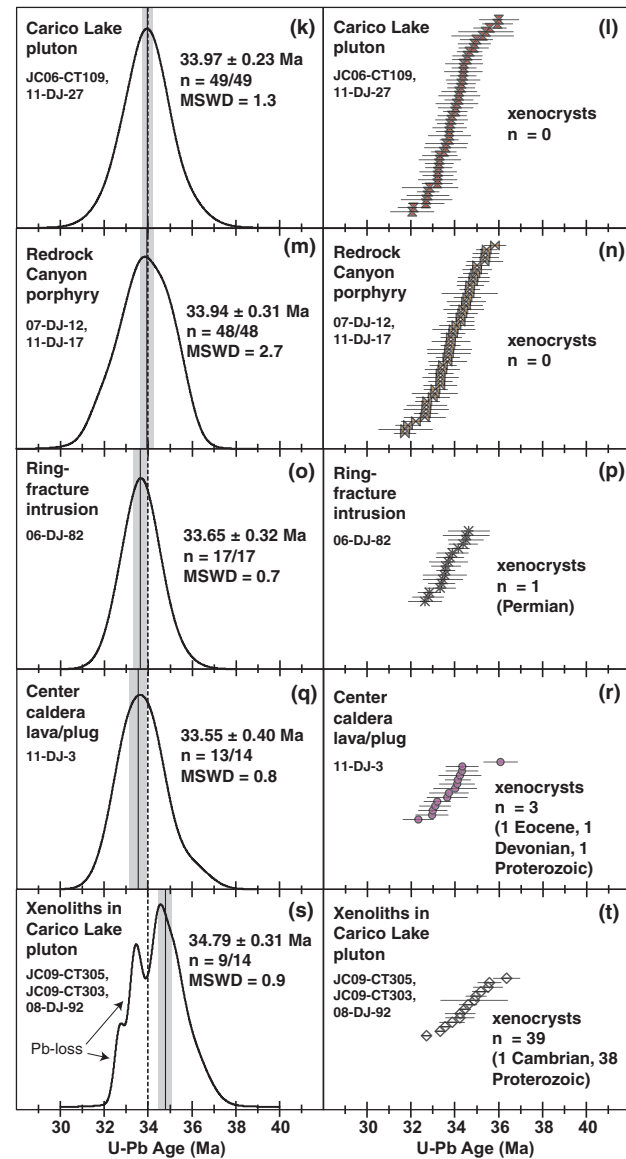
Fig. 18. Compilation of zircon U–Pb age data, divided into extrusive (a–j) and intrusive (k–t) panel pairs showing probability density function and rank order plots. Continuous vertical lines and gray fields in the probability density function plots show error-weighted mean U–Pb ages and 95% confidence intervals. Thin dashed vertical lines show the $^{40}Ar/^{39}Ar$ age for the Caetano rhyolites (34·0 Ma) and the pre-Caetano andesite (35·2 Ma). Error bars in rank order plots are 1σ errors for single U–Pb analyses.

less than 10–15% change in these estimates. In contrast, numerous Tertiary granites (mostly located west of the 0·706 line in Nevada) fall within the isotopic fields defined by the basalts (Fig. 17), permitting a much greater (up to 100%) mantle component in their sources.

ZIRCON U–PB GEOCHRONOLOGY AND TRACE ELEMENT GEOCHEMISTRY

Zircon $^{206}Pb/^{238}U$ ages

To compare U–Pb age spectra for different stratigraphic levels of the intra-caldera Caetano Tuff (and thus

different stratigraphic levels of the Caetano Tuff magma chamber), $^{206}Pb/^{238}U$ zircon age data for single samples were grouped into sections that define their relative positions in meters above the caldera floor: the upper unit (3680–3750 m), upper part of the lower unit (3020–3590 m), mid–lower unit (1000–1260 m), basal lower unit (10 m) and tuff dike (Fig. 18a–h; Table 10). We note that although single samples are heterogeneous (Table 10; Supplementary Data Table 10), this approach allows us to compare caldera-wide variations that would otherwise be difficult to resolve in the scope of single samples that reflect localized conditions of zircon crystallization and inheritance. The combined U–Pb age datasets reveal unimodal and overlapping weighted-

Table 10: Summary of $^{206}Pb/^{238}U$ zircon ages for Caetano caldera samples

Unit	Sample	Latitude (°N)	Longitude (°W)	Location	Age (Ma)	95% CI	n	MSWD	Xenocrysts
Caetano Tuff, upper unit	08-DJ-87	40·1264	−116·8269	Tub Spring, 3686 m	34·62	0·32	28/29	3·1	1E, 2P
Caetano Tuff, upper unit	*05-DJ-26*	*40·1696*	*−116·8062*	*Rocky Pass, 3750 m*	*33·33*	*0·46*	*13/13*	*1·1*	*0*
Caetano Tuff, upper unit, combined	—	—	—	—	**34·46**	**0·29**	**41/42**	**3·1**	**1E, 2P**
Caetano Tuff, upper lower unit	06-DJ-37	40·1165	−116·8112	Tub Spring, 3530 m	34·01	0·33	18/18	1·0	1D
Caetano Tuff, upper lower unit	05-DJ-27	40·1713	−116·8153	Rocky Pass, 3020 m	33·90	0·35	17/18	1·1	1P
Caetano Tuff, upper lower unit	05-DJ-23	40·1700	−116·8084	Rocky Pass, 3590 m	34·69	0·32	22/24	3·4	1Ct, 3P
Caetano Tuff, upper lower unit, combined	—	—	—	—	**34·45**	**0·21**	**57/60**	**2·3**	**1Ct, 1D, 4P**
Caetano Tuff, lower unit	H03-82	40·1587	−116·6634	Toiyabe Range, 1260 m	34·29	0·30	21/21	1·5	0
Caetano Tuff, lower unit	JC06-CT110	40·1219	−116·7329	west side of Toiyabe Range, ∼1000 m	34·13	0·31	18/18	0·9	1P
Caetano Tuff, lower unit, combined	—	—	—	—	**34·23**	**0·21**	**39/39**	**1·2**	**1P**
Caetano Tuff, basal lower unit	JC06-CT104	40·0815	−116·6835	north of Wenban Spring, 10 m	34·91	0·42	13/13	1·5	2P
Caetano Tuff dike	H09-49	40·1764	−116·6544	Fortress Fault, outcrop	33·97	0·32	19/19	1·1	1E, 1P
Caetano Tuff, basal lower unit and tuff dike, combined	—	—	—	—	**34·46**	**0·31**	**32/32**	**1·8**	**1E, 3P**
Carico Lake pluton	JC06-CT109	40·1387	−116·8567	Carico Lake Valley	33·86	0·28	28/28	0·9	0
Carico Lake pluton	11-DJ-27	40·1312	−116·8394	east side of Carico Lake Valley	34·08	0·42	21/21	1·9	0
Carico Lake pluton, combined	—	—	—	—	**33·97**	**0·23**	**49/49**	**1·3**	**0**
Xenoliths in Carico Lake pluton	JC09-CT305	40·1485	−116·8461	Carico Lake Valley	33·70	2·0	3/4	5·2	1C, 24P
Xenoliths in Carico Lake pluton	JC09-CT303	40·1485	−116·8461	Carico Lake Valley	34·40	1·2	5/5	6	10P
Xenoliths in Carico Lake pluton	08-DJ-92	40·1395	−116·8569	Carico Lake Valley	34·74	0·73	5/5	1·4	4P
Xenoliths in Carico Lake pluton, combined	—	—	—	—	**34·79**	**0·31**	**9/14**	**0·9**	**1C, 38P**
Redrock Canyon porphyry	07-DJ-12	40·1414	−116·9023	Carico Lake Valley	34·07	0·37	28/28	2·3	0
Redrock Canyon porphyry	*11-DJ-17*	*40·1838*	*−116·9822*	*east side of Redrock Canyon*	*33·71*	*0·58*	*20/20*	*3·1*	*0*
Redrock Canyon porphyry, combined	—	—	—	—	**33·94**	**0·31**	**48/48**	**2·7**	**0**
Ring-fracture intrusion	*06-DJ-82*	*40·2135*	*−116·8591*	*Tci-1, north Carico Lake Valley*	*33·65*	*0·32*	*17/17*	*0·7*	*1Pm*
Center caldera lava/plug	11-DJ-3	40·1649	−116·8979	Tci-2, west side of Carico Lake Valley	**33·55**	**0·40**	**13/14**	**0·8**	**1E, 1D, 1P**
Pre-Caetano andesite	H05-52	40·1267	−116·6845	near Francis Cabin, Toiyabe Range	**35·64**	**0·56**	**5/5**	**0·3**	**5Ct, 1J**

Bold text indicates single and combined units plotted in Fig. 18. Italics indicates samples identified with Pb loss in CA study; additional CA and non-CA dates have been given by Watts *et al.* (2016). Depths in tuff unit location descriptions refer to their stratigraphic positions in meters above the caldera floor. Ages are error-weighted mean U–Pb ages for single and combined zircon samples. Uncertainties shown are 95% confidence intervals. *n*, number of single analyses used to define weighted-mean U–Pb ages. MSWD, mean square weighted deviations. E, Eocene; Ct, Cretaceous; J, Jurassic; Pm, Permian; D, Devonian; C, Cambrian; P, Proterozoic. See Supplementary Data Table 10 for compilation of all zircon U–Pb data.

mean U–Pb ages of 34·2–34·5 ± 0·2–0·3 Ma for the intra-caldera Caetano Tuff (Fig. 18a–h). Zircon populations in the upper tuff units (Fig. 18a–d) are characterized by more antecrysts and xenocrysts (36–39 Ma), apparent as distinct outliers (Fig. 18d) and asymmetries in probability density functions, which contribute to higher MSWDs (Fig. 18a and c). Some samples also yield younger zircon U–Pb ages (32 Ma), apparent as irregular young 'shoulders' (Fig. 18a). SHRIMP-RG analyses of a subset of these zircons after thermal annealing and chemical abrasion (CA) are largely devoid of anomalously young U–Pb ages, indicating Pb loss in some Caetano zircons (Watts *et al.*, 2016; CA data not presented here). Most analyzed tuff samples contain xenocrystic zircon (∼5–10% of zircon populations), mainly of Proterozoic (∼850–1700 Ma), and fewer of Paleozoic, Mesozoic, and Cenozoic age (Table 10). The Pre-Caetano andesite is dominated by xenocrystic zircon (∼55% Mesozoic); however, a few Eocene zircons correspond to a weighted-mean U–Pb age of 35·6 ± 0·6 Ma that is comparable with the oldest U–Pb ages observed in Caetano Tuff zircons (Fig. 18a–j).

Large caldera intrusions have identical weighted-mean U–Pb ages of 33·9–34·0 ± 0·2–0·3 Ma (Fig. 18k–n). Small caldera intrusions have slightly younger mean U–Pb ages of 33·5–33·6 ± 0·3–0·4 Ma (Fig. 18o–r). Thus, compared to the Caetano Tuff, intrusive caldera units have overall younger U–Pb ages. However, in the case of the Carico Lake and Redrock Canyon intrusions, this may be due in part to a lack of older inherited zircon (Fig. 18k–n; Table 10). Older zircon U–Pb ages in the Caetano Tuff (36–38 Ma) that overlap younger zircon ages within uncertainty (i.e. not distinct outliers) are averaged into weighted-mean U–Pb age calculations, resulting in ∼0·2–0·5 Ma older ages relative to the Carico Lake and Redrock Canyon intrusions. The lack of xenocrystic zircon in the large caldera intrusions is an important feature of the U–Pb datasets. Given the large sample sizes (*n* = 49, *n* = 48), if xenocrysts were present, they should be represented in the datasets (and indeed are for every unit except the Carico Lake pluton and Redrock Canyon porphyry; Table 10).

Xenoliths within the Carico Lake pluton yield zircons that are overwhelmingly xenocrystic (75% Proterozoic), but a few euhedral zircon crystals returned U–Pb ages consistent with the age of Caetano magmatism, 34·8 ± 0·3 Ma (Fig. 18s and t). Pb loss is an apparent problem in xenolithic zircons based on the presence of an anomalously young age peak at about 33 Ma (Fig. 18s) that is 1 Myr younger than the age of the pluton that hosts them (Fig. 18k); however, the relatively small sample size of Eocene-age zircon (*n* = 14) may also contribute to the apparent age bimodality.

Comparison of zircon ^{206}Pb/^{238}U ages with sanidine ^{40}Ar/^{39}Ar ages

Single crystal sanidine ^{40}Ar/^{39}Ar dates on all parts of the Caetano magmatic system (pre-caldera, caldera-forming,

post-caldera) provide a robust framework in which to integrate zircon U–Pb geochronology datasets (Table 11; ^{40}Ar/^{39}Ar ages calculated based on Fish Canyon Tuff sanidine = 28·201 Ma; Kuiper *et al.*, 2008). Sanidine ^{40}Ar/^{39}Ar dates on the Caetano Tuff yield an error-weighted mean age of 34·00 ± 0·03 Ma (*n* = 14 samples, 2σ SE). This group includes the upper and lower tuff units, tuff dike, and outflow tuff (Table 11). In comparison, weighted-mean zircon U–Pb ages for the Caetano Tuff are 0·2–0·5 Myr older (Fig. 18a–h; Table 10). The Carico Lake pluton has a sanidine ^{40}Ar/^{39}Ar date that is identical to that of the Caetano Tuff, 34·00 ± 0·05 Ma (Table 11). Its weighted-mean zircon U–Pb age of 34·0 ± 0·2 Ma is indistinguishable within analytical uncertainty. Likewise, the Redrock Canyon porphyry has a sanidine ^{40}Ar/^{39}Ar date of 33·90 ± 0·04 Ma, identical to its U–Pb age of 33·9 ± 0·3 Ma. The plagioclase ^{40}Ar/^{39}Ar date for the pre-Caetano andesite (35·21 ± 0·18 Ma) is comparable with the weighted mean U–Pb age of 35·6 ± 0·6 Ma for the few Eocene zircons found in this unit (Fig. 18i and j).

Trace elements

Zircons from all stratigraphic levels of the intra-caldera Caetano Tuff over a 3600 m depth range define similar and overlapping fields for all trace elements and trace element ratios (Fig. 19a–f). Intrusive Caetano units have zircons that fall within the same compositional fields as extrusive units with somewhat more restricted Eu/Eu* ranges (i.e. <0·50) (Fig. 19). The center caldera lava/plug, which has a distinctly higher SiO$_2$ content than other intrusive caldera units (Fig. 4a), has zircons that fall along the lower boundary of the Eu/Eu* vs Hf trend (Fig. 19h) with generally lower Th/U (<0·50) (Fig. 19j), similar to observations for the more evolved Caetano Tuff dike (Fig. 19d).

Caetano zircons have highly heterogeneous Ti contents (0·8–26 ppm) and corresponding crystallization temperatures (620–960°C) (Supplementary Data Fig. 1; Supplementary Data Table 11). Cores, interiors and rims give comparably large ranges in temperature, and no coherent pattern of up- or down-temperature crystallization is apparent in single core–rim zoning profiles (Supplementary Data Fig. 2). All units have some zircons with Ti-temperatures exceeding zircon saturation and liquidus temperatures, indicating zircon growth from magmatic compositions disparate from those represented by Caetano whole-rock compositions. Zircons from the most evolved lower Caetano Tuff have a greater proportion of low (<700°C) Ti-in-zircon temperatures relative to less evolved upper tuff exposures (Supplementary Data Fig. 1).

DISCUSSION

In the following discussion, we integrate results from whole-rock, mineral and accessory mineral datasets to define the petrologic evolution of the magmatic system that sourced the >1100 km^3 Caetano Tuff. The

Table 11: Summary of $^{40}Ar/^{39}Ar$ ages for Caetano caldera samples

Unit	Sample	Latitude (°N)	Longitude (°W)	Location	Mineral	*n* or % ^{39}Ar	Age (Ma)	2σ error
Caetano Tuff, upper unit	00-DJ-34	40·1550	–116·6210	Toiyabe Range, 3540 m	sanidine	12	34·01	0·08
Caetano Tuff, upper unit	00-DJ-34	40·1550	–116·6210	Toiyabe Range, 3540 m	sanidine	14	34·03	0·05
Caetano Tuff, upper unit	08-DJ-88*	40·1264	–116·8269	Tub Spring, 3686 m	sanidine	15	33·91	0·05
Caetano Tuff, upper lower unit	05-DJ-27	40·1713	–116·8153	Rocky Pass, 3020 m	sanidine	10	34·07	0·08
Caetano Tuff, upper lower unit	H03-94	40·2075	–117·0288	Moss Creek	sanidine	14	33·96	0·05
Caetano Tuff, lower unit	H03-82	40·1587	–116·6634	Toiyabe Range, 1260 m	sanidine	13	34·04	0·05
Caetano Tuff, lower unit	H03-84	40·1640	–116·6770	Toiyabe Range	sanidine	10	33·93	0·06
Caetano Tuff, lower unit	H03-88B	40·1170	–117·0370	Cedars quad on saddle west of Elephants Head	sanidine	9	34·03	0·07
Caetano Tuff, lower unit	05-DJ-14	40·2086	–117·0382	Shoshone Range	sanidine	10	34·07	0·07
Caetano Tuff dike	H07-55	40·1764	–116·6544	Toiyabe Range	sanidine	14	34·00	0·05
Caetano Tuff dike	CH05-102-2150	40·1667	–116·6308	Fortress fault, cuttings CH05-102 2150–2170 feet	sanidine	9	33·99	0·08
Caetano Tuff dike	H07-52	40·1746	–116·6471	Fortress fault, outcrop	sanidine	15	34·01	0·05
Caetano Tuff, outflow	H03-89	40·0966	–117·0576	Cedars area, Shoshone Range	sanidine	21	34·05	0·05
Caetano Tuff, outflow	Tru5-4	40·3245	–117·5937	Golconda Canyon, Tobin Range	sanidine	10	33·97	0·06
Caetano Tuff, combined	—	—	—	—	—	—	34·00 ± 0·03†	—
Carico Lake pluton	H03-96	40·1670	–116·8490	Carico Lake Valley	sanidine	15	34·00	0·05
Redrock Canyon porphyry	07-DJ-12	40·1414	–116·9023	Carico Lake Valley	sanidine	19	33·90	0·04
Ring-fracture intrusion	06-DJ-82	40·2135	–116·8591	Carico Lake Valley	sanidine	14	33·96	0·05
Pre-Caetano andesite	H05-52	40·1267	–116·6845	near Francis Cabin, Toiyabe Range	plagioclase	78	35·21	0·18
Post-Caetano andesite	09-DJ-77	40·2229	–117·0780	interbedded with Bates Mtn Tuff	plagioclase	91	33·55	0·04

All analyses performed at New Mexico Geochronological Research Laboratory, New Mexico Institute of Mining and Technology. Data compiled from John *et al.* (2008), Henry & John (2013) and this study. All analyses calculated or recalculated for a neutron flux monitor age of 28·201 Ma for Fish Canyon Tuff sanidine (FC-1) after Kuiper *et al.* (2008). Depths in tuff unit location descriptions refer to their stratigraphic positions in meters above the caldera floor. *n*, number of single grains used to define weighted-mean age in single crystal fusion sanidine analyses. % ^{39}Ar is percentage of ^{39}Ar used in step-heating plateau age determinations for plagioclase analyses.

*Equivalent to sample 08-DJ-87.

†Error-weighted mean $^{40}Ar/^{39}Ar$ sanidine age and 2σ standard error for combined tuff samples.
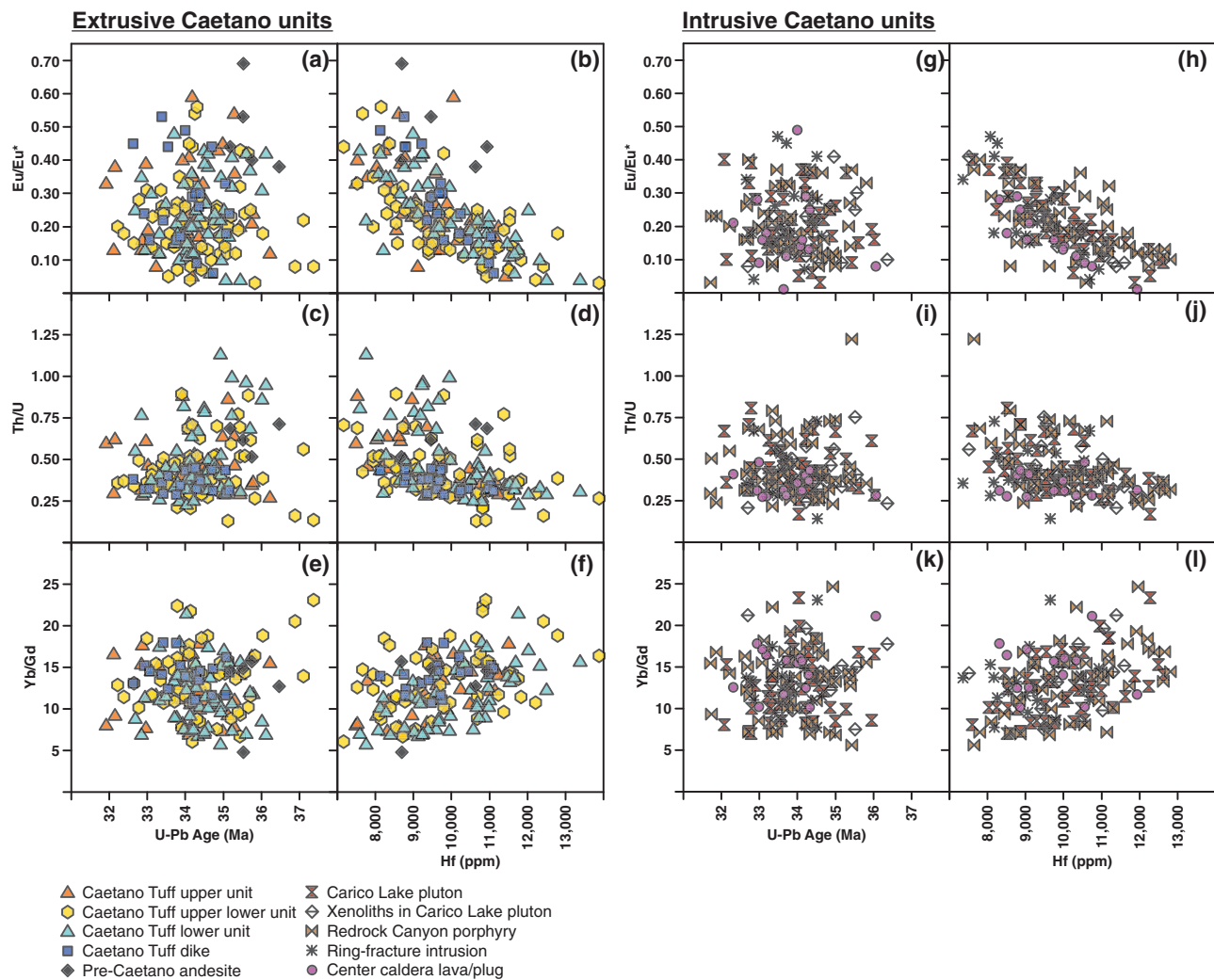
Fig. 19. Compilation of zircon trace element data, divided into extrusive (a–f) and intrusive (g–l) Caetano units. Selected trace element ratios are plotted against U–Pb age and Hf concentration.

discussion is focused on key points concerning the formation of the Caetano Tuff magma chamber, development of its compositional zonation, the conditions that led to its eruption, its relationship to large caldera intrusions, and its role in informing extant mush model paradigms. The section concludes with a bulleted petrogenetic model and figure that summarizes the sequential evolution of the Caetano caldera system.

Formation of the Caetano Tuff magma chamber

Vigorous Eocene magmatism, thought to be related to roll-back of the formerly shallow Farallon slab, initiated in the Caetano region by ~39 Ma, beginning with silicic intrusions associated with the 35·7–36·3 Ma Cortez and Cortez Hill dikes and succeeded by eruption of the pre-Caetano andesite at 35·2 Ma (Fig. 2). Zircon U–Pb age populations in the Cortez and Cortez Hill dikes (John *et al.*, 2009) and pre-Caetano andesite (Fig. 18i and j) overlap the oldest zircons in the Caetano Tuff (Fig. 18a–h), temporally linking early phases of magmatism to the main magma building phase that culminated in

eruption of the Caetano Tuff ignimbrite at 34·0 Ma. The peraluminous (ASI 1·0–1·2; Fig. 4b), high-$\delta^{18}O$ (10·0–10·5‰; Fig. 15a) and radiogenic ($^{87}Sr/^{86}Sr_i = 0·7068$–0·7072, $\varepsilon Nd = -4·93$ to $-4·94$; Fig. 17a and b) characteristics of the Caetano Tuff provide unequivocal evidence for its derivation from high-$\delta^{18}O$ metasedimentary basement crust (Figs 16 and 17). Ubiquitous Proterozoic and lesser Mesozoic and Tertiary zircon xenocrysts in the Caetano Tuff (Fig. 18a–h), Mesozoic zircon xenocrysts in the pre-Caetano andesite (Fig. 18i and j), and metapelite xenoliths dominated by Proterozoic zircon xenocrysts in the Carico Lake pluton (Fig. 18s and t) provide direct evidence of magmatic sampling of the basement crust at depth.

The refractory major element compositions of the metapelite xenoliths (Fig. 4), and a restitic mineralogy of Al- and Fe-rich phases, including low-pressure andalusite and cordierite (Fig. 13h), support their derivation from an Fe-rich pelitic source at low pressure (<4 kbar) and high temperature (>700°C) (Bucher & Grapes, 2011). These conditions overlap the pelitic wet solidus for biotite-dehydration melting via the following

reactions: biotite + plagioclase + aluminosilicate + quartz = melt + cordierite (Patiño Douce & Johnston, 1991), biotite + aluminosilicate + quartz = melt + cordierite + K-feldspar, and biotite + aluminosilicate = melt + cordierite + spinel + K-feldspar (White et al., 2003). These phases are consistent with the mineralogy observed in the xenoliths (Fig. 13h). Whole-rock major element data for the least evolved Caetano rhyolites overlap the partial melt fields for mafic metapelite and metagraywacke crustal sources (Fig. 5), and the xenoliths contain a small portion of zircons with U–Pb ages and trace element concentrations that overlap those of the Caetano magmas (Figs 18s, t and 19g–l). The combined evidence supports large-scale anatexis of metapelitic basement to generate the Caetano Tuff parental magma, with the xenoliths representing the restitic residues from which the rhyolite melts were extracted.

By the end of the Cretaceous, Mesozoic crustal shortening had thickened the crust beneath the Caetano region to ∼40–50 km (Coney & Harms, 1984; DeCelles & Coogan, 2006). Paleozoic–Proterozoic strata were folded and thrust faulted into imbricate sequences of carbonate and siliciclastic rocks up to 30 km thick (e.g. Howard, 2003; Lee et al., 2003) (Fig. 16). The Proterozoic McCoy Creek Group is a thick package (>2·7 km) of siliciclastic rocks widely exposed in the Deep Creek, Schell Creek, and Snake Ranges in eastern Nevada (Misch & Hazzard, 1962; Rodgers, 1984; Fig. 1). U–Pb age spectra for inherited zircons in the Caetano Tuff and xenoliths are very similar to U–Pb age spectra for the McCoy Creek Group and overlying Prospect Mountain Quartzite in the Deep Creek Range (Fig. 16 inset; Yonkee et al., 2014). Proterozoic McCoy Creek Group metasediments in and near the Ruby Mountains core complex ∼100 km NE of the Caetano caldera (Hudec, 1992; Colgan et al., 2010; Fig. 1) conformably underlie Cambrian rocks equivalent to Cambrian strata exposed near the Caetano caldera [e.g. Hamburg Dolomite at Cortez ∼3 km NE (Gilluly & Masursky, 1965) and at Gold Acres ∼7 km north (Leonardson, 2010) and the Prospect Mountain Quartzite at Eureka <100 km to the SE (Long et al., 2014) (Figs 1 and 2)]. It is therefore reasonable to infer the presence of these units at depth beneath Caetano.

Mica schists, phyllites, metasiltstones, argillites, and quartzites of the McCoy Creek Group (Misch & Hazzard, 1962) would have been fertile sources for silicic magma generation as mafic magmas intruded the crustal column during slab roll-back (Fig. 16). The uniformly radiogenic and ^{18}O-enriched character of all erupted Caetano magmas, contrasted with the extreme isotopic heterogeneity of the metapelite xenoliths (Fig. 17), supports a model in which basalts intruded and melted isotopically diverse and fertile mid–upper crust, followed by accretion of anatectic melts to form a large and isotopically well-mixed magma reservoir (Fig. 16). An early stage snapshot of this assembly process may be represented by the pre-Caetano andesite, which has a lower $\delta^{18}O$ value, more radiogenic isotope signature, and significant Mesozoic inheritance (Figs 17 and 18j), suggesting

derivation from an isotopically distinct parcel of Mesozoic crust.

Trace elements and REE patterns in the least evolved Caetano rhyolites are very similar to those for analyzed metapelites exposed in the Lamoille Canyon area of the Ruby Mountains and the East Humboldt Range (Lee et al., 2003; Figs 1, 10 and 11). Combined with O, Sr, and Nd isotopic constraints (Fig. 17), this supports large-degree partial melting of similar source rocks to generate the Caetano magmas, with little mass contributed from the basaltic intrusions to perturb the geochemical budget of the system. This is in contrast to other mid-Tertiary igneous centers in Nevada, which exhibit significant geochemical and isotopic diversity, pointing to large contributions from mafic end-members (e.g. Gans et al., 1989; Grunder, 1995; Barnes et al., 2001). Thermodynamic modeling of incremental intrusion of basaltic sills into fertile pelitic upper crust demonstrates that partial melt can reach ∼60% at typical arc magma production rates over a period of ∼1·6 Myr (Annen & Sparks, 2002; Annen et al., 2006). This time period is roughly equivalent to the time elapsed between the pre-Caetano andesite and the Caetano Tuff in U–Pb zircon crystallization age (∼1·4 Myr; Fig. 18a–j) and $^{40}Ar/^{39}Ar$ eruption age (∼1·2 Myr; Table 11). Intrusion of basaltic magmas over million year timescales (as inferred by the pre-caldera dikes and andesite) is also consistent with the requirement for thermal pre-conditioning of the crust to accommodate accumulation and storage of the >1000 km^3 Caetano Tuff magma chamber (Jellinek & DePaolo, 2003; Annen, 2009).

Because binary mixing between anatectic melts of pelitic crust and intruded basaltic magma (Fig. 17) would produce magmas of intermediate composition, it is inferred that the Caetano Tuff inherited its isotopic composition from hybridized melts that fractionated in the upper crust (e.g. Nash et al., 2006). Geochemical and isotopic data do not preclude larger crustal proportions (up to 100%) in the Caetano Tuff magma chamber (Figs 11 and 17). However, thermomechanical models indicate that it is unlikely that no mixing would occur between partial melts of old pelitic crust, partial melts of new basaltic crust, and residual melts of crystallizing basaltic intrusions (Annen & Sparks, 2002). Although the pre-Caetano andesite may represent an early stage snapshot of the assembly process that produced the Caetano Tuff magma chamber, it is not a suitable intermediate progenitor of the Caetano Tuff based on its relatively small eruptive volume (Fig. 2), variably higher and lower compatible trace element contents (Fig. 9), disparate isotopic composition (Fig. 17), predominantly Mesozoic zircon U–Pb inheritance (Table 10), and zircon trace element trends that are distinct from the main Caetano array (Fig. 19a and b).

Zonation of the Caetano Tuff magma chamber

Fractional crystallization was the dominant process in establishing chemical gradients within the Caetano Tuff

magma chamber. Decreasing compatible trace elements and increasing incompatible trace elements (Fig. 9), depletion in LREE, sharp negative Eu anomalies and enrichment in HREE (Fig. 11), modal mineralogies that shift towards higher sanidine + quartz/plagioclase ratios and lower mafic mineral abundances (Fig. 12i–l), and more evolved plagioclase (Fig. 12o–r), sanidine (Fig. 12u–x) and biotite (Fig. 14a and b) compositions in the lower parts of the intra-caldera tuff sequence are consistent with this model. Sparse pyroxenes define a reverse trend, with less evolved compositions in lower tuff exposures (Fig. 14c). Ductile deformation and partial disaggregation of pyroxene-bearing andesite lithic fragments in the lower unit (e.g. Fig. 13f), and the identical pyroxene chemistry between the lower unit (including those pyroxenes in lithic fragments) and the pre-Caetano andesite (Fig. 14c), make a compelling case that the pyroxene is xenocrystic, probably syn-eruptively mixed with the tuff. In contrast, the upper unit and ring-fracture intrusion contain only a few xenocrystic pyroxenes (Fig. 14c); the majority are compositionally and texturally consistent with a magmatic origin (Figs 13b and 14c). Zircons exhibit trace element trends indicative of fractional crystallization; however, these trends overlap for all stratigraphic levels and U–Pb ages of the intra-caldera Caetano Tuff (Fig. 19a–f), indicating mixed zircon populations that recorded multi-stage growth in a long-lived magmatic system, preceding and continuing up through the time of chamber-wide zonation.

The observed compositional gap within the intra-caldera Caetano Tuff (~3 wt % SiO_2; Fig. 6a) is consistent with fractional crystallization and crystal–liquid separation in the Caetano Tuff magma chamber. Evolved melts are commonly segregated from their parental source mushes once a critical crystallinity is reached, yielding compositional gaps between extracted liquids and cumulate residues (e.g. Brophy, 1991; Deering & Bachmann, 2010; Dufek & Bachmann, 2010). Both Rhyolite-MELTS modeling of major elements (Fig. 8) and EC-RAxFC modeling of trace elements (Fig. 10) demonstrate that the compositional range of the Caetano Tuff, including the compositional gap, can be generated by crystallization of either the least evolved Caetano rhyolite composition (Carico Lake pluton) or a hypothetical 'gap' rhyolite with a composition intermediate between the lower and upper tuff units. The crystallinity at which the appropriate bimodal SiO_2 compositions are achieved for the 'gap' rhyolite (30%) is lower than that for the Carico Lake pluton (50–60%) or the optimal melt 'extraction window' (50–70%) of Dufek & Bachmann (2010) (Fig. 8). Crystallization of the Carico Lake pluton melt would produce cumulates higher in Sr and Ba than what is observed in the intrusive or extrusive rock record; however, these modeled concentrations do overlap the estimated Ba and Sr range of the recharge magma [~20 000 ppm Ba in sanidine rims corresponds to ~2000–4000 ppm Ba in equilibrium rhyolite (Nash & Crecraft, 1985), yielding an approximate Ba + Sr range of ~3000–6000] (Fig. 10).

A model in which cumulates (dominated by feldspar) were segregated from interstitial liquids is supported by the gap observed in whole-rock major elements (Fig. 6a), Sr and Ba trace elements (Fig. 9b and d) and plagioclase An contents (Fig. 12m–r). Composite clusters of plagioclase and orthopyroxene in the upper tuff unit and ring-fracture intrusion (Fig. 13b; Supplementary Data Appendix B) are also consistent with the existence of cumulates in the Caetano Tuff magma chamber; however, these cumulates are more mafic and refractory than the sanidine-rich cumulates that dominate the least evolved Caetano rhyolites. They are interpreted to represent early crystallized rind material (i.e. the mostly crystalline area between the wall-rock and melt-rich magma body), entrained in the Caetano Tuff magma prior to or during eruption. This interpretation is supported by Rhyolite-MELTS modeling, which demonstrates that plagioclase and orthopyroxene were early crystallizing phases in the Caetano rhyolites, the occurrence of the least evolved plagioclase crystals intergrown with orthopyroxenes in the upper tuff unit (Fig. 12o), and petrographic observations of cluster boundaries defined by euhedral crystal faces in contact with groundmass glass (Fig. 13b). The less pronounced gap in whole-rock trace elements and REE controlled by accessory phases (Figs 9f, h and 11) and the broad spread in zircon trace element ratios (Fig. 19) may be due to the mobility of smaller zircon and other accessory phases relative to larger feldspar crystals that remain locked in crystal mush zones during liquid segregation events (e.g. Stelten et al., 2015).

After extraction of high-SiO_2 liquids at ≥30% crystallinity (Figs 8 and 10), the trace element and REE patterns of the lower Caetano Tuff unit indicate continued crystallization along a genetically related liquid line of descent (Figs 9–11). However, this zoning is not systematic within the erupted stratigraphic sequence of the lower Caetano Tuff unit (e.g. Fig. 9 insets). The most evolved compositions in the tuff dike (Figs 9 and 11) would require >80% fractionation of the 'gap' rhyolite composition (Fig. 10). If loss of heat is the driving force for crystallization, it is likely that there were many melt segregation events, punctuated by subsolidus lock-up and rejuvenation–dissolution, to generate the compositionally zoned upper chamber (e.g. Hildreth & Wilson, 2007). It is interpreted that the more evolved upper chamber was largely isolated from its source mush after extraction, and geochemically discrete domains generated by its continued crystallization were mixed prior to eruption, homogenizing the magma (melt and minerals) to generate a compositionally and texturally 'monotonous' crystal-rich cap (see section below on evaluating the mush model for Caetano magmatism).

It is not likely that the compositional gap observed in the lower compound cooling unit was caused by a change in eruption dynamics (e.g. Spera et al., 1986). Caldera collapse, as evidenced by the presence of megabreccia blocks and mesobreccia lenses in the intra-caldera tuff, was occurring prior to and continuing

through the time at which the compositional gap was recorded in the eruptive sequence, and there is no physical evidence (e.g. welding break, megascopic change in tuff appearance) that correlates with the compositional gap in continuous outcrop. Megabreccia occurs about ~1200 m above the caldera floor and ~1400 m below the compositional gap in the northeastern part of the caldera [Fig. 2; compare fig. 15 of John *et al.* (2008)]. In the northwestern part of the caldera, megabreccia occurs within ~100 m of the caldera floor at Wilson Pass [Fig. 2; compare fig. 14 of John *et al.* (2008)]. A sufficiently deep basin would be needed to accommodate ~1200 m of intra-caldera tuff in the northeastern caldera, and paleovalley deposits in the area that pre-date the caldera have thicknesses less than half of what would be required (≤400 m thick paleovalley deposits in the southern Cortez Mountains; John *et al.*, 2008). This evidence indicates that caldera-wide collapse was probably occurring early in the eruptive sequence, with no apparent effect on the geochemical characteristics of the Caetano Tuff.

Eruption of the Caetano Tuff magma chamber

The Caetano Tuff probably erupted through multiple caldera ring dikes, one of which is preserved along the northeastern caldera margin (Fig. 2). The tuff dike is the most chemically evolved caldera unit (Figs 4, 9 and 11), and is a composite of coarsely porphyritic to nearly aphyric rhyolite. Aphyric sections of the dike may represent a small lens of crystal-poor melt that existed at the top of the chamber just prior to eruption; sparse aphyric pumices in basal Caetano Tuff vitrophyres lend support to this interpretation. Continuous eruption of the Caetano Tuff magma chamber preserved a zoned intra-caldera tuff sequence up to ~3·6 km thick, at which point a caldera-wide cooling or depositional break marks a clear hiatus in eruptive activity. The paucity of discernible eruptive breaks in the lower unit is consistent with other comparably voluminous ignimbrites erupted in intervals of days to weeks (e.g. Bishop Tuff, Wilson & Hildreth, 1997). Subsequent explosive ash eruptions continued in a more sporadic fashion, forming an additional 0·5–2 km of crystal-rich intra-caldera tuff and interbedded sediments. These upper unit tuffs are compositionally equivalent to the least evolved upper parts of the lower compound tuff unit (Figs 6, 9 and 11) and are interpreted to represent continued tapping of deeper, less evolved parts of the Caetano Tuff magma chamber. Geochemical and isotopic evidence from minerals (Figs 12o, p, u, v, 14 and 15a), U–Pb zircon geochronology (Fig. 18a–d), and identical $^{40}Ar/^{39}Ar$ sanidine ages (Table 11) support this interpretation.

Most of the Caetano Tuff appears to have been retained within the topographic confines of the caldera. Modeled ash-fall dispersal models for supervolcanoes predict continental-scale ash deposition (e.g. Mastin *et al.*, 2014), yet no ash deposits of Caetano age or

composition have been identified in basins of the western USA that contain Paleogene deposits (e.g. southern Great Valley and Santa Ynez–Red Mountain area in California, northeastern Oregon, western Idaho; A. Sarna-Wojcicki, personal communication). Post-eruption erosion of ash cannot be discounted; the Caetano Tuff erupted near the crest of an erosional highland (Nevadaplano) in the mid-Tertiary (e.g. Henry *et al.*, 2012; Cassel *et al.*, 2014; Fig. 1). However, it is notable that the outflow Caetano Tuff is much less widely distributed and presumably of smaller volume than many other ignimbrites of Eocene–Oligocene age in the Nevada Great Basin (e.g. Henry *et al.*, 2012; Figs 1 and 2). The lack of a fall deposit in the vicinity of the Caetano caldera is analogous to observations for other comparably voluminous ignimbrites erupted in the Great Basin (e.g. Maughan *et al.*, 2002) and flare-up provinces elsewhere (e.g. Bryan *et al.*, 2010; Folkes *et al.*, 2011; Lipman *et al.*, 2015), indicating that this may be due to high mass eruption rates and rapid development of collapsing pyroclastic flows in the largest caldera-forming eruptions (see de Silva *et al.*, 2006), perhaps related to specific eruption-triggering mechanisms such as rapid roof failure (Gregg *et al.*, 2012).

Eruption triggering of the Caetano Tuff appears to have been facilitated at least in part (see later section on evaluating the mush model for Caetano magmatism) by chamber-wide magmatic recharge events, as evidenced by CL-bright overgrowth rims on sanidine and quartz phenocrysts (Fig. 12u–x insets; Fig. 13d). Zoned sanidines are particularly abundant in the upper unit and upper lower unit, with Ba rim concentrations up to ~20 000–25 000 ppm (Fig. 12u and v). Liquidus temperatures, zircon saturation temperatures and Ti-in-zircon temperatures are also higher for these units (Supplementary Data Fig. 1; Supplementary Data Table 11), supporting their derivation from deeper levels within the Caetano Tuff magma chamber. Petrographic examination of single sanidine phenocrysts with CL reveals that they are generally present as large crystal fragments rather than intact grains (Fig. 12u–x insets), and extrapolation of fragment dimensions corresponds to whole crystals several millimeters to ~0·5 cm in size. This evidence combined with their poikilitic textures (Supplementary Data Appendix B) indicates rapid growth of sanidine phenocrysts as they recorded chemical perturbations to their host melts. Most crystals possess multiple Ba spikes, indicating that magma recharge occurred repeatedly prior to eruption.

The recharge magma that affected the Caetano Tuff magma chamber is inferred to have had similar geochemical characteristics to the main magma body, based on the rhyolitic composition of the entire intra-caldera tuff sequence (Fig. 6a), the lack of mafic enclaves and predominantly rhyolitic pumice compositions (Fig. 4a), and the isotopic homogeneity of all Caetano rhyolites, including those with a greater proportion of sanidines with high Ba (Figs 12s–x and 15a). A rhyolite melt with ~2000–4000 ppm Ba would be

required for equilibrium crystallization of the high-Ba sanidine rims (~20 000 ppm Ba) (Nash & Crecraft, 1985), which is within the upper range of Ba contents documented in the least evolved Caetano rhyolites and the post-Caetano andesite (Fig 9c and d). The boundaries between CL-dark and CL-bright zones in sanidine and quartz phenocrysts are commonly defined by resorption textures, indicating dissolution prior to bright-rim overgrowths. This evidence is consistent with high-temperature silicic magmas remelting cumulates and leading to increased Ba contents in the melt and high-Ba sanidine rim growth (e.g. Bachmann *et al.*, 2002, 2014; Wolff *et al.*, 2015). These cumulates may have been derived from either crystallization of the hypothetical 'gap' melt or Carico Lake pluton melt (Fig. 10).

Modeling of timescales required to generate the sharp sanidine Ba diffusion profiles for a range of magmatic temperatures (800–850°C), the upper end of which approximates the liquidus temperatures of the least evolved Caetano rhyolites (Fig. 6c), yields estimates of hundreds to thousands of years (Supplementary Data Appendix C). These calculations assume an initial step function in Ba concentration, which may not be valid owing to growth zoning or disequilibrium crystallization that results in a more relaxed initial profile shape (e.g. Chamberlain *et al.*, 2014; Till *et al.*, 2015). Therefore these calculations are maximum estimates. Notwithstanding, it appears that recharge and subsequent eruption of the Caetano Tuff (at which point Ba diffusion in sanidine crystals ceased) occurred on geologically rapid (hundreds to thousands of years or less) timescales, a conclusion that has been corroborated by many other mineral chronometry studies of ignimbrite eruptions (e.g. Morgan *et al.*, 2006; Wark *et al.*, 2007; Druitt *et al.*, 2012; Matthews *et al.*, 2012; Chamberlain *et al.*, 2014).

Relationship between the Caetano Tuff and caldera intrusions

The identical ^{40}Ar/^{39}Ar ages of the Caetano Tuff, Carico Lake pluton and Redrock Canyon porphyry (Table 11), and their compositional affinity in whole-rock major, trace and REE contents (Figs 4, 6, 9 and 11), modal mineralogy (Fig. 12g–j), plagioclase chemistry (Fig. 12m–p), sanidine Ba zoning (Fig. 12s–v), mineral-scale O isotope compositions (Fig. 15) and whole-rock Sr, Nd and Pb isotope compositions (Fig. 17; Table 9), provide robust evidence for a cogenetic origin. Modeling results for major and trace element compositions are consistent with the pluton, porphyry and least evolved upper tuff unit consisting largely of residual cumulate material from which more evolved rhyolitic liquids were extracted (Figs 8 and 10). The pluton and porphyry were not formed from newly amalgamated magma batches beneath the caldera that were independent of the Caetano Tuff magma chamber (see Glazner *et al.*, 2004, 2008; Tappa *et al.*, 2011; Zimmerer & McIntosh, 2012; Mills & Coleman, 2013). Phenocryst resorption textures

(Supplementary Data Appendix B), fractional crystallization signatures (Figs 9 and 10), and sanidine Ba zoning (Fig. 12s and t) provide clear evidence that intrusive crystal cargoes interacted with liquid-rich magmas and were not derived from slow accumulation of near-solid material (e.g. Coleman *et al.*, 2004; Frazer *et al.*, 2014). Slightly less evolved average whole-rock compositions (Fig. 6a and b), liquidus temperatures (Fig. 6c), and biotite chemistry (Fig. 14a and b) relative to other low-SiO$_2$ caldera units indicate that the Carico Lake pluton tapped less evolved (and deeper) parts of a common magmatic system. The presence of metapelite xenoliths within the Carico Lake pluton (and their absence in other caldera units) also supports a deeper crustal origin, perhaps along the base of the chamber where Proterozoic basement crust (restite) was mechanically removed and entrained in the Carico Lake pluton magma body.

Error-weighted mean zircon U–Pb ages for the Carico Lake pluton and Redrock Canyon porphyry are 0·2–0·5 Myr younger than those determined for different stratigraphic sections of the intra-caldera Caetano Tuff (Fig. 18a–h, k–n), possibly owing to dissolution of zircon crystals from earlier stages of magma assembly. Zircon xenocrysts in the small caldera intrusions (Fig. 18o–r), suggest that their absence in the pluton and porphyry may be related to the size and thermal regime (prolonged residence at high temperature) of larger magmatic bodies that do not favor preservation of inherited zircon crystals and retain a zircon crystallization record skewed towards later stages of magma growth (e.g. Lipman & Bachmann, 2015). The preservation of fresh mafic phenocrysts (biotite, hornblende) in the upper Caetano Tuff and ring-fracture intrusion (e.g. Fig. 14d inset), compared with their pervasive resorption in the Carico Lake pluton and porphyry (Fig. 13e), supports this hypothesis. Evidence for magma recharge in the tuff, pluton and porphyry (Fig. 12s–x) indicates that reheating preceded eruption, which may have maintained an elevated thermal gradient in the residual (non-erupted) sub-caldera magma reservoir that favored dissolution (e.g. Miller *et al.*, 2007). However, we note that the broad spread in zircon trace elements in the Carico Lake pluton generally matches what is observed in the Caetano Tuff (Fig. 19) and does not indicate any missing (earlier) phases of crystallization.

The magmatic build-up to the climactic caldera-forming eruption of the Caetano Tuff did not occur on geologically instantaneous timescales (see Glazner *et al.*, 2004), but probably over a protracted period of hundreds of thousands of years, based on 0·2–0·5 Myr older mean zircon U–Pb ages (Fig. 18a–h; Table 10) relative to sanidine ^{40}Ar/^{39}Ar eruption ages (Table 11). Zircon populations in the Caetano Tuff and large caldera intrusions appear to be predominantly autocrystic (crystallized *in situ* in Caetano magmas) as opposed to antecrystic (derived from magmatic precursors) or xenocrystic (derived from foreign contaminants) based on their (1) generally continuous U–Pb age spectra and unimodal probability density functions (Fig. 18a–h, k–r),

(2) consistency in trace element concentrations and ratios that fall along fractional crystallization trends (e.g. Fig. 19b and h), and (3) restricted ranges of doubly fingerprinted (δ^{18}O composition and U–Pb age) cores and rims (Fig. 15b). The Carico Lake pluton and Redrock Canyon porphyry do not posses any zircon evidence for crystallization and growth that significantly post-dated the caldera-forming eruption (Fig. 18k–n). Their buoyant intrusion and subsequent cooling and consolidation occurred shortly after eruption, based on indistinguishable sanidine ^{40}Ar/^{39}Ar ages between the caldera-forming ignimbrite and resurgent caldera intrusions (Table 11).

The restored (pre-extension) volume of the exposed parts of the Carico Lake and Redrock Canyon intrusions is >50 km^3, and the total pluton volumes at depth are probably much greater. Aeromagnetic data reveal magnetic highs that span the entire caldera basin, with the Carico Lake pluton corresponding to a distinct magnetic high in the center of the caldera (Fig. 3). Using three-dimensional reconstructions of erupted and intruded deposits, maximum caldera down-drop, and hornblende barometry constraints, we estimate an ~5–9 km thick magma chamber, with the top at ~3 km depth and the base at ~8–12 km depth. Using a pre-extension caldera area of 280 km^2, and attributing ~4 km thickness and 1100 km^3 in volume to the Caetano Tuff, a minimum pluton volume of ~280–1400 km^3 is derived. This corresponds to a combined magmatic volume of >2500 km^3 for the Caetano caldera, and an intrusive:extrusive (I:E) ratio of ~1:1 to 1:4. This ratio is lower than I:E estimates for calderas that have produced tuffs of comparable volume to the Caetano Tuff (e.g. Yellowstone 3:1 and Long Valley 10:1; White *et al.*, 2006), and considerably lower than the extreme I:E ratios for total replacement of the upper crustal column by plutons extending down to >15–20 km depth (e.g. Lipman, 2007; Grunder *et al.*, 2008).

Evaluating the mush model for Caetano magmatism
Given the highly crystal-rich nature of the intra-caldera Caetano Tuff (Fig. 6d), textural evidence from crystal clusters and resorbed minerals (Fig. 13b; Supplementary Data Appendix B), lengthy zircon crystallization timescales (Fig. 18a–h), and populations of zircons with low Ti-in-zircon crystallization temperatures (Supplementary Data Figs 1 and 2), near-solidus (mush) conditions are unequivocal in its magmatic evolution. However, several aspects of the Caetano Tuff are inconsistent with prevailing mush paradigms. A dichotomy has been proposed to explain ignimbrite zoning patterns, in which crystal-rich mushes (manifest by monotonous intermediates) require thermal reactivation timescales that exceed homogenization timescales, whereas crystal-poor caps of mushes (crystal-poor rhyolites) exist in an imminently eruptible state, requiring minimum reactivation timescales that permit

preservation of magma chamber gradients (Huber *et al.*, 2012). Although the Caetano Tuff is monotonous in some respects (crystallinity, O, Sr, Nd, Pb isotopic composition), it retains clear evidence of chemical zonation in whole-rock major, trace and REE, liquidus temperatures, modal mineralogy, and mineral chemistry (Figs 6, 9, 11, 12i–l, o–r, u–x and 14a–c). Its volume and zoned rhyolite chemistry are more reminiscent of the Bishop Tuff (e.g. Hildreth & Wilson, 2007), whereas its uniformly crystal-rich nature and protracted duration of crystallization are more comparable with the Fish Canyon Tuff (e.g. Bachmann *et al.*, 2002; Wotzlaw *et al.*, 2013). We posit that it represents an intermediate process between these two archetypal end-members, involving both (1) segregation of evolved melt lenses through fractional crystallization from deeper or less evolved source mushes to generate a zoned chamber and (2) remobilization of batholith-scale, largely crystalline mush zones from the top through to the lowermost portions of the chamber. This remobilization process did not, however, result in homogenization of chemical gradients, despite clear evidence for multiple episodes of recharge prior to eruption (Fig. 12s–x).

The more silicic nature of the Caetano Tuff compared with similarly crystal-rich monotonous intermediates is a feature that is shared with many other rhyolitic ignimbrites around the world, including numerous examples in the western and central Nevada volcanic fields (Fig. 7; Best *et al.*, 2013c). It is perhaps instructive that several of these crystal-rich rhyolitic ignimbrites were erupted in immediate proximity to the Caetano caldera in central Nevada (e.g. Fish Creek Mountains Tuff, tuff of Cove Mine; Figs 1 and 7), highlighting the importance of their source protoliths and the crustal architecture in this region (Fig. 16). Partial melting of pelitic crust generates large volumes of initial rhyolite (Patiño Douce & Johnston, 1991; Annen & Sparks, 2002), without the requirement for multi-stage distillation from more mafic precursors (Dufek & Bachmann, 2010). Anatexis of large volumes of metasedimentary crust, and isotopic modification of mafic magmas during their ascent through the crustal column, is consistent with the uniformly radiogenic and ^{18}O-enriched character of all erupted Caetano magmas (Fig. 17). This process may be analogous to those that have yielded exceptionally large volumes of crystal-rich ignimbrites in the Altiplano region of the central Andes (e.g. de Silva, 1989), as they share many distinct similarities, including eruption through tectonically thickened crust, preponderance of silicic relative to mafic erupted products, and petrological requirements for derivation from large-scale crustal melting rather than fractional crystallization of mantle-derived magmas. Ignimbrite deposits of the central Andes are also comparably elevated in their δ^{18}O compositions (δ^{18}O$_{quartz}$ = 8·1–9·6‰, δ^{18}O$_{zircon}$ = 6·7–7·8‰; Folkes *et al.*, 2013).

In addition to tectonic setting, chamber geometry is another factor that may explain some of the hybrid qualities of the Caetano Tuff. Slab- or sill-like chamber

geometries (width/height aspect ratio > 2) promote homogeneous mixing as crystal-laden plumes descend from the roof, and buoyant melts rise from crystal frameworks along the chamber floor, resulting in stirring and blending of chemical and thermal gradients (de Silva, 1991). In contrast, more equant chamber geometries (aspect ratio < 2) promote sidewall crystallization and convective fractionation, ferrying buoyant melts to the top of the chamber, resulting in chemical and thermal stratification (e.g. Baker & McBirney, 1985). A restored (pre-extension) caldera diameter of 20 km, and a chamber thickness of ~5–9 km would correspond to an intermediate aspect ratio of ~2–4 for the Caetano Tuff magma chamber. Chemical evidence for crystal fractionation would seem consistent with a more equant chamber geometry. However, whereas the bulk of the intra-caldera tuff sequence (>2·5 km from the caldera floor) is homogeneous ('monotonous') and well mixed with respect to major elements (Fig. 6a and b), crystallinity (Fig. 6d), modal mineralogy (Fig. 12k and l), and mineral chemistry (Figs 12q, r, w, x and 14a, b), the overlying >1·5 km of tuff is less evolved and more heterogeneous (Fig. 6a and b). A major element compositional gap separates the two groups within a single compound cooling unit of tuff (Fig. 6a–c), providing evidence for a discrete thermochemical boundary layer within the tuff's source magma chamber at the time of eruption. Major and trace element modeling indicates that this boundary layer formed as a result of fractional crystallization and crystal–melt segregation. Following segregation, the two compositional groups may have been partly separated by this boundary layer. One possibility is a thermally buffered crystal partition (e.g. Ellis *et al.*, 2014). Although there is only a slight increase in crystallinity at this level within the intra-caldera Caetano Tuff (Fig. 6d), this boundary may have been more pronounced during much of its pre-eruptive magmatic evolution. If such a partition existed, the effective aspect ratio of the upper part of the chamber would have been fairly high (~8), aiding in convective overturn and homogenization, whereas the lower chamber (upper tuff exposures) may have maintained more compositional diversity and a direct link to new magmatic inputs from below. Trace elements (including REE) demonstrate more variability than major elements, and less abrupt zonation across the thermochemical boundary layer (Figs 9 and 11), and thus the link between these two domains was not uniformly static, perhaps aided by the mobility of accessory minerals in interstitial melt zones (e.g. Stelten *et al.*, 2015). The upper chamber was also affected by recharge, although to a lesser extent than lower parts of the chamber (Fig. 12u–x).

Sanidine Ba zoning indicates that recharge of the Caetano Tuff magma chamber occurred within hundreds to thousands of years of eruption or less (Supplementary Data Appendix C), considerably shorter than the upper bounds of mush reactivation modeled for comparably thick (~2–5 km) crystal-rich ignimbrites (hundreds of thousands of years, Huber *et al.*, 2012;

Wotzlaw *et al.*, 2013). If stirring and homogenization occur on timescales 1–2 orders of magnitude shorter than those required for mush reactivation (Huber *et al.*, 2012), eruption of crystal-rich Caetano Tuff with chemical gradients intact is an obvious contradiction to this model. However, our data indicate that recharge alone may not have been sufficient to trigger eruption, based on evidence for multiple episodes of recharge within sanidine phenocrysts, the paucity of Ba-enriched growth bands in sanidines from the lower tuff unit relative to the upper tuff unit, and consistently sharp diffusion profiles across all sanidine domains that formed within a narrow time window of eruption (Fig. 12u–x).

Additional processes that may aid in remobilization of batholith-sized magma chambers include tectonic extension (Allan *et al.*, 2012), external roof triggering (Gregg *et al.*, 2012), and buoyancy (Burgisser & Bergantz, 2011; Caricchi *et al.*, 2013; Malfait *et al.*, 2014; but see Gregg *et al.*, 2015). Structural data indicate minimal tectonic extension at the time of the Caetano Tuff eruption (Colgan *et al.*, 2008). Ash-flow tuffs and sediments in the caldera are conformable over 9 Myr, from 34 to 25 Ma, and consistent with little to no extension prior to Miocene times, when ~110% extension dissected the caldera basin (Colgan *et al.*, 2008; Fig. 2). The exclusively vertical to steeply inward dipping faults along the caldera margins to depths >4 km (Henry & John, 2013) are not consistent with external roof triggering, which would be expected to produce outward dipping reverse faults (Gregg *et al.*, 2012). The roof aspect ratio for the Caetano Tuff magma chamber (~0·3 based on a 3 km depth to the top of the chamber and a 10 km horizontal half-width) and its volume (>1100 km³) fall within a range in which both fault generation in the roof and dike injection from the reservoir below are likely to be important in triggering eruption (i.e. volume > 1000 km³ and roof aspect ratio < 0·5; Gregg *et al.*, 2012). Buoyancy as a long-term process, starting during the nascent stages of magma generation and continuing through batholith-scale development of the Caetano Tuff chamber, punctuated by a succession of relatively late-stage recharge events as a final eruption trigger, is our preferred interpretation. Recharge may have worked in concert with buoyancy, leading to the formation of buoyant (hot and more crystal-poor) melt lenses that aided in remobilizing or 'unzipping' the crystal-rich Caetano mush (e.g. Burgisser & Bergantz, 2011).

Petrogenetic model

The combined geological, petrological, and geochronological results presented here constrain the sequential evolution of the magma chamber that sourced the Caetano Tuff and its intrusive equivalents (Fig. 20).

(a) Silicic dikes and domes at Cortez and Cortez Hills were emplaced at 35·7–36·3 Ma, along what would become the northeastern margin of the Caetano caldera. Within 0·5 Myr of this magmatic episode,
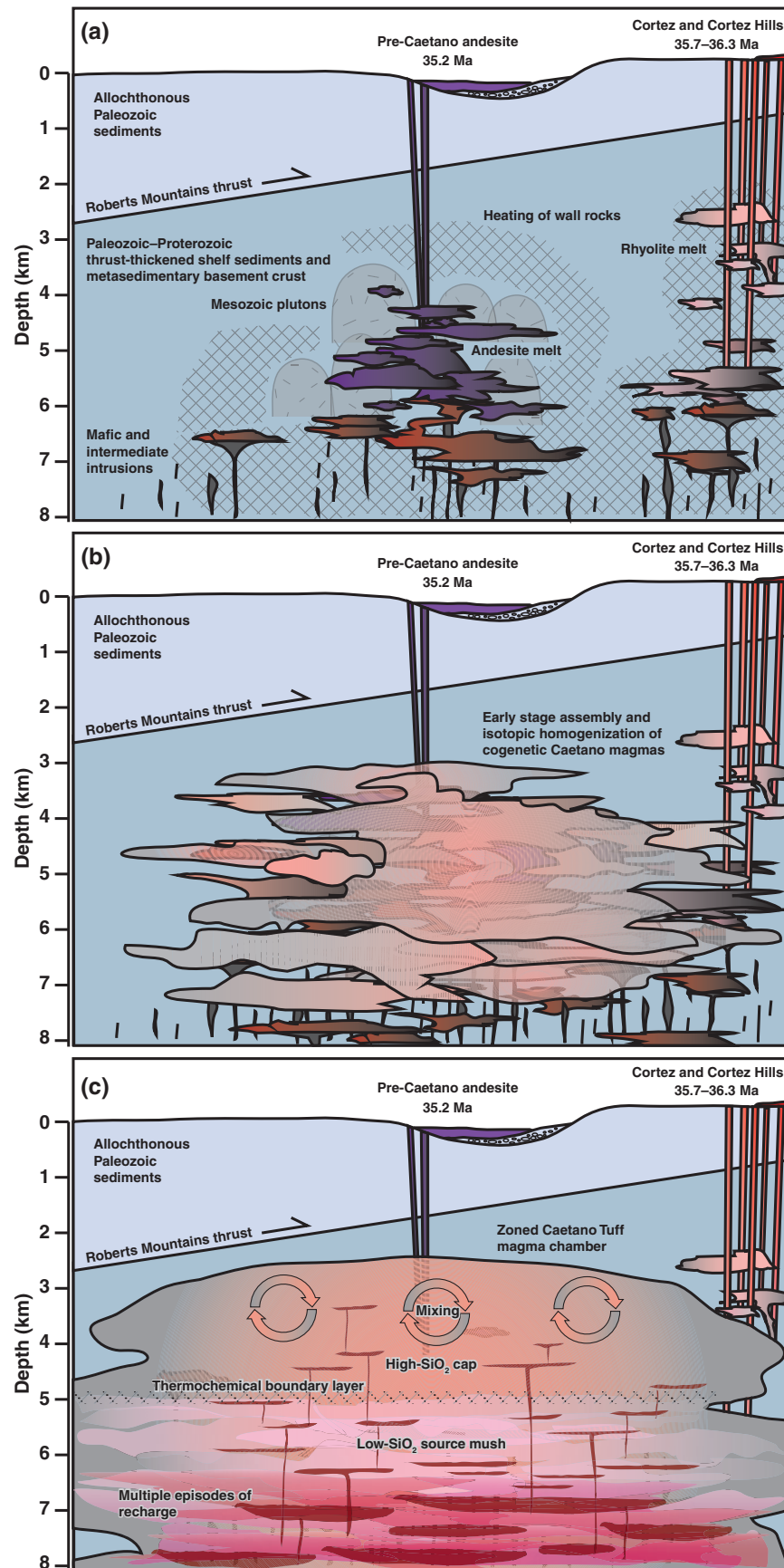
Fig. 20. Schematic evolution of the Caetano caldera system, from the earliest to the latest phases of magmatic activity (a–f). Vertical exaggeration ~2:1. Descriptions of each panel are included in the main text.
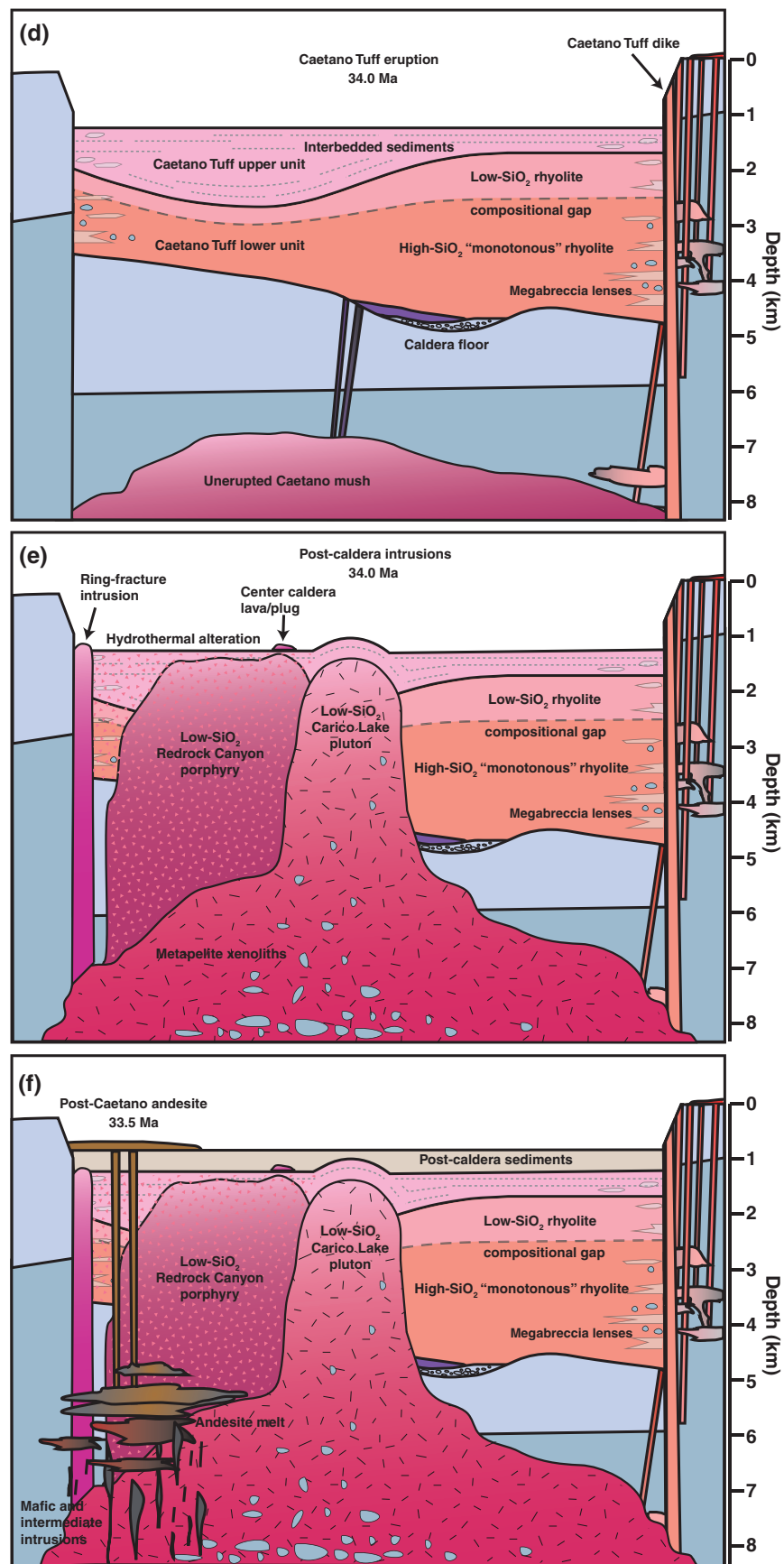
Fig. 20. (Continued)

andesite erupted at 35·2 Ma, producing lavas that partly covered Paleozoic basement rocks and Eocene gravels along the eastern part of the caldera floor. Isotopic data for the pre-caldera andesite confirm a strong crustal affinity, and support a model of mixing and hybridization of mantle-derived melts with basement crust (predominantly Mesozoic based on zircon U–Pb inheritance). Mafic intrusions and precursory magmas preheated the surrounding wall rocks, priming the crustal block for large-volume melt accumulation.

(b) Early stage melt accumulation of the Caetano Tuff magma chamber overlapped in space and time with the pre-caldera silicic dikes and andesite, as evidenced by overlapping zircon U–Pb age spectra. Like the pre-caldera andesite, isotopic data are consistent with a large proportion of crust ($\sim$70–80%) in the source magma of the Caetano Tuff, dominated by Proterozoic metasedimentary basement, with lesser Mesozoic and Tertiary components. As heterogeneous melts rose through the crustal column they were amalgamated and homogenized at shallower crustal levels. Isotopic homogenization was achieved early in the evolution of the magma body, based on doubly fingerprinted O isotope compositions and U–Pb ages of single Caetano zircons. A large and overlapping spread in zircon trace element ratios (through time and with increasing degrees of differentiation) indicates prolonged assembly of cogenetic Caetano magmas. Peak zircon crystallization occurred between 34·2 and 34·5 Ma (0·2–0·5 Myr prior to 34·0 Ma Caetano Tuff eruption), supporting a protracted period of magma assembly.

(c) Extensive crystal fractionation occurred within the source magma chamber of the Caetano Tuff and was the dominant cause of its zonation. The intra-caldera tuff is normally zoned upwards from high- to low-SiO$_2$ compositions, which correlate with whole-rock trace element and REE contents, liquidus temperatures, mineral modal abundances and mineral chemistry. A distinct compositional gap occurs within a single compound cooling unit of the tuff, providing evidence for a thermochemical boundary layer within the Caetano Tuff magma chamber at the time of eruption. Geochemical evidence indicates that this gap resulted from extraction of more evolved interstitial melts from less evolved crystal mush progenitors. Following extraction and chemical stratification, the melt-rich zone continued to crystallize, differentiate, and mix, forming a homogeneous cap overlying a less evolved and more heterogeneous source mush. Multiple episodes of recharge and oscillating supra-solidus to sub-solidus conditions punctuated the evolution of the magmatic system. However, these reheating events did not result in complete overturn or convective homogenization of the Caetano Tuff magma chamber.

(d) Eruption of the large-volume ($>$1100 km^3) Caetano Tuff at 34·0 Ma evacuated the zoned magma chamber from the top down. A tuff dike along the northeastern caldera margin tapped the most chemically evolved (and also partly aphyric) part of the system. The bulk of the intra-caldera tuff was erupted as high-SiO$_2$ (75–78 wt % SiO$_2$), crystal-rich (30–45 vol. %) 'monotonous' rhyolite capped by a smaller volume of low-SiO$_2$ (71–75 wt % SiO$_2$) and comparably crystal-rich, but more heterogeneous, rhyolitic tuff. This sequence comprises an $\sim$3·6 km compound cooling unit (defined as the lower unit) along the northeastern caldera margin that thins westward following asymmetric caldera collapse. An additional 0·5–2 km thickness of low-SiO$_2$, crystal-rich tuffs and interbedded sediments (defined as the upper unit) overlies the compound cooling unit, and represents sporadic tapping of deeper and less evolved parts of the Caetano Tuff magma chamber.

(e) Two voluminous low-SiO$_2$ caldera intrusions (Redrock Canyon porphyry and Carico Lake pluton) and several smaller intrusions were emplaced shortly after the climactic caldera-forming eruption at 34·0 Ma, within analytical uncertainty of ^{40}Ar/^{39}Ar sanidine ages ($\pm$0·05 Ma). All geochronological, petrological, and isotopic datasets indicate that the intrusive caldera units were derived from large volumes of crystal-rich magma that remained in the Caetano Tuff chamber after caldera collapse. Geologic mapping, aeromagnetic data, and geobarometry constraints indicate that the plutonic volume was comparable to or possibly exceeded that of the Caetano Tuff. Emplacement of the Redrock Canyon porphyry drove a large hydrothermal system in the western half of the caldera, which terminated prior to or during intrusion of the unaltered Carico Lake pluton. The Carico Lake pluton was forcibly emplaced at shallow crustal levels ($<$1 km depth), locally doming and steeply tilting the intra-caldera Caetano Tuff. Metapelite xenoliths within the Carico Lake pluton signify deeper crustal origins prior to its buoyant ascent.

(f) Post-caldera andesites erupted in the northwestern part of the caldera at 33·5 Ma. Similar whole-rock trace element contents and Sr, Nd, and Pb isotope ratios support a genetic affinity between the post-caldera andesite and the caldera-forming tuff and intrusions. The post-caldera andesite may have been sourced from the remobilized sub-caldera roots of the Caetano system, with lower O isotope ratios that reflect a larger mantle component during rejuvenation. Its high Sr + Ba content is consistent with tapping of a cumulate (feldspar)-rich source. The 0·5 Myr younger age of the post-caldera andesite relative to the caldera-forming eruption and plutonic rocks that had cooled through their closure temperatures indicates that its source rocks would have been fully solidified prior to remelting and remobilization.

CONCLUSIONS

An exceptional record of magmatism is preserved in the 34 Ma Caetano caldera, providing an unusual opportunity to probe the processes and timescales over which the Earth's largest calderas are built. Many of the classic features of calderas are directly observable at Caetano, allowing reconstructions of magmatic processes that culminate in explosive eruptions, and providing a critical window into the linkages between volcanic and plutonic parts of large caldera systems that are commonly lacking in younger and less well-exposed calderas around the world. Actively deforming caldera volcanoes, such as Yellowstone and those in the Altiplano–Puna Volcanic Complex, underscore the need for geological context in which to make constrained predictions. Our study provides multiple lines of corroborating evidence (whole-rock, major and accessory mineral, isotopic, geochronologic) that voluminous ignimbrites can have substantial plutonic counterparts, formed by the same physical processes that yield climactic caldera-forming eruptions. This study demonstrates that long periods of precursory magmatic build-up are terminated by rapid remobilization and eruption of crystal-rich ignimbrites, and comparably rapid intrusion of sub-caldera plutons. The Caetano Tuff does not fit within a simple two-state mush model paradigm, and requires reconsideration of mush reactivation and homogenization timescales. Future studies will undoubtedly reveal a more complete story from the framework established by the present investigation, and one that we hope will further the longstanding goal of an integrated perspective into the dynamic processes of crustal magmatism and the occurrence of geologically rare, yet extreme events of explosive eruptions from supervolcanoes.

SUPPLEMENTARY DATA

Supplementary data for this paper are available at *Journal of Petrology* online.

REFERENCES

Allan, A. S. R., Wilson, C. J. N., Millet, M. A. & Wysoczanski, R. J. (2012). The invisible hand: tectonic triggering and modulation of a rhyolitic supereruption. *Geology* **40**, 563–566.

Annen, C. (2009). From plutons to magma chambers: thermal constraints on the accumulation of eruptible silicic magma in the upper crust. *Earth and Planetary Science Letters* **284**, 409–416.

Annen, C. & Sparks, R. S. J. (2002). Effects of repetitive emplacement of basaltic intrusions on thermal evolution and melt generation in the crust. *Earth and Planetary Science Letters* **203**, 937–955.

Annen, C., Blundy, J. D. & Sparks, R. S. J. (2006). The genesis of intermediate and silicic magmas in deep crustal hot zones. *Journal of Petrology* **47**, 505–539.

Bachmann, O. & Bergantz, G. W. (2004). On the origin of crystal-poor rhyolites: extracted from batholitic crystal mushes. *Journal of Petrology* **45**, 1565–1582.

Bachmann, O. & Bergantz, G. W. (2008a). Deciphering magma chamber dynamics from styles of compositional zoning in large silicic ash flow sheets. In: Putirka, K. D. & Tepley, F. J. (eds) *Minerals, Inclusions and Volcanic Processes. Mineralogical Society of America and Geochemical Society, Reviews in Mineralogy and Geochemistry* **69**, 651–674.

Bachmann, O. & Bergantz, G. W. (2008b). Rhyolites and their source mushes across tectonic settings. *Journal of Petrology* **49**, 2277–2285.

Bachmann, O., Dungan, M. A. & Lipman, P. W. (2002). The Fish Canyon magma body, San Juan volcanic field, Colorado: Rejuvenation and eruption of an upper crustal batholith. *Journal of Petrology* **43**, 1469–1503.

Bachmann, O., Miller, C. F. & de Silva, S. L. (2007). The volcanic–plutonic connection as a stage for understanding crustal magmatism. *Journal of Volcanology and Geothermal Research* **167**, 1–23.

Bachmann, O., Deering, C. D., Lipman, P. W. & Plummer, C. (2014). Building zoned ignimbrites by recycling silicic cumulates: insight from the 1,000 km³ Carpenter Ridge Tuff, CO. *Contributions to Mineralogy and Petrology* **167**, 1025.

Bacon, C. R. & Hirschmann, M. M. (1988). Mg/Mn partitioning as a test for equilibrium between coexisting Fe–Ti oxides. *American Mineralogist* **73**, 57–61.

Bacon, C. R., Dusel-Bacon, C., Aleinikoff, J. N. & Slack, J. F. (2014). The Late Cretaceous Middle Fork caldera, its resurgent intrusion, and enduring landscape stability in east–central Alaska. *Geosphere* **10**, 1432–1455.

Baker, B. H. & McBirney, A. R. (1985). Liquid fractionation. Part III: Geochemistry of zoned magmas and the compositional effects of liquid fractionation. *Journal of Volcanology and Geothermal Research* **24**, 55–81.

Barnes, C. G., Burton, B. R., Burling, T. C., Wright, J. E. & Karlsson, H. R. (2001). Petrology and geochemistry of the late Eocene Harrison Pass pluton, Ruby Mountains core complex, northeastern Nevada. *Journal of Petrology* **42**, 901–929.

Barth, A. P. & Wooden, J. L. (2010). Coupled elemental and isotopic analyses of polygenetic zircons from granitic rocks by ion microprobe, with implications for melt evolution and the sources of granitic magmas. *Chemical Geology* **277**, 149–159.

Bennett, V. C. & DePaolo, D. J. (1987). Proterozoic crustal history of the western United States as determined by neodymium isotopic mapping. *Geological Society of America Bulletin* **99**, 674–685.

Best, M. G., Christiansen, E. H., Deino, A. L., Gromme, C. S., McKee, E. H. & Noble, D. C. (1989). Eocene through Miocene volcanism in the Great Basin of the western United States. *New Mexico Bureau of Mines and Mineral Resources Memoir* **47**, 91–133.

Best, M. G., Barr, D. L., Christiansen, E. H., Gromme, C. S., Deino, A. L. & Tingey, D. G. (2009). The Great Basin altiplano during the middle Cenozoic ignimbrite flare up: Insights from volcanic rocks. *International Geology Review* **51**, 1–45.

Best, M. G., Christiansen, E. H., Deino, A. L., Gromme, S., Hart, G. L. & Tingey, D. G. (2013a). The 36–18 Ma Indian Peak–Caliente ignimbrite field and calderas, southeastern Great Basin, USA: Multicyclic super-eruptions. *Geosphere* **9**, 864–950.

Best, M. G., Christiansen, E. H. & Gromme, S. (2013b). Introduction: The 36–18 Ma southern Great Basin, USA, ignimbrite province and flareup: Swarms of subduction-related supervolcanoes. *Geosphere* **9**, 260–274.

Best, M. G., Gromme, C. S., Deino, A. L., Christiansen, E. H. & Tingey, D. G. (2013c). The 36–18 Ma Central Nevada ignimbrite field and calderas, Great Basin, USA: Multicyclic super-eruptions. *Geosphere* **9**, 1562–1636.

Bindeman, I. N. (2008). Oxygen isotopes in mantle and crustal magmas as revealed by single crystal analysis. In: Putirka, K. D. & Tepley, F. J. (eds) *Minerals, Inclusions and Volcanic Processes. Mineralogical Society of America and Geochemical Society, Reviews in Mineralogy and Geochemistry* **69**, 445–478.

Bindeman, I. N. & Valley, J. W. (2003). Rapid generation of both high-and low-δ^{18}O, large-volume silicic magmas at the Timber Mountain/Oasis Valley caldera complex, Nevada. *Geological Society of America Bulletin* **115**, 581–595.

Black, L. P., Kamo, S. L., Allen, C. M., Davis, D. W., Aleinikoff, J. N., Valley, J. W., Mundil, R., Campbell, I. H., Korsch, R. J., Williams, I. S. & Foudoulis, C. (2004). Improved $^{206}Pb/^{238}U$ microprobe geochronology by the monitoring of a trace-element-related matrix effect; SHRIMP, ID-TIMS, ELA-ICP-MS and oxygen isotope documentation for a series of zircon standards. *Chemical Geology* **205**, 115–140.

Boehnke, P., Watson, E. B., Trail, D., Harrison, T. M. & Schmitt, A. K. (2013). Zircon saturation rerevisited. *Chemical Geology* **351**, 324–334.

Bohrson, W. A. & Spera, F. J. (2007). Energy-constrained recharge, assimilation, and fractional crystallization (EC-RAxFC): A Visual Basic computer code for calculating trace

element and isotope variations of open-system magmatic systems. *Geochemistry, Geophysics, Geosystems* **8**, Q11003.

Brophy, J. G. (1991). Composition gaps, critical crystallinity, and fractional crystallization in orogenic (calc-alkaline) magmatic systems. *Contributions to Mineralogy and Petrology* **109**, 173–182.

Bryan, S. E., Peate, I. U., Peate, D. W., Self, S., Jerram, D. A., Mawby, M. R., Marsh, J. S. & Miller, J. A. (2010). The largest volcanic eruptions on Earth. *Earth-Science Reviews* **102**, 207–229.

Bucher, K. & Grapes, R. H. (2011). *Petrogenesis of Metamorphic Rocks*. 8th edn. Springer.

Buddington, A. F. (1959). Granite emplacement with special reference to North America. *Geological Society of America Bulletin* **70**, 671–748.

Burgisser, A. & Bergantz, G. W. (2011). A rapid mechanism to remobilize and homogenize highly crystalline magma bodies. *Nature* **471**, 212–215.

Caricchi, L., Annen, C., Blundy, J., Simpson, G. & Pinel, V. (2013). Frequency and magnitude of volcanic eruptions controlled by magma injection and buoyancy. *Nature Geoscience* **7**, 126–130.

Cassel, E. J., Breecker, D. O., Henry, C. D., Larson, T. E. & Stockli, D. F. (2014). Profile of a paleo-orogen: High topography across the present-day Basin and Range from 40–23 Ma. *Geology* **42**, 1007–1010.

Chamberlain, K. J., Morgan, D. J. & Wilson, C. J. N. (2014). Timescales of mixing and mobilization in the Bishop Tuff magma body: perspectives from diffusion chronometry. *Contributions to Mineralogy and Petrology* **168**, 1034.

Christiansen, E. H. & McCurry, M. (2008). Contrasting origins of Cenozoic silicic volcanic rocks from the western Cordillera of the United States. *Bulletin of Volcanology* **70**, 251–267.

Christiansen, E. H., Sheridan, M. F. & Burt, D. M. (1986). The geology and geochemistry of Cenozoic topaz rhyolites from the western United States. In: *Geological Society of America, Special Papers* **205**, 1–82.

Cole, J. S., Deering, C. D., Burt, R. M., Sewell, S., Shane, P. A. R. & Matthews, N. E. (2014). Okataina Volcanic Centre, Taupo Volcanic Zone, New Zealand: A review of volcanism and synchronous pluton development in an active, dominantly silicic caldera system. *Earth-Science Reviews* **128**, 1–17.

Coleman, D. S., Gray, W. & Glazner, A. F. (2004). Rethinking the emplacement and evolution of zoned plutons: geochronologic evidence for incremental assembly of the Tuolumne Intrusive Suite, California. *Geology* **32**, 433–436.

Colgan, J. P., John, D. A., Henry, C. D. & Fleck, R. J. (2008). Large-magnitude extension of the Eocene Caetano caldera, Shoshone and Toiyabe Ranges, Nevada. *Geosphere* **4**, 107–130.

Colgan, J. P., Howard, K. A., Fleck, R. J. & Wooden, J. L. (2010). Rapid middle Miocene extension and unroofing of the southern Ruby Mountains, Nevada. *Tectonics* **29**, TC6022.

Colgan, J. P., Henry, C. D. & John, D. A. (2011). Geologic map of the Caetano caldera, Lander and Eureka Counties, Nevada. Nevada Bureau of Mines and Geology Map 174.

Coney, P. J. (1978). Mesozoic–Cenozoic Cordilleran plate tectonics. In: Smith, R. B. & Eaton, G. P. (eds) *Cenozoic Tectonics and Regional Geophysics of the Western Cordillera. Geological Society of America, Memoirs* **152**, 33–50.

Coney, P. J. & Harms, T. A. (1984). Cordilleran metamorphic core complexes; Cenozoic extensional relics of Mesozoic compression. *Geology* **12**, 550–554.

Coney, P. J. & Reynolds, S. J. (1977). Cordilleran Benioff zones. *Nature* **270**, 403–406.

Cooper, G. F. & Wilson, C. J. N. (2014). Development, mobilisation and eruption of a large crystal-rich rhyolite: The Ongatiti ignimbrite, New Zealand. *Lithos* **198–199**, 38–57.

Cooper, K. M. & Kent, A. J. R. (2014). Rapid remobilization of magmatic crystals kept in cold storage. *Nature* **506**, 480–483.

Cousens, B., Henry, C. & Gupta, V. (2012). Distinct mantle sources for Pliocene Quaternary volcanism beneath the modern Sierra Nevada and adjacent Great Basin, northern California and western Nevada, USA. *Geosphere* **8**, 562–580.

DeCelles, P. G. & Coogan, J. C. (2006). Regional structure and kinematic history of the Sevier fold-and-thrust belt, central Utah. *Geological Society of America Bulletin* **118**, 841–864.

Deering, C. D. & Bachmann, O. (2010). Trace element indicators of crystal accumulation in silicic igneous rocks. *Earth and Planetary Science Letters* **297**, 324–331.

de Silva, S. L. (1989). Altiplano–Puna volcanic complex of the central Andes. *Geology* **17**, 1102–1106.

de Silva, S. L. (1991). Styles of zoning in the central Andean ignimbrites: Insights into magma chamber processes. In: Harmon, R. S. & Rapela, C. W. (eds) *Andean Magmatism and its Tectonic Setting. Geological Society of America, Special Papers* **265**, 233–243.

de Silva, S. L. & Gosnold, W. D. (2007). Episodic construction of batholiths: Insights from the spatiotemporal development of an ignimbrite flare-up. *Journal of Volcanology and Geothermal Research* **167**, 320–335.

de Silva, S. L., Zandt, G., Trumbull, R., Viramonte, J. G., Salas, G. & Jimenez, N. (2006). Large ignimbrite eruptions and volcano-tectonic depressions in the central Andes: a thermomechanical perspective. In: Troise, C., De Natale, G. & Kilburn, C. R. J. (eds) *Mechanisms of Activity and Unrest at Large Calderas. Geological Society, London, Special Publications* **269**, 47–63.

Dickinson, W. R. (2006). Geotectonic evolution of the Great Basin. *Geosphere* **2**, 353–368.

Drew, D. L., Bindeman, I. N., Watts, K. E., Schmitt, A. K., Fu, B. & McCurry, M. (2013). Crustal-scale recycling in caldera complexes and rift zones along the Yellowstone hotspot track: O and Hf isotopic evidence in diverse zircons from voluminous rhyolites of the Picabo volcanic field, Idaho. *Earth and Planetary Science Letters* **381**, 63–77.

Druitt, T. H., Costa, F., Deloule, E., Dungan, M. & Scaillet, B. (2012). Decadal to monthly timescales of magma transfer and reservoir growth at a caldera volcano. *Nature* **482**, 77–80.

Dufek, J. & Bachmann, O. (2010). Quantum magmatism: magmatic compositional gaps generated by crystal–melt dynamics. *Geology* **38**, 687–690.

Ellis, B. S., Bachmann, O. & Wolff, J. A. (2014). Cumulate fragments in silicic ignimbrites: The case of the Snake River Plain. *Geology* **42**, 431–434.

Farmer, G. L. & DePaolo, D. J. (1983). Origin of Mesozoic and Tertiary granite in the western United States and implications for pre-Mesozoic crustal structure: 1. Nd and Sr isotopic studies in the geocline of the northern Great Basin. *Journal of Geophysical Research* **88**, 3379–3401.

Farrell, J., Smith, R. B., Husen, S. & Diehl, T. (2014). Tomography from twenty-six years of seismicity reveals the spatial extent of the Yellowstone crustal magma reservoir extends well beyond the Yellowstone caldera. *Geophysical Research Letters* **41**, 3068–3073.

Ferry, J. M. & Watson, E. B. (2007). New thermodynamic models and revised calibrations for the Ti-in-zircon and Zr-in-rutile thermometers. *Contributions to Mineralogy and Petrology* **154**, 429–437.

Folkes, C. B., Wright, H. M., Cas, R. A. F., de Silva, S. L., Lesti, C. & Viramonte, J. G. (2011). A re-appraisal of the stratigraphy and volcanology of the Cerro Galan volcanic system, NW Argentina. *Bulletin of Volcanology* **73**, 1427–1454.

Folkes, C. B., de Silva, S. L., Bindeman, I. N. & Cas, R. A. F. (2013). Tectonic and climate history influence the geochemistry of large-volume silicic magmas: New $\delta^{18}O$ data from the Central Andes with comparison to N. America and Kamchatka. *Journal of Volcanology and Geothermal Research* **262**, 90–103.

Frazer, R. E., Coleman, D. S. & Mills, R. D. (2014). Zircon U–Pb geochronology of the Mount Givens Granodiorite: implications for the genesis of large volumes of eruptible magma. *Journal of Geophysical Research* **119**, 2907–2924.

Fridrich, C. J. Smith, R. P., DeWitt, E. & McKee, E. H. (1991). Structural, eruptive, and intrusive evolution of the Grizzly Peak caldera, Sawatch Range, Colorado. *Geological of Society America Bulletin* **103**, 1160–1177.

Gans, P. B., Mahood, G. A. & Schermer, E. (1989). Synextensional magmatism in the Basin and Range Province; A case study from the eastern Great Basin. In: *Geological Society of America, Special Papers* **233**, 1–53.

Ghiorso, M. S. & Evans, B. W. (2008). Thermodynamics of rhombohedral oxide solid solutions and a revision of the Fe–Ti two-oxide geothermometer and oxygen-barometer. *American Journal of Science* **308**, 957–1039.

Gilluly, J. & Masursky, H. (1965). *Geology of the Cortez Quadrangle, Nevada. US Geological Survey Bulletin* **1175**, 117 pp.

Glazner, A. F., Bartley, J. M., Coleman, D. S., Gray, W. & Taylor, R. Z. (2004). Are plutons assembled over millions of years by amalgamation from small magma chambers?. *Geological Society of America Today* **14**, 4–11.

Glazner, A. F., Coleman, D. S. & Bartley, J. M. (2008). The tenuous connection between high-silica rhyolites and granodiorite plutons. *Geology* **36**, 183–186.

Gregg, P. M., de Silva, S. L., Grosfils, E. B. & Parmigiani, J. P. (2012). Catastrophic caldera-forming eruptions: Thermomechanics and implications for eruption triggering and maximum caldera dimensions on Earth. *Journal of Volcanology and Geothermal Research* **241–242**, 1–12.

Gregg, P. M., Grosfils, E. B. & de Silva, S. L. (2015). Catastrophic caldera-forming eruptions II: the subordinate role of magma buoyancy as an eruption trigger. *Journal of Volcanology and Geothermal Research* **305**, 100–113.

Grunder, A. L. (1995). Material and thermal roles of basalt in crustal magmatism: case study from eastern Nevada. *Geology* **23**, 952–956.

Grunder, A. L., Klemetti, E. K., McKee, C. M. & Feeley, T. C. (2008). Eleven million years of arc volcanism at the Aucanquilcha Volcanic Cluster, Northern Chilean Andes: Implications for the lifespan and emplacement of batholiths. *Transactions of the Royal Society of Edinburgh: Earth Sciences* **97**, 415–436.

Gualda, G. A., Ghiorso, M. S., Lemons, R. V. & Carley, T. L. (2012). Rhyolite-MELTS: A modified calibration of MELTS optimized for silica-rich, fluid-bearing magmatic systems. *Journal of Petrology* **53**, 875–890.

Hart, G. L. (1997). An oxygen isotope investigation of the Indian Peak Volcanic Field, southern Utah–Nevada: Magma source constraints on a late Oligocene caldera system. MS thesis, Brigham Young University, Provo, UT, 57 pp.

Henry, C. D. & John, D. A. (2013). Magmatism, ash-flow tuffs, and calderas of the ignimbrite flareup in the western Nevada volcanic Field, Great Basin, USA. *Geosphere* **9**, 951–1008.

Henry, C. D., Hinz, N. H., Faulds, J. E., Colgan, J. P., John, D. A., Brooks, E. R., Cassel, E. J., Garside, L. J., Davis, D. A. & Castor, S. B. (2012). Eocene–Early Miocene paleotopography of the Sierra Nevada–Great Basin–Nevadaplano based

on widespread ash-flow tuffs and paleovalleys. *Geosphere* **8**, 1–27.

Hildreth, W. (1979). The Bishop Tuff: evidence for the origin of the compositional zonation in silicic magma chambers. In: *Geological Society of America, Special Papers* **180**, 43–76.

Hildreth, W. (1981). Gradients in silicic magma chambers: Implications for lithospheric magmatism. *Journal of Geophysical Research* **86**, 10153–10192.

Hildreth, W. (2004). Volcanological perspectives on Long Valley, Mammoth Mountain, and Mono Craters: Several contiguous but discrete systems. *Journal of Volcanology and Geothermal Research* **136**, 169–198.

Hildreth, W. S. & Wilson, C. J. N. (2007). Compositional zoning in the Bishop Tuff. *Journal of Petrology* **48**, 951–999.

Howard, K. A. (2003). Crustal structure in the Elko–Carlin Region, Nevada, during Eocene gold mineralization: Ruby–East Humboldt metamorphic core complex as a guide to the deep crust. *Economic Geology* **98**, 249–268.

Huber, C., Bachmann, O. & Dufek, J. (2012). Crystal-poor versus crystal-rich ignimbrites: A competition between stirring and reactivation. *Geology* **40**, 115–118.

Hudec, M. R. (1992). Mesozoic structural and metamorphic history of the central Ruby Mountains metamorphic core complex, Nevada. *Geological Society of America Bulletin* **104**, 1086–1100.

Humphreys, E. D. (1995). Post-Laramide removal of the Farallon slab, western United States. *Geology* **23**, 987–990.

Humphreys, E. D., Hessler, E., Dueker, K., Farmer, G. L., Erslev, E. & Atwater, T. (2003). How Laramide-age hydration of North American lithosphere by the Farallon slab controlled subsequent activity in the western United States. *International Geology Review* **45**, 575–595.

Ireland, T. R. & Williams, I. S. (2003). Considerations in zircon geochronology by SIMS. In: Hanchar, J. M. & Hoskin, P. W. O. (eds) *Zircon. Mineralogical Society of America and Geochemical Society, Reviews in Mineralogy and Geochemistry* **53**, 215–241.

Jellinek, A. & DePaolo, D. J. (2003). A model for the origin of large silicic magma chambers; precursors of caldera-forming eruptions. *Bulletin of Volcanology* **65**, 363–381.

John, D. A., Henry, C. D. & Colgan, J. P. (2008). Magmatic and tectonic evolution of the Caetano caldera, north–central Nevada: A tilted, mid-Tertiary eruptive center and source of the Caetano Tuff. *Geosphere* **4**, 75–106.

John, D. A., Colgan, J. P., Henry, C. D. & Wooden, J. L. (2009). Prolonged Eocene magmatism culminating with the Caetano caldera, Cortez area, Nevada: Inferences from SHRIMP U–Pb zircon dating. American Geophysical Union, Fall Meeting 2009, abstract V41B-2187.

John, D. A., Rockwell, B. W., Henry, C. D. & Colgan, J. P. (2011). Hydrothermal alteration of the late Eocene Caetano ash-flow caldera, north–central Nevada: A field and ASTER remote sensing study. In: Steininger, R. & Pennell, B. (eds) *Great Basin Evolution and Metallogeny Proceedings. Geological Society of Nevada 2010 Symposium.* Reno, NV, pp. 1055–1083.

King, E. M., Valley, J. W., Stockli, D. F. & Wright J. E.. (2004). Oxygen isotopic trends of granitic magmatism in the Great Basin: Location of the Precambrian craton boundary as reflected in zircons. *Geological Society of America Bulletin* **116**, 451–462.

Kistler, R. W. (1990). Two different lithosphere types in the Sierra Nevada, California. In: Anderson, J. L. (ed.) *The Nature and Origin of Cordilleran Magmatism. Geological Society of America, Memoirs* **174**, 271–281.

Kucks, R. P., Hill, P. L. & Ponce, D. A. (2006). Nevada magnetic and gravity maps and data: A website for the distribution of data. *US Geological Survey Data Series* **234**, http://pubs.usgs.gov/ds/2006/234.

Kuiper, K. F., Deino, A., Hilgen, F. J., Krijgsman, W., Renne, P. R. & Wijbrans, J. R. (2008). Synchronizing rock clocks of Earth history. *Science* **320**, 500–504.

Larson, P. B. & Taylor, H. P. (1986). $^{18}O/^{16}O$ ratios in ash-flow tuffs and lavas erupted from the central Nevada caldera complex and the central San Juan caldera complex, Colorado. *Contributions to Mineralogy and Petrology* **92**, 146–156.

Lee, S., Barnes, C. G., Snoke, A. W., Howard, K. A. & Frost, C. D. (2003). Petrogenesis of Mesozoic, peraluminous granites in the Lamoille Canyon area, Ruby Mountains, Nevada, USA. *Journal of Petrology* **44**, 713–732.

Leonardson, R. L. (2010). Barrick Cortez Gold Acres structure. In: Steininger, R. & Pennell, W. (eds) *Great Basin Evolution and Metallogeny: Geological Society of Nevada Symposium Proceedings*, pp. 17–29.

Lipman, P. W. (1984). The roots of ash-flow calderas in western North America: windows into the tops of granitic batholiths. *Journal of Geophysical Research* **89**, 8801**–**8841.

Lipman, P. W. (2007). Incremental assembly and prolonged consolidation of Cordilleran magma chambers: Evidence from the Southern Rocky Mountain volcanic field. *Geosphere* **3**, 42–70.

Lipman, P. W. & Bachmann, O. (2015). Ignimbrites to batholiths: Integrating perspectives from geological, geophysical, and geochronological data. *Geosphere* **11**, 705–743.

Lipman, P. W., Christiansen, R. L. & O'Connor, J. T. (1966). *A compositionally zoned ash-flow sheet in southern Nevada. US Geological Survey, Professional Papers* **524-F**, 47 pp.

Lipman, P. W., Prostka, H. J. & Christiansen, R. L. (1972). Cenozoic volcanism and plate tectonic evolution of western United States, Part 1: Early and middle Cenozoic. *Philosophical Transactions of the Royal Society of London, Series A* **271**, 217–248.

Lipman, P. W., Zimmerer, M. J. & McIntosh, W. C. (2015). An ignimbrite caldera from the bottom up: exhumed floor and fill of the resurgent Bonanza caldera, Southern Rocky Mountain volcanic field, Colorado. *Geosphere* **11**, 1902–1947.

Long, S. P., Henry, C. D., Muntean, J. L., Edmondo, G. P. & Cassel, E. J. (2014). Early Cretaceous construction of a structural culmination, Eureka, Nevada, U.S.A.: implications for out-of-sequence deformation in the Sevier hinterland. *Geosphere* **3**, 564–584.

Ludwig, K. R. (2009). *SQUID 2: A User's Manual, rev. 12 Apr, 2009. Berkeley Geochronology Center Special Publication* **5**.

Ludwig, K. R. (2012). *Isoplot 3.75, a geochronological toolkit for Excel. Berkeley Geochronology Center Special Publication* **5**.

MacDonald, W. D., Palmer, H. C., Deino, A. L. & Shen, P. Y. (2012). Insights into deposition and deformation of intra-caldera ignimbrites, central Nevada. *Journal of Volcanology and Geothermal Research* **245–246**, 40–54.

Mahood, G. A. (1990). Second reply to comment of R. S. J. Sparks, H. E. Huppert and C. J. N. Wilson on 'Evidence for long residence times of rhyolitic magma in the Long Valley magmatic system: the isotopic record in the precaldera lavas of Glass Mountain'. *Earth and Planetary Science Letters* **99**, 395–399.

Malfait, W. J., Siefert, R., Petitgirard, S., Perrillat, J. P., Mezouar, M., Ota, T., Nakamura, E., Lerch, P. & Sanchez-Valle, C. (2014). Supervolcano eruptions driven by melt buoyancy in large silicic magma chambers. *Nature Geoscience* **7**, 122–125.

Mastin, L. G., Van Eaton, A. R. & Lowenstern, J. B. (2014). Modeling ash fall distribution from a Yellowstone

supereruption. *Geochemistry, Geophysics, Geosystems* **15**, 3459–3475.

Matthews, N. E., Pyle, D. M., Smith, V. C., Wilson, C. J. N., Huber, C. & van Hinsberg, V. (2012). Quartz zoning and the pre-eruptive evolution of the ~340-ka Whakamaru magma systems, New Zealand. *Contributions to Mineralogy and Petrology* **163**, 87–107.

Maughan, L. L., Christiansen, E. H., Best, M. G., Gromme, C. S., Deino, A. L. & Tingey, D. G. (2002). The Oligocene Lund Tuff, Great Basin, USA: a very large volume monotonous intermediate. *Journal of Volcanology and Geothermal Research* **113**, 129–157.

McDonough, W. F. & Sun, S. (1995). The composition of the Earth. *Chemical Geology* **120**, 223–253.

McKee, E. H. (1971). Tertiary igneous chronology of the Great Basin of the western United States—Implications for tectonic models. *Geological Society of America Bulletin* **82**, 3497–3502.

Miller, C. F. & Mittlefehldt, D. W. (1982). Depletion of light rare-earth elements in felsic magmas. *Geology* **10**, 129–133.

Miller, J., Matzel, J. E., Miller, C. F., Burgess, S. D. & Miller, R. B. (2007). Zircon growth and recycling during the assembly of large, composite arc plutons. *Journal of Volcanology and Geothermal Research* **167**, 282–299.

Mills, R. D. & Coleman, D. S. (2013). Temporal and chemical connections between plutons and ignimbrites from the Mount Princeton magmatic center. *Contributions to Mineralogy and Petrology* **165**, 961–980.

Misch, P. & Hazzard, J. C. (1962). Stratigraphy and metamorphism of late Precambrian rocks in central northeastern Nevada and adjacent Utah. *AAPG Bulletin* **46**, 289–343.

Morgan, D. J., Blake, S., Rogers, N. W., De Vivo, B., Roland, G. & Davidson, J. P. (2006). Magma chamber recharge at Vesuvius in the century prior to the eruption of A.D. 79. *Geology* **34**, 845–848.

Muntean, J. L., Cline, J. S., Simon, A. C. & Longo, A. A. (2011). Magmatic–hydrothermal origin of Nevada's Carlin-type gold deposits. *Nature Geoscience* **4**, 122–127.

Nash, W. P. & Crecraft, H. R. (1985). Partition coefficients for trace elements in silicic magmas. *Geochimica et Cosmochimica Acta* **49**, 2309–2322.

Nash, B. P., Perkins, M. E., Christensen, J. N., Lee, D. C. & Halliday, A. N. (2006). The Yellowstone hotspot in space and time: Nd and Hf isotopes in silicic magmas. *Earth and Planetary Science Letters* **247**, 143–156.

Patiño Douce, A. E. (1999). What do experiments tell us about the relative contribution of crust and mantle in the origin of granitic magmas?. In: Castro, A., Fernandez, C. & Vigneresse, J. (eds) *Understanding Granites: Intergrating New and Classic Techniques. Geological Society, London, Special Publications* **168**, 55–75.

Patiño Douce, A. E. & Johnston, A. D. (1991). Phase equilibria and melt productivity in the pelitic system: implications for the origin of peraluminous granitoids and aluminous granulites. *Contributions to Mineralogy and Petrology* **107**, 202–218.

Petford, N., Cruden, A. R., McCaffrey, K. J. W. & Vigneresse, J.-L. (2000). Granite magma formation, transport and emplacement in the Earth's crust. *Nature* **408**, 669–673.

Ridolfi, F., Renzulli, A. & Puerini, M. (2010). Stability and chemical equilibrium of amphibole in calc-alkaline magmas: an overview, new thermobarometric formulations and application to subduction-related volcanoes. *Contributions to Mineralogy and Petrology* **160**, 45–66.

Rodgers, D. W. (1984). Stratigraphy, correlation, and depositional environments of upper Proterozoic and lower Cambrian rocks of the southern Deep Creek Range, Utah. *Utah Geological Association Publication* **13**, 79–92.

Smith, R. L. (1979). Ash-flow magmatism. In: *Geological Society of America, Special Papers* **180**, 5–25.

Spera, F. J., Yuen, D. A., Greer, J. C. & Sewell, G. (1986). Dynamics of magma withdrawal from stratified magma chambers. *Geology* **14**, 723–726.

Stankiewicz, J., Ryberg, T., Haberland, C., Fauzi & Natawidjaja, D. (2010). Lake Toba volcano magma chamber imaged by ambient seismic noise tomography. *Geophysical Research Letters* **37**, L17306.

Stelten, M. E., Cooper, K. M., Vazquez, J. A., Calvert, A. T. & Glessner, J. J. G. (2015). Mechanisms and timescales of generating eruptible rhyolitic magmas at Yellowstone caldera from zircon and sanidine geochronology and geochemistry. *Journal of Petrology* **56**, 1607–1642.

Streck, M. J. & Grunder, A. L. (2007). Phenocryst-poor rhyolites of bimodal, tholeiitic provinces: the Rattlesnake Tuff and implications for mush extraction models. *Bulletin of Volcanology* **70**, 385–401.

Tappa, M. J., Coleman, D. S., Mills, R. D. & Samperton, K. M. (2011). The plutonic record of a silicic ignimbrite from the Latir volcanic field, New Mexico. *Geochemistry, Geophysics, Geosystems* **12**, Q10011.

Till, C. B., Vazquez, J. A. & Boyce, J. W. (2015). Months between rejuvenation and volcanic eruption at Yellowstone caldera, Wyoming. *Geology* **43**, 695–698.

Trail, D., Bindeman, I. N., Watson, E. B. & Schmitt, A. K. (2009). Experimental calibration of oxygen isotope fractionation between quartz and zircon. *Geochimica et Cosmochimica Acta* **73**, 7110–7126.

Ward, K. M., Zandt, G., Beck, S. L., Christiansen, D. H. & McFarlin, H. L. (2014). Seismic imaging of the magmatic underpinnings beneath the Altiplano–Puna volcanic complex from the joint inversion of surface wave dispersion and receiver functions. *Earth and Planetary Science Letters* **40**, 43–53.

Wark, D. A., Hildreth, W., Spear, F. S., Cherniak, D. J. & Watson, E. B. (2007). Pre-eruption recharge of the Bishop magma system. *Geology* **35**, 235–238.

Watts, K. E., Bindeman, I. N. & Schmitt, A. K. (2011). Large-volume rhyolite genesis in caldera complexes of the Snake River Plain: Insights from the Kilgore Tuff of the Heise volcanic field, Idaho, with comparison to Yellowstone and Bruneau Jarbidge rhyolites. *Journal of Petrology* **52**, 857–890.

Watts, K. E., Coble, M. A., Vazquez, J. A., Henry, C. D., Colgan, J. P. & John, D. A. (2016). Chemical abrasion-SIMS (CA-SIMS) U–Pb dating of zircon from the late Eocene Caetano caldera, Nevada. *Chemical Geology* **439**, 139–151.

White, R. W., Powell, R. & Clarke, G. L. (2003). Prograde metamorphic assemblage evolution during partial melting of metasedimentary rocks at low pressures: migmatites from Mt. Stafford, central Australia. *Journal of Petrology* **44**, 1937–1960.

White, S. M., Crips, J. A. & Spera, F. J. (2006). Long-term volumetric eruption rates and magma budgets. *Geochemistry, Geophysics, Geosystems* **7**, Q03010.

Williams, I. S. (1997). U–Th–Pb geochronology by ion microprobe: not just ages but histories. *Society of Economic Geologists, Reviews in Economic Geology* **7**, 1–35.

Wilson, C. J. N. & Hildreth, W. (1997). The Bishop Tuff: New insights from eruptive stratigraphy. *Journal of Geology* **105**, 407–440.

Wolff, J. A., Ellis, B. S., Ramos, F. C., Starkel, W. A., Boroughs, S., Olin, P. H. & Bachmann, O. (2015). Remelting of cumulates as a process for producing chemical zoning in silicic tuffs: A comparison of cool, wet and hot, dry rhyolitic magma systems. *Lithos* **236–237**, 275–286.

Wooden, J. L., Kistler, R. W. & Tosdal, R. M. (1999). *Strontium, lead, and oxygen isotopic data for granitoid and volcanic rocks from the northern Great Basin and Sierra Nevada, California, Nevada and Utah. US Geological Survey, Open-File Report* **99–569**, 20 pp.

Wotzlaw, J. F., Schaltegger, U., Frick, D. A., Dungan, M. A., Gerdes, A. & Guünther, D. (2013). Tracking the evolution of large-volume silicic magma reservoirs from assembly to supereruption. *Geology* **41**, 867–870.

Wright, J. E. & Wooden, J. L. (1991). New Sr, Nd, and Pb isotopic data from plutons in the northern Great Basin: implications for crustal structure and granite petrogenesis in the hinterland of the Sevier thrust belt. *Geology* **19**, 457–460.

Yonkee, W. A., Dehler, C. D., Link, P. K., Balgord, E. A., Keeley, J. A., Hayes, D. S., Wells, M. L., Fanning, C. M. & Johnston, S. M. (2014). Tectono-stratigraphic framework of Neoproterozoic to Cambrian strata, west–central U.S.: Protracted rifting, glaciation, and evolution of the North American Cordilleran margin. *Earth-Science Reviews* **136**, 59–95.

Zimmerer, M. J. & McIntosh, W. C. (2012). An investigation of caldera-forming magma chambers using the timing of ignimbrite eruptions and pluton emplacement at the Mt. Aetana caldera complex. *Journal of Volcanology and Geothermal Research* **245–246**, 128–148.

Zimmerer, M. J. & McIntosh, W. C. (2013). Geochronologic evidence of upper-crustal *in situ* differentiation: Silicic magmatism at the Organ caldera complex, New Mexico. *Geosphere* **9**, 155–169.